DESIGN AND ANALYSIS OF INTELLIGENT SYSTEM FOR CLASSIFICATION OF COVID AND NON-COVID PATIENTS

Thesis Submitted for the Award of the Degree of

DOCTOR OF PHILOSOPHY

Electronics and Communication Engineering

By

Patibandla Anitha

Registration Number: 42100225

Supervised By

Dr Manu Prakram(14704)

Assistant Professor

School of Electronics and Electrical Engineering

Lovely Professional University

LOVELY PROFESSIONAL UNIVERSITY, PUNJAB

2026

DECLARATION

I, **Patibandla Anitha** bearing Registration No.**42100225**, hereby declare that the research work embodied in the Ph.D. thesis titled **"DESIGN AND ANALYSIS OF INTELLIGENT SYSTEM FOR CLASSIFICATION OF COVID AND NON-COVID PATIENTS"** submitted to **Lovely Professional University, Punjab** is the original and bonafide work carried out by me under the supervision of Dr.Manu Prakram, Assistant Professor, **School of Electronics and Electrical Engineering, Lovely Professional University, Punjab.**

I further declare that:

a) The work presented in this thesis is a genuine contribution to the field of research and is a result of investigations carried out by me during the period of my doctoral study.

b) The research work has been conducted in accordance with the academic and ethical standards prescribed by the university.

c) Due acknowledgements and references have been duly given wherever the work of others has been cited or used.

d) The thesis has not been submitted either partly or fully to any other university or institution for the award of any degree or diploma.

I understand that any violation of the above declarations may lead to the cancellation of my degree by the university at any stage.

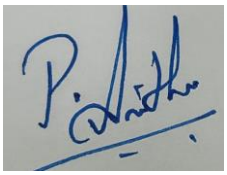

Signature of Scholar

Name: Patibandla Anitha

Registration Number: 42100225

Date: 19-02-2026

CERTIFICATE

This is to certify that the work reported in the Ph. D. thesis entitled **"DESIGN AND ANALYSIS OF INTELLIGENT SYSTEM FOR CLASSIFICATION OF COVID AND NON-COVID PATIENTS"** submitted in fulfillment of the requirement for the award of degree of **Doctor of Philosophy (Ph.D.)** in the **School of Electronics and Electrical Engineering** is a research work carried out by **Patibandla Anitha,42100225**, is bonafide record of her original work carried out under my supervision and that no part of thesis has been submitted for any other degree, diploma or equivalent course.

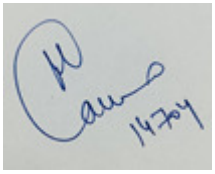

Signature of Supervisor

Name: Dr Manu Prakram

UID: 14704

Date: 19-02-2026

ACKNOWLEDGEMENTS

First and foremost, I would like to thank God Almighty for giving me the wisdom, strength, knowledge, ability, and opportunity to undertake this project. It gives me a great delight to express my gratitude to many people, without their support and inspiration; this thesis work would not have been possible.

I would like to express my sincere gratitude to HoS Dr. Gaurav Sethi, Professor, SEEE, Lovely Professional University for the continuous support of my Ph.D work his motivation, and his immense knowledge. I sincerely thank my supervisor, Dr.Manu Prakram, Assistant Professor, SEEE for his exceptional guidance, valuable advice, and constant support throughout this project. His guidance helped me in all the time of research and writing of this thesis. I would like to express my sincere gratitude to Dr.Kirti Rawal for her constant support and motivation throughout the duration of my work. Her guidance at all stages of my work has been instrumental in my work progress. She has been patient in answering my queries and motivated me at times of uncertainty for progressing forward. It was a great pleasure for me to have a chance to work with both of them. I have really learned the basics of research from both of them. I would like to thank all the faculty and staff members of the School of Electronics and Electrical Engineering, Lovely Professional University, Punjab, India,for their help and support. I am deeply thankful to Chancellor, Vice Chancellor Lovely Professional University, Registrar, Dean (Academic), Dean (School of Engineering & Electrical Engineering), DRP and RDC members for their moral support, for providing the necessary suggestions and for providing me with all the necessary facilities during my candidature.

I also express my deep sense of gratitude to Dr.K.L.Mallikarjun, HoD, ECE Malla Reddy College of Engineering and Technology for his endless support and inspiration throughout the duration of my work. I thank the faculty and staff members of Electronics and Communication Engineering Department of Malla Reddy College of Engineering and Technology for their constant moral support and inspiration.

I owe to my family members for all types of support. Without their affection, there would have been nothing to write an acknowledgement. In particular, I thank my parents, Mr P.Nageswara Rao and Mrs, P.V.Ratna Kumari ,my sister Mrs.P.Padmaja, my ever supporting beautiful daughters Neelotpala and Nidhi for their wishes, affection, love, inspiration, and never-ending support that helped me in the difficult stages of my work.

Last but not least, I express my gratitude to those who helped me directly and indirectly for the successful completion of the research work. Thank you all for encouraging me and inspiring me to achieve my dreams.

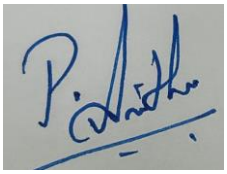

PATIBANDLA ANITHA

Registration number: 42100225

School of Electronics and Electrical engineering

Lovely Professional University, Punjab

Abstract

The COVID-19 pandemic has emerged as one of the most devastating global health crises of the 21st century, severely impacting medical, social, and economic systems worldwide. As of 2025, more than 770 million confirmed cases and approximately 6.9 million deaths have been reported globally, underscoring the urgent need for efficient diagnostic, preventive, and therapeutic strategies. The rapid transmission rate of severe acute respiratory syndrome (SARS)-CoV-2, coupled with the emergence of new viral variants, has further complicated containment efforts, making early and accurate diagnosis a cornerstone in managing disease spread and optimizing patient outcomes. Timely identification of infection not only facilitates prompt clinical intervention but also helps in contact tracing, quarantine enforcement, and epidemiological modelling essential for public health decision-making.

Traditional molecular diagnostic approaches such as Reverse Transcription Polymerase Chain Reaction (RT-PCR) are widely regarded as the gold standard for COVID-19 detection. However, their sensitivity is highly dependent on viral load, sample collection quality, and testing conditions. False negatives, logistical delays, and limited testing capacity especially in resource-constrained settings—have hindered their effectiveness in large-scale screening. Consequently, imaging modalities such as Computed Tomography (CT) and Chest X-Ray (CXR) have emerged as indispensable adjunct diagnostic tools. These imaging techniques provide non-invasive, rapid visualization of lung abnormalities, enabling detection of typical manifestations such as ground-glass opacities, bilateral patchy shadows, and interstitial lesions associated with COVID-19 infection. Particularly in cases where RT-PCR results are inconclusive or delayed, radiological imaging has proven invaluable for clinical decision support.

However, manual interpretation of CT and CXR images poses significant challenges to both patients and clinicians. The exponential increase in caseload during the pandemic has overwhelmed healthcare systems globally, leading to delayed diagnoses and compromised care. Radiologists are often required to analyze hundreds of images daily under high-pressure conditions, increasing the risk of fatigue-induced diagnostic errors. Furthermore, the subtle and heterogeneous visual characteristics of COVID-19 lesions—especially in early or asymptomatic stages—complicate accurate manual differentiation from other viral pneumonias or respiratory disorders. Variations in imaging quality, scanner settings, and patient posture further introduce inconsistencies in visual assessments. These factors

collectively contribute to variability in diagnosis, subjectivity in interpretation, and delayed clinical response, emphasizing the urgent need for intelligent, automated systems that can assist radiologists in fast and reliable COVID-19 detection.

To address these challenges, the present study proposes an integrated and optimized Deep Learning (DL) based diagnostic framework that leverages both CT and CXR imaging data for automated COVID-19 detection. The methodology comprises three principal stages: advanced preprocessing, optimized segmentation, and efficient classification. Each stage is meticulously designed to ensure high diagnostic accuracy, robustness to heterogeneous imaging conditions, and computational efficiency suitable for real-time implementation in clinical environments.

In the first stage, preprocessing is performed using the Block-Matching and 3D Filtering (BM3D) technique, a state-of-the-art denoising algorithm known for its exceptional ability to preserve fine image structures while effectively suppressing noise. The BM3D algorithm operates by grouping similar 2D image blocks into 3D arrays and performing collaborative filtering in the transform domain. This approach significantly enhances signal-to-noise ratio (SNR) without blurring essential anatomical and pathological details. When applied to CT and CXR datasets, BM3D improves the visual clarity of lung regions and pathological features such as opacities and consolidations. The resulting high-fidelity images provide a strong foundation for subsequent segmentation and feature extraction stages, mitigating the adverse effects of noise, motion artifacts, and intensity inhomogeneity that are prevalent in medical imaging datasets.

Following denoising, the study focuses on precise lung and lesion segmentation, a critical step that delineates infected areas and isolates relevant regions for analysis. To achieve this, an Optimal U-Net (OU-Net) architecture is employed, an advanced variant of the traditional U-Net model specifically tailored for medical image segmentation. OU-Net incorporates adaptive encoder-decoder pathways, multi-scale feature fusion, and enhanced skip connections that facilitate more accurate boundary preservation and context aggregation. This architectural refinement ensures that the model captures both global contextual information and local spatial details, essential for identifying subtle COVID-19 lesions. The performance of OU-Net is further enhanced through the Modified Grey Wolf Optimization (MGWO) algorithm, which optimizes the network's hyperparameters, including learning rate, filter sizes, and weight coefficients. MGWO, inspired by the social hierarchy and hunting strategy of grey wolves, introduces adaptive control parameters that improve convergence speed,

avoid premature stagnation, and enhance segmentation accuracy across diverse imaging modalities. As a result, the OU-Net with MGWO optimization demonstrates superior delineation of infected lung regions, outperforming conventional U-Net and other segmentation frameworks in terms of Dice coefficient, Intersection over Union (IoU) (IoU), and boundary precision metrics.

The third stage of the proposed methodology involves the classification of COVID-19 and normal cases using a hybrid DL and feature optimization pipeline termed CT-CXR-COVID-19 Classification Network (CT-CXR-Net). After BM3D preprocessing and OU-Net-based segmentation, deep features are extracted using the ResNet50 architecture, a robust Convolutional Neural Network (CNN) known for its residual learning mechanism that alleviates vanishing gradient problems. ResNet50 effectively captures complex hierarchical representations of visual patterns from both CT and CXR images, enabling the model to discern between subtle textural differences indicative of infection and healthy lung tissue. These deep features, however, are typically high-dimensional and contain redundant or irrelevant information, which can degrade classifier performance and increase computational overhead.

To overcome this limitation, the Improved Brown Bear Optimization (IBBO) algorithm is utilized for feature selection. IBBO, inspired by the foraging and migration behaviour of brown bears, is enhanced with adaptive exploration and exploitation strategies to balance global and local search capabilities. The algorithm selects the most informative and discriminative feature subsets that contribute maximally to classification accuracy while minimizing redundancy. This intelligent feature selection reduces data dimensionality, enhances model generalization, and accelerates the classification process.

The final classification is performed using a Ridge Classifier, chosen for its balance between bias and variance, and its robustness against multicollinearity among selected features. By applying L2 regularization, the Ridge Classifier minimizes overfitting while maintaining high generalization performance across varying datasets. This combination of deep feature extraction, nature-inspired optimization, and robust classification ensures reliable COVID-19 detection with superior performance compared to conventional CNN-based or Machine Learning (ML)-based approaches.

Experimental validation of the proposed framework is conducted on publicly available CT and CXR datasets containing both COVID-19 positive and normal cases. Extensive performance comparisons with state-of-the-art methods including VGG19, DenseNet121,

InceptionV3, and standard U-Net variants demonstrate that the proposed BM3D–OU-Net–MGWO–ResNet50–IBBO–Ridge pipeline achieves substantial improvements in diagnostic accuracy and segmentation fidelity. The integration of multi-stage optimization (MGWO and IBBO) ensures the model's adaptability across different imaging resolutions making it suitable for clinical deployment.

Beyond performance metrics, the proposed methodology offers several practical advantages. First, it significantly reduces the dependency on manual interpretation, alleviating radiologist workload during high patient inflow conditions. Second, the preprocessing and segmentation pipeline ensures interpretability by producing clear visual delineations of infected regions, thereby providing clinicians with transparent diagnostic insights. Third, the modular structure of the framework allows easy integration into existing hospital information systems, facilitating seamless clinical adoption. Furthermore, the combination of CT and CXR data enhances the robustness of diagnosis by enabling cross-validation between imaging modalities, reducing the risk of false negatives and improving reliability.

Finally, this study presents a comprehensive and optimized framework for automated COVID-19 detection using multimodal imaging data. The novelty lies in the synergistic integration of BM3D-based preprocessing, MGWO-optimized OU-Net segmentation, ResNet50 deep feature extraction, IBBO-driven feature optimization, and Ridge classification, forming a unified and interpretable diagnostic pipeline. By addressing the limitations of manual analysis and conventional DL models, the proposed CT-CXR-Net framework demonstrates exceptional potential for real-world clinical application. It not only enhances diagnostic accuracy and speed but also contributes to building scalable, data-driven healthcare systems capable of responding effectively to current and future pandemics. Ultimately, this research bridges the gap between medical imaging, Artificial Intelligence (AI), and optimization-driven learning, advancing the frontier of automated disease diagnosis and supporting global efforts in pandemic preparedness and management.

Contents

List of Tables

List of Figures

List of Abbreviations

AI	Artificial Intelligence
ARDS	Acute Respiratory Distress Syndrome
BM3D	Block-Matching and 3D Filtering
CAM	Class Activation Mapping
CLAHE	Contrast Limited Adaptive Histogram Equalization
CNN	Convolutional Neural Network
COVID-19	Coronavirus Disease 2019
CT	Computed Tomography
CT-CXR-Net	CT-CXR-COVID-19 Classification Network
CXR	Chest X-Ray
DCAF	Dual-Channel Attention Fusion
DCT	Discrete Cosine Transform
DDHGC	Dynamic Dual-Histogram Gamma Correction
DL	Deep Learning
DWT	Discrete Wavelet Transform
FCN	Fully Convolutional Network
FL	Federated Learning
GAN	Generative Adversarial Network
IBBO	Improved Brown Bear Optimization
IoMT	Internet of Medical Things
IoU	Intersection over Union

MSE	Mean Squared Error
MGWO	Modified Grey Wolf Optimization
ML	Machine Learning
OU-Net	Optimal U-Net
PSNR	Peak Signal-to-Noise Ratio
PSO	Particle Swarm Optimization
RMT	Memory Transformer
RT-PCR	Reverse Transcription Polymerase Chain Reaction
SARS	Severe Acute Respiratory Syndrome
SVM	Support Vector Machine
SSIM	Structural Similarity Index Measure
ViT	Vision Transformers
WHO	World Health Organization
XAI	Explainable AI

Chapter 1

Introduction

1.1 Overview

COVID-19 The disease quickly became global, with the World Health Organization (WHO) declaring it a pandemic on March 11, 2020. The main modes of COVID-19 transmission involve respiratory droplets, which was released by coughs, sneezes, or speech of infected individuals. Contact with contaminated surfaces can also be a mode of transmission. The virus has demonstrated a high rate of transmission, with an average reproductive number. This implies that the average infected individual transmits the virus to two or three others, causing cases to increase exponentially in the early stages of the outbreak [1].

The COVID-19 is characterized by a broad spectrum of mild to severe symptoms. Symptoms are typically common, such as fever, fatigue, cough, and loss of taste or smell. Some groups are more at risk, such as the elderly and those with underlying health threats like cardiovascular disease [2]. Around mid-2023, the global case fatality rate of COVID-19 is about 1-2 percent but differs by country and over time through factors like healthcare capacity and virus variants.

The global number of confirmed COVID-19 cases and deaths had surpassed 760 million and 6.8 million, respectively, as presented in Figure 1.1. The development of multiple variants such as Alpha, Beta, Delta, and Omicron, which have different levels of transmissibility and severity, has shaped the course of the pandemic. The role of vaccination campaigns in controlling the spread of COVID-19 has been critical [3]. As of mid-2023, more than 13 billion vaccine doses have been administered worldwide, with approximately 70 percent of the global population having received at least one dose.

The COVID-19 pandemic has impacted the economy and society significantly. International economies suffered considerable shrinkages, and the international monetary fund estimated a 3.5% decrease in global GDP in 2020. Unemployment rates soared and supply chain upheavals resulted in shortages of goods and services.

The pandemic also illuminated and intensified preexisting disparities, with vulnerable groups being more impacted. Governments responded by imposing several measures, including lockdowns, social distancing, and financial support packages, to alleviate the impact [4]. The pandemic increased the uptake of remote work, digital transformation, and telehealth services, which will likely influence the operation of societies post-pandemic.

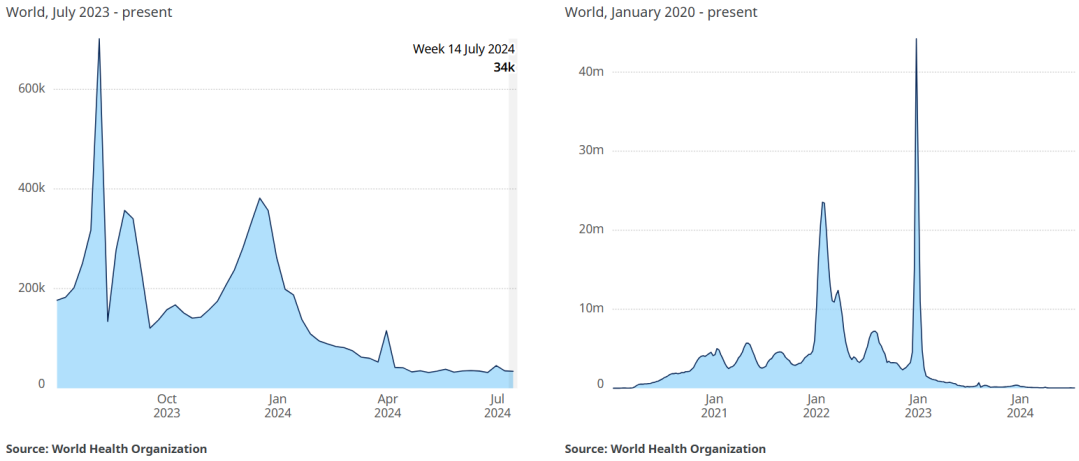

Figure 1.1. Statistics of COVID-19.

1.2 Traditional COVID-19 Screening Methods

The following section concerns the manual COVID-19 screening methodologies.

RT-PCR: RT-PCR is the most reliable diagnostic method in COVID-19 as it is sensitive and specific. This molecular test identifies the presence of viral RNA in a sample, usually gathered with a nasopharyngeal swab. The reverse transcription of viral RNA into complementary DNA (cDNA) initiates the process. Polymerase chain reactions are subsequently used to amplify the cDNA, allowing the virus to be detected at low concentrations. RT-PCR tests yield precise findings, frequently diagnosing COVID-19 infection in advance of the symptoms [5]. Nonetheless, it needs specific laboratory equipment and skilled staff, which cause delays in result delivery, particularly in times of high demand.

Antigen Testing: Rapid Diagnostic Tests, also called antigen tests are also less costly and quicker to run compared to RT-PCR, giving results within about 15 to 30 minutes.

Antigen tests have proven especially helpful in screening large populations and detecting contagious people within a short period [6]. Nevertheless, they tend to be less sensitive than RT-PCR tests, particularly in patients with low viral loads or during the initial phases of infection. False negatives are more typical, and it is necessary that negative outcomes are reconfirmed by another RT-PCR test. Antigen tests are vital in controlling the pandemic despite these drawbacks because they allow mass testing and quick isolation of infected people.

Serological Testing: Serological tests, or antibody tests, measure presence of antibodies against SARS-CoV-2 in blood. These are performed to establish whether an individual has previously been infected with the virus and not to diagnose a current infection. Serological testing can give significant information regarding the dissemination of the virus within a community and assist in identifying individuals who have developed a certain degree of immunity [7]. Nevertheless, antibodies present do not necessarily mean the body is immunized, and the longevity of the antibodies defense is under investigation. These tests cannot be used to detect existing infections because the formation of antibodies usually takes one to three weeks after infection.

Chest Imaging: Chest imaging, including CXR and CT scans, has been utilized as an additional diagnostic measure in COVID-19, especially where RT-PCR results were inconclusive or delayed. Imaging demonstrates typical features of lung involvement in COVID-19 patients, including bilateral infiltrates and ground-glass opacities. Although this is not COVID-19-specific, the findings were used to diagnose in conjunction with clinical symptoms and other tests. Chest imaging is especially practical in evaluating the severity of the disease, as well as tracking the course of the disease in hospitalized patients [8]. Non-specificity and the potential of radiation exposure limit its usefulness as a primary diagnostic tool.

1.2.1 Problems of RT-PCR, Antigen, and Serological Testing

The RT-PCR tests have certain drawbacks that can affect their usefulness in screening COVID-19. A significant problem is that they need special lab equipment and qualified personnel to perform the tests. This create bottlenecks, particularly in areas

with scarce healthcare facilities or when demand is high, leading to delayed outcomes. Furthermore, RT-PCR is subject to sample collection quality and timing. False negatives occur due to improper sample handling or collection, especially when it is prematurely or late in the infection cycle. The test is also comparatively costly and time-consuming, which restricts the accessibility and scalability of mass testing in low-resource environments.

There is a limit to the sensitivity of antigen tests, especially when it comes to identifying cases with low viral loads. This implies that they have a higher tendency to give false-negative results, particularly in asymptomatic persons or those in the early or late stages of infection. Although the antigen tests were helpful in quick screening, they are less sensitive than RT-PCR, which can result in missed cases and further transmission of the virus in case negative results are not verified by subsequent testing [9]. Additionally, the accuracy of antigen tests differs considerably across various manufacturers and test kits, thereby requiring critical selection and validation of tests in practice in the context of public health.

Serology is not the right method to diagnose active COVID-19 infections because antibodies need time to form after infection. This latency restricts their application in timely intervention and isolation of infected individuals. Moreover, the availability of antibodies does not always imply immunity, since the protective quality and longevity of antibodies against SARS-CoV-2 were unclear [10]. Cross-reactivity with other coronaviruses can also cause false positives, resulting in a possible misinterpretation of immunity status. In addition, individual immune responses and differences in test sensitivity complicate the interpretation of serological values, especially when these are used to gauge population-level immunity or inform public health decisions.

1.2.2 Advantages of Chest Imaging

Chest imaging has several strengths over RT-PCR, antigen, and serological tests. They are

Immediate Evaluation of the Disease Severity: Chest imaging, such as CXRs and CT scans, offers instant visual confirmation of lung involvement in COVID-19 patients. Chest imaging, in contrast to RT-PCR and antigen tests, can show the extent

and severity of lung damage due to disease. This is especially useful in acute clinical care, where quick grading of disease severity is essential to determine the level of care and treatment required. To illustrate, CT scans reveal early pneumonia, and healthcare professionals can provide prompt treatment.

Applicable to Symptomatic Patients who Test Negative: In certain situations, a COVID-19 patient has symptoms that are suspicious of the infection but does not test positive on RT-PCR or antigen tests because of other factors, including low viral loads or incorrect sample collection. In these cases, chest imaging can play a supplementary role in diagnosis [11]. It aids in validating a diagnosis of suspected COVID-19 by detecting typical patterns of lung abnormalities, including those related to the virus, such as ground-glass opacities and bilateral infiltrates. This is especially relevant in instances where prompt diagnostic validation is required, and other testing procedures are non-existent or impractical.

Disease Progression and Response to Treatment: Chest imaging plays a crucial role in tracking the progress of COVID-19 and its response to treatment. Repeated imaging enables clinicians to assess longitudinal changes in lung pathology, evaluate the efficacy of therapeutic interventions, and make decisions regarding plan continuation, escalation, or modification. This ability is particularly critical in more critical situations, where prompt modification of care can greatly influence patient outcomes. Although RT-PCR, antigen, and serological tests can deliver data on the presence of the virus and immune response, they cannot provide a picture of the changes which happen in the lungs in real time, which are essential to managing severe respiratory complications.

Complementary Role in Comprehensive COVID-19 Management: Chest imaging does not replace molecular or antigen testing but complements the overall management of COVID-19. It offers another layer of diagnostic information that, when integrated with test results and clinical assessment, present a more comprehensive picture of the patient status [12].

1.3 IoMT Environment

The Internet of Medical Things (IoMT) is a significant healthcare development that has gained prominence during the COVID-19 pandemic. The IoMT comprises a web of interoperable devices and applications that capture, process, and send health information as depicted in Figure 1.2. Its main strength is in improving patient care and monitoring. Remote patient monitoring enables healthcare professionals to monitor the vital signs and health status of patients, were consistent monitoring result in timely interventions and improved health outcomes. In a pandemic, remote patient monitoring reduced the risk of virus spread and provided continuity to non-COVID patients.

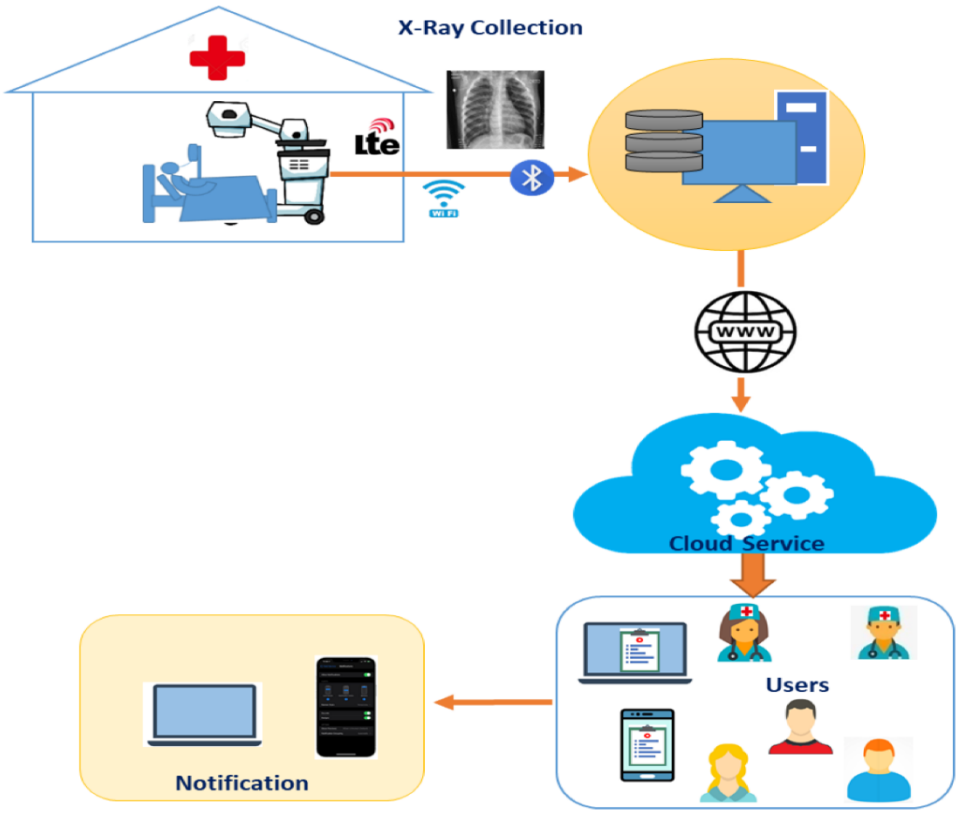

Figure 1.2. Typical IoMT Framework.

The IoMT lowers health expenses and increases system efficiency. IoMT devices minimize manual data entry by automating data collection and analysis, reducing errors and allowing healthcare professionals to concentrate on patients [13]. This automation results in quicker diagnosis and treatment, shortening hospitalization and

related expenses. As an example, smarter infusion pumps and medication administration devices make sure that drugs are delivered correctly, reducing medication errors and adverse drug events. Additionally, IoMT enables proactive maintenance of medical devices, avoiding expensive failures and securing optimal functionality. Implementation of IoMT within healthcare systems facilitates data-driven decision-making, which can contribute to operational efficiency and resource allocation.

The COVID-19 pandemic catalyzed the use of telehealth, and IoMT was instrumental in its rapid adoption. IoMT devices, facilitate the collection and sharing of health data with healthcare providers, facilitating remote consultations and interventions. This is crucial in dealing with infectious diseases, where reduction in physical contact is critical. IoMT facilitates the growth of telehealth into rural and underserved regions, enhancing access and equity in healthcare.

Moreover, IoMT-gained data were also incorporated into electronic health records [14], which offered holistic understanding of a patient health history and enabled customized treatment. The IoMT will increasingly serve to provide high-quality, efficient and accessible care as healthcare systems evolve to address the emerging challenges.

1.4 Research Motivation

Physicians have been confronted with a major challenge during the COVID-19 pandemic, especially in the early and precise identification of the virus. The first is the use of RT-PCR tests, which, though reliable, can take several hours to days to provide results because of specialized equipment and lab processing. Such latency impedes timely decision-making, particularly in emergency and high-risk scenarios where quick response is essential.

Moreover, healthcare facilities are already overwhelmed by the lack of test options at peak times of the pandemic, which has compelled physicians to triage patients and make complicated decisions about who gets immediate testing and treatment. The workload and stress of health workers have risen dramatically because of need to

rapidly and correctly diagnose COVID-19 and high number of patients under their care, combined with limited resources.

The existing COVID-19 detection approaches pose multiple challenges to patients, the first of which pertains to their accessibility and time-promptness. RT-PCR tests frequently necessitated patients to visit specific testing locations, which was difficult due to mobility concerns, geographic isolation, or the lack of accessible transportation. Waiting time of test results can lead to anxiety and uncertainty, especially among people who must quarantine or handle their symptoms without access to medical advice. Furthermore, false-negative outcomes of antigen tests contribute to undiagnosed cases, which pose a risk of passing the virus to others unknowingly. The unavailability of quick, precise, and broadly accessible testing tools can slow down treatment, extend illness, and spread the virus, intensifying the effects of the pandemic on persons and populations.

The struggles doctors and patients undergo highlight the necessity of a quicker COVID-19 detection system. Quick and precise testing can play a crucial role in handling of the pandemic by facilitating early detection and seclusion of infected parties, minimizing the transmission of the virus. More rapid detection mechanisms enable healthcare providers to start the relevant treatments in good time, enhancing patient outcomes and alleviating the burden on health care facilities [15]. Moreover, a more streamlined testing process also improves the accessibility of testing, as individuals will be able to be tested more conveniently without the logistical difficulties that they experience today. Meeting these needs, a faster detection system will be instrumental in managing the pandemic, safeguarding human health, and ensuring the restoration of both society and the economy.

1.5 Problem Statement

Several limitations are critical in manual COVID-19 screening methods such as traditional RT-PCR, antigen tests, and serological assays. A significant factor is that manual processing is time-consuming, especially RT-PCR tests, which require complex laboratory work and was subjected to lengthy analysis. Such a lag in response times can have severe implications on timely decision-making and patient

care, particularly in hectic, high-volume facilities. Furthermore, manual screening techniques typically involve physical collection of samples, which is both logistically demanding and risky, including possible contact with the virus by medical personnel and time lag in delivery to testing locations.

Issues of accuracy and reliability also plague manual screening methods. RT-PCR tests are highly sensitive but give false-negative results when the sample is not collected correctly or when the virus in the sample is present in low concentration. Though faster, antigen tests are less sensitive and more susceptible to false negatives, especially in those with low viral loads or initial infections. Serological tests, which identify antibodies, cannot diagnose active infections and was falsely positive because they cross-react with other viruses. Such constraints add to uncertainty and result in misdiagnoses, which impact patient outcomes and overall health management in society.

The existing screening procedures puts a burden on healthcare services and restricts accessibility. RT-PCR testing involves the use of specialized laboratory equipment and trained staff, which were not readily available, particularly in underserved or remote locations. This dearth worsens the wait times and lead to bottlenecks in testing capacity. Moreover, RT-PCR tests are prohibitively expensive, and large-scale testing is hampered by extensive infrastructure requirements, which make it difficult to successfully control and contain outbreaks. Accessibility is also exacerbated by the fact that patients must go to testing locations, which proved problematic with mobility problems or in places where testing was not readily available.

The combination of AI and the IoMT presents a potential solution to the constraints of manual screening systems. AI has the potential to automate and optimize many parts of the diagnostic process, including processing imaging data in CXR and CT scans. AI can detect trends and anomalies in COVID-19 cases promptly, enabling real-time data and minimizing the necessity of human interpretation. This not only accelerates the diagnostic process but also improves testing throughput, enabling quicker detection and treatment.

1.6 Research Objectives

To solve above research problems, the following research objectives are defined as follows:

- To preprocess COVID-19 CT and CXR images using BM3D filtering. To suppress noise while preserving structural and textural details for enhanced image clarity. To ensure high-quality inputs for accurate segmentation and feature extraction in downstream processes.
- To segment lung regions and COVID-19 lesions accurately using the OU-Net architecture. To optimize encoder-decoder paths and enhanced skip connections for precise delineation of pathological areas. To fine-tune network parameters with MGWO for improved convergence and robustness.
- To classify COVID-19 and Normal cases from CT and CXR images using the CT-CXR-Net. To extract deep features with ResNet50 and select the most informative features using IBBO. To provide robust and efficient classification with a Ridge Classifier, balancing bias and variance for high accuracy.

1.7 Datasets

This work implemented using both CT and CXR datasets, which enhances the robustness and novelty of the research work. Figure 1.3 shows the sample CT and CXR images for both normal and COVID-19 classes.

1.7.1 CT Scan Dataset

The CT scan dataset employed in the study is composed of high-resolution CT images of the chest aimed at COVID-19 classification. The dataset contains 1229 COVID-19 positive case images and 1229 non-COVID-19 case images to provide a balanced dataset to train and evaluate. The dataset is especially useful in training DL models since CT images reflect structural changes in lung tissue more accurately than CXR images, leading to a more accurate image of early-stage infection. The dataset is

available through Kaggle SARS-CoV-2 CT Scan Dataset and accessed via Kaggle SARS-CoV-2 CT Scan Dataset.

To conduct experimental analysis, the dataset was partitioned into training, testing, and validation groups as indicated in Table 1.1. In this case, 70 percent of the dataset is reserved to train, enabling the models to discover strong feature representations with many images. In addition, 15% was allocated to testing, which will allow assessing the generalization of the model on unseen data. The remaining 15 percent is devoted to validation, which performs hyperparameter optimization and avoids overfitting. This division guarantees the model is trained efficiently and an impartial evaluation of performance is upheld.

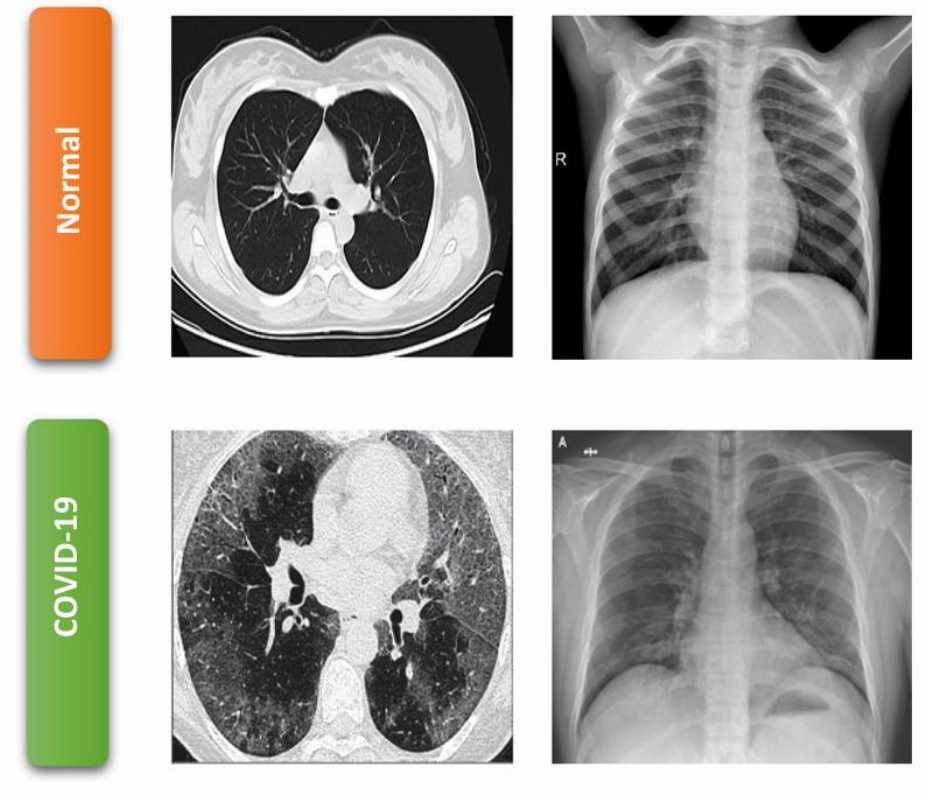

Figure 1.3. Sample CT and CXR Images of Both Normal and COVID-19.

Table 1.1. CT Dataset Distribution.

Class	Total Images	Training (70%)	Testing (15%)	Validation (15%)
COVID-19	1229	860	184	185
Non-COVID-19	1229	860	184	185
Total	2458	1720	368	370

1.7.2 CXR Dataset

The CXR dataset employed in this research is a large set of COVID-19, Normal, and other lung infection images selected by a collaborative team of researchers belonging to Qatar University, the University of Dhaka, and their international partners. The dataset contained 219 COVID-19, 1341 Normal, and 1345 Viral Pneumonia images, but later updates increased examples of the COVID-19 class and other categories considerably. The ultimate release consists of 10,973 COVID-19 positive CXR images, and 10,192 Normal CXR images, with corresponding lung masks to facilitate segmentation tasks. The dataset provides a wide range of images taken in different clinical environments, which are suitable to train DL models to classify and segment images. The dataset is available through Kaggle COVID-19 CXR Dataset. The dataset was accessed via Kaggle COVID-19 CXR Dataset.

The dataset will be divided into training, testing, and validation sets in a typical 70%-15%-15% ratio as outlined in Table 1.2 to ensure model robustness and generalizability. In this case, 70% of the images are trained and the model will be trained to learn discriminative features with both COVID-19 and Normal cases to evaluate accuracy and reliability on unseen images. The remaining 15 percent is assigned to validation, which assists in optimizing hyperparameters and makes sure the model is not overfitting during training. This partitioning plan guarantees a balanced representation of both classes in each subset.

Table 1.2. CXR Dataset Distribution.

Class	Total Images	Training (70%)	Testing (15%)	Validation (15%)
COVID-19	10,973	7,681	1,646	1,646
Normal	10,192	7,134	1,529	1,529
Total	21,165	14,815	3,175	3,175

1.8 Performance Metrics

This section provides the definition of preprocessing metrics, segmentation metrics, and classification metrics.

1.8.1 Preprocessing Metrics

Together, Peak Signal-to-Noise Ratio (PSNR), Structural Similarity Index Measure (SSIM), and Mean Squared Error (MSE) provide a comprehensive assessment of preprocessing performance.

PSNR: PSNR is a common measure of image preprocessing quality, especially when performing denoising. It compares the peak achievable pixel intensity, and the MSE between original and processed images. Here, MAX_I^2 is the maximum potential pixel intensity of the image, often 255 in an 8-bit grayscale image. is the MSE of the original (reference) and processed (denoised) images. The larger the PSNR value, the higher the quality of the image, meaning that the noise has been successfully minimized without any disregard to the important structural information.

$$PSNR = 10 \times \log\left(\frac{MAX_I^2}{MSE}\right) \quad (1.1)$$

SSIM: The SSIM measures the perceived similarity between two images based on luminance, contrast, and structural features. Here, x is the original image, y and the processed (denoised) image (and is the mean intensity of the two images), μ_x and μ_y (which are the variances) are the contrast information, the covariance between the two images (reflecting structural correlations). The constants and are little

stabilization numbers added to prevent division by zero when denominators are nearly zero. The value of SSIM lies between 0 and 1, with 1 representing ideal structural similarity. Having a high SSIM score indicates that the preprocessing algorithm manages to preserve valuable anatomical information and visual fidelity necessary to segment the lung and lesions precisely.

$$SSIM(x,y) = \frac{(2\mu_x\mu_y+C_1)(2\sigma_{xy}+C_2)}{(\mu_x^2+\mu_y^2+C_1)(\sigma_x^2+\sigma_y^2+C_2)} \quad (1.2)$$

MSE: The MSE measures the average squared error between the original image and the denoised image. In this case, M and N are the dimensions of the image (height and width, respectively), so there are total pixels. The squared difference calculates the difference in intensity of each pixel, giving higher weight to larger differences. A reduced MSE value indicates that the preprocessing method successfully reduced pixel-wise errors and conserved valuable visual information. Low MSE is a key concept in medical imaging because essential diagnostic information, like lung texture and lesions, are preserved without causing undesired noise.

$$MSE = \frac{1}{MN}\sum_{i=1}^{M} \sum_{j=1}^{N}[I(i,j) - K(i,j)]^2 \quad (1.3)$$

1.8.2 Segmentation Metrics

Together, the segmentation eight metrics provide a comprehensive evaluation of segmentation performance.

Segmentation Accuracy: Accuracy quantifies the overall accuracy of the segmentation model by measuring the proportion of pixels (or voxels) that the model classifies correctly as lesion (positive) or background (negative). In this case, True Positives (correctly identified lesion pixels), True Negatives (correctly identified background pixels), False Positives (pixels falsely labelled lesion), and False Negatives (lesion pixels falsely missed by the model). An increased accuracy translates to improved segmentation performance, but in imbalanced datasets, with the count of background pixels significantly exceeding the count of lesion pixels, this is misleading.

$$Accuracy = \frac{TP+TN}{TP+TN+FP+FN} \quad (1.4)$$

Segmentation Sensitivity: Recall, or Sensitivity, quantifies the accuracy of the model in properly detecting real lesion areas. High Sensitivity means that the segmentation network identifies most of the true lesion areas correctly. In medical image segmentation, increased Sensitivity is important as the absence of a lesion area result in a false-negative diagnosis, which negatively impacts clinical judgment.

$$Sensitivity = \frac{TP}{TP+FN} \quad (1.5)$$

Segmentation Specificity (True Negative Rate): Specificity measures how well the model correctly detects non-lesion (background) areas. High Specificity is designed so that normal lung tissue or background is not misclassified as an infected or abnormal area. The balance between Sensitivity and Specificity in segmentation of CT and CXR images is necessary to guarantee correct delineation of lesions without false alarms.

$$Specificity = \frac{TN}{TN+FP} \quad (1.6)$$

Segmentation Precision (Positive Predictive Value): Precision quantifies the correctness of positive predictions, which means what proportion of the pixels predicted as lesions are in the lesion region. High Precision implies that the model generates fewer false positives, so that the areas highlighted in the segmentation mask are true pathological regions. This measure is especially significant when reducing false alarms is critical to diagnostic accuracy.

$$Precision = \frac{TP}{TP+FP} \quad (1.7)$$

Segmentation Recall: In segmentation tasks, Recall guarantees that the model identifies the majority of the infected or abnormal lung areas. Medical segmentation wants High Recall values because missing a lesion can result in incorrect diagnosis. Recall must, however, be balanced with Precision to prevent over-segmentation.

$$Recall = \frac{TP}{TP+FN} \quad (1.8)$$

Segmentation F1-Score: It quantifies models with large Precision and low Recall, or the converse. The larger the F1-Score, the better the segmentation model was at identifying real lesions and reducing false alarms. This metric is especially relevant in medical image segmentation, where under-segmentation and over-segmentation can influence diagnosis.

$$F1\text{-}Score = \frac{2\times Precision\times Recall}{Precision+Recall} \quad (1.9)$$

Segmentation Jaccard Index (IoU): A higher Jaccard value (closer to 1) indicates better agreement between prediction and ground truth. This metric is widely used for evaluating segmentation accuracy in medical images, including lung and lesion segmentation.

$$Jaccard = \frac{|A\cap B|}{|A\cup B|} = \frac{TP}{TP+FP+FN} \quad (1.10)$$

Segmentation Dice Score: The dice score is a 0 to 1 scale, with 1 corresponding to perfect overlap. It is especially applicable to medical segmentation problems, including lung and lesion detection, since it directly measures spatial similarity. A steep Dice Score indicates the model fits the lesion boundaries with a small error.

$$Dice = \frac{2|A\cap B|}{|A|+|B|} = \frac{2TP}{2TP+FP+FN} \quad (1.11)$$

1.8.3 Classification Metrics

Together, the classification metrics provide a comprehensive evaluation of the COVID-19 vs Normal image classification performance.

Accuracy: In COVID-19 classification, Accuracy quantifies the overall proportion of correctly classified images both COVID-19 and Normal, which relative to the total number of test samples. Here, TP represents the number of correctly classified COVID-19 images, TN denotes correctly classified Normal images, FPcorresponds to Normal images incorrectly labeled as COVID-19, and FN refers to COVID-19 images misclassified as Normal. High Accuracy means the classification model, e.g., the proposed CT-CXR-Net, is effective in differentiating between infected and non-infected cases. But the accuracy alone does not fully capture performance in imbalanced datasets, so other measures are needed to enable a complete assessment.

Precision: Precision is used to assess how many true COVID-19 cases the model identifies. This plays a vital role in medical diagnostics to avoid premature alarms and misleading patients of false COVID-19 positivity.

Recall: Recall (equivalent to True Positive Rate) is a metric that evaluates how effectively the model identifies all the true COVID-19 cases present in the dataset. This is particularly crucial in medical contexts where a missed COVID-19-positive case delay treatment or transmission control.

F1-Score: F1-Score: F1-Score is a balanced score, a combination of Precision and Recall that gives a single performance measure. It is the harmonic average between these two measurements. An increased F1-Score indicates that the classifier is effective in the accurate detection of COVID-19 cases and has low rates of both false classification and false negative.

1.9 Simulation Environment

Table 1.3 describes the software and hardware specifications employed in the study and the cross-validation strategy employed to evaluate the model. Python 3.7.6 is the main programming language used on the software side, being one of the most popular programming languages in ML and medical image processing because of its simplicity, readability, and rich library ecosystem. The research uses a range of major supporting libraries, such as TensorFlow 2.0 to create and test DL models, OpenCV to process and manipulate images, Scikit-learn to design and evaluate classical ML models, Matplotlib to plot and visualize results, and Pandas to handle and preprocess data efficiently. This combination offers a versatile, highly performant environment that can drive both the preprocessing and segmentation operations effectively.

Table 1.3. Software and Hardware Environment with Cross-Validation.

Category	Specification	Details
Software	Programming Language	Python 3.7.6
	Supporting Libraries	TensorFlow 2.0.0, OpenCV, Scikit-learn,

		Matplotlib, Pandas
Hardware	Processor (CPU)	Minimum: Intel Core i5 (8th Gen)
	RAM	Minimum: 16 GB
	Storage	Minimum: 512 GB SSD
Cross-Validation	Strategy	k-Fold Cross-Validation
	Number of Folds	10 folds (80% training, 20% testing per fold)

On hardware, the study defines a minimum processor requirement of Intel Core i5 (8th Generation), providing enough computational capabilities to train and infer DL models with reasonable delays. It is suggested that a minimum of RAM of 16 GB is necessary to load and process high-resolution medical images like CT and CXR scans, which often require substantial memory resources during preprocessing, patch extraction, and batch training. It has 512 GB SSD storage, which offers high read and write speeds on large datasets, model checkpoints, and intermediate data storage, and helps mitigate I/O bottlenecks during model training and evaluation. This hardware configuration guarantees that experiments are conducted effectively, even on high-dimensional medical image data.

To evaluate, the table emphasizes the cross-validation strategy, namely, k-Fold Cross-Validation with 10 folds. This approach enables a powerful evaluation of model performance, reduces biases based on data partitioning, and enhances generalization. The study introduces an additional element of k-Fold Cross-Validation to guarantee that the performance metrics reported are representative of the model reliability on various subsets of the dataset, increasing the credibility and reproducibility of the experimental outcomes.

1.10 Organization of Thesis

Chapter 1 provides an overview of the COVID-19 pandemic and its global impact, highlighting the importance of timely diagnosis. It discusses the role of CT and CXR imaging in detecting lung abnormalities associated with COVID-19. The chapter also outlines the challenges in manual diagnosis and motivates the need for automated classification methods.

Chapter 2 reviews existing research on COVID-19 detection using CT and CXR images. It examines various preprocessing, segmentation, and classification techniques employed in previous studies. The chapter identifies gaps in current methods, particularly in noise suppression, segmentation accuracy, and classification efficiency.

Chapter 3 focuses on the implementation of BM3D for image denoising. It details how BM3D preserves structural and textural details in CT and CXR images. The chapter also evaluates the effectiveness of BM3D in enhancing image quality for subsequent segmentation and feature extraction.

Chapter 4 presents the design and implementation of the OU-Net architecture. It explains the adaptive encoder-decoder paths, enhanced skip connections, and MGWO-based parameter optimization. The chapter highlights the segmentation results, focusing on accurate lung region and lesion delineation.

Chapter 5 describes the CT-CXR-Net for automated COVID-19 vs Normal classification. It details deep feature extraction using ResNet50, feature selection via IBBO, and classification using a Ridge Classifier. The chapter also presents performance metrics, comparison with existing methods, and analysis of classification results.

Chapter 6 summarizes the research findings and highlights the advantages of the proposed methodology. It discusses limitations, practical implications, and contributions to automated COVID-19 detection. The chapter also suggests future directions, including integration of additional imaging modalities and real-time clinical deployment.

Chapter 2
Literature Survey

2.1 Introduction

The last ten years have witnessed an explosion in medical imaging and AI research, with a particular interest in image preprocessing methods in modalities like CT and CXR scans. Preprocessing techniques have progressed beyond classical image enhancement and noise-reduction filters to advanced DL-based transformations, data augmentation, and lung region isolation techniques. Indicatively, a recent review indicates that most of the COVID-19 imaging research has implemented preprocessing methods such as augmentation, HE and lung segmentation as essential facilitators of consistent classification. Through a systematic review of these advancements, one will understand how preprocessing prepares downstream segmentation and classification tasks, not just by enhancing image quality, but also by aligning heterogeneous datasets, reducing artefacts, and maintaining structures that are diagnostically relevant.

Automated diagnostic pipelines rely on segmentation and classification, with classical methods of thresholding, region-growing, and deformable models giving way to deep networks like Fully Convolutional Network (FCN), U-Net, attention-based networks and transformer-based models. CNN and transfer learning models have become popular on the classification side to differentiate between COVID-19, viral pneumonia, and normal chest images, with recent surveys highlighting the significance of feature extraction, model generalization, and robust evaluation. Using this literature survey, gaps are identifiable, including but not limited to segmentation robustness in diverse imaging conditions, feature selection to classify the image, and connecting preprocessing to end-to-end pipelines.

2.2 Related Work on Preprocessing Methods

Clement David-Olawade et al. [20] offered a review of AI-assisted low-dose imaging methods, with a particular emphasis on CT, CXR, and magnetic resonance imaging (MRI). The authors emphasized the progress in DL models, specifically CNN, to

improve image quality and reduce radiation doses considerably. They talked about different AI-based methods that can facilitate low-dose imaging protocols, and they seek to harmonize diagnostic accuracy and patient safety. One of the shortcomings of their review is the fact that the discussed AI techniques were not empirically validated or compared, which prevents the evaluation of their practical efficacy in clinical practice.

AN bin Azhar et al. [21] assessed how various image preprocessing methods affect the performance of DL models in detecting COVID-19 with CXR images. The authors evaluated the impact of different preprocessing techniques on the accuracy of DL models in classifying CXR images, with the aim of enhancing diagnostic results. One limitation of their study is the lack of a specific examination of the computational efficiency and scalability of the preprocessing methods within a real-world clinical setting.

AM Arul Raj et al. [22] created a deep CNN system to identify COVID-19 on CXR images. The authors also tackled the issue of scarce high-quality datasets by using image preprocessing measures to improve the quality of training data. Their strategy was to enhance the model to better classify CXR images, which lead to more effective COVID-19 diagnosis. One of the limitations of their method is that they use one dataset, which can impact the applicability of the model to various patient groups and imaging scenarios.

Esraa Hassan et al. [23] suggested a methodology to identify COVID-19 in CT images with multiple pre-trained models. Their methodology involved transfer learning with deep CNNs, applying models like ResNet, VGG, and Inception to categorize CT images into positive and negative COVID-19. One of the constraints of their research is that they used numerous pre-trained models without adequate regularization methods, which lead to overfitting and affect the performance of the model on unseen information.

Ajay Mittal et al. [24] presented a deep residual learning-based denoising architecture on medical CXR images. To train the denoising model, the authors used deep residual learning methods, emphasizing the preservation of valuable features and removing

noise. Their model has one weakness: the training of deep residual networks is computationally complex, which was problematic in terms of both processing time and resource costs in clinical environments.

A methodology of denoising and improving the quality of CT and CXR images of lung diseases was proposed by N. Anitha et al. [25]. Their method employed a blend of image processing algorithms, such as contrast enhancement and smoothing, to enhance the diagnostic clarity of medical images. The authors used these techniques on both CT and CXR images to enable easier detection and analysis of lung diseases. They also have a limitation in that they do not extensively analyze the computational efficiency and scalability of the proposed techniques in real-world clinical environments.

Devanand Bhonsle [26] wrote about different ways of silencing noise signals in the medical imaging field, with special attention to CT and ultrasound images. He discussed the addition of noise in these imaging methods and has looked at many methods of reducing signal noise, so that proper diagnosis was made. The chapter presented a summary of various noise suppression measures and performance considerations. One of the limitations of his review is that there are no specific comparative analyses of the various noise suppression methods, which was helpful in identifying the most effective approaches to medical imaging situations.

A noise reduction and super-resolution approach based on transfer learning was proposed by K. Lokeshwar Reddy and G. Bharathi Mohan [28] to improve medical imaging. Their method used pre-trained DL models to minimize noise and maximizing resolution, thus contributing to more accurate medical diagnosis. The authors used this methodology on medical images to illustrate its effectiveness. Their study has a limitation in that it does not provide a detailed analysis of how the method was generalized to various types of medical imaging modalities and datasets.

J.H. Jensha Haennah et al. [29] designed a hybrid Universal Net (U-Net) and CNN image classification system to identify COVID-19 based on CXR and CT images. Their model combined U-Net to segment the images and CNN to classify them, hoping to enhance the accuracy. Their method has a weakness in that it can overfit

because it uses only one dataset, and this can influence the performance of the model on other real-world data.

Valantina Stephen et al. [30] suggested a noise reduction technique based on CNNs plus Discrete Wavelet Transform (DWT) to improve CXR imaging. Their solution was to minimize noise in CXR images, thus minimizing radiation exposure without compromising the quality of images to facilitate accurate diagnosis. The authors used this approach on CXR images to show its efficiency. Their study has a limitation in that it does not provide a thorough evaluation of the trade-off between noise reduction and maintenance of essential diagnostic features in images.

S. Kushwaha et al. [31] introduced superior noise filtering algorithms to enhance medical images. Their strategy involved using both spatial and frequency domain filtering techniques to successfully remove noise in medical images, thus enhancing image quality to better diagnose. The authors tested these techniques on a range of medical imaging modalities to prove their effectiveness. They also have a limitation in that they do not extensively analyze the computational efficiency and scalability of proposed techniques in clinical environments.

S. Rajaraman et al. [32] designed a modality-specific pretext learning model in pediatric CXR image classification. Their methodology involved image denoising and deblurring to improve the quality of CXR images and then used a VGG-16-Sharp-U-Net architecture to classify the images. This approach was intended to enhance the precision of labeling pediatric CXR images as normal or abnormal. One of the limitations of their method is that they used only one dataset, which can restrict the applicability of the model to various pediatric populations and imaging scenarios.

S. Chauhan et al. [33] proposed a U-Net architecture augmented with ResNextify and inverted bottleneck modules to denoise low-dose CT images. The authors provided evidence of the effectiveness of their approach by conducting experiments on publicly available datasets. Their study has a weakness in that it does not provide detailed analysis of how the model performs on various CT scanners and imaging protocols, which impact its use in diverse clinical environments.

K. Mori et al. [34] aimed to assess the minimization of radiation dose in chest radiography with DL-based noise reduction processing. They sought to enhance the quality of images and reduce the amount of radiation exposure to patients, thereby increasing the safety and efficacy of chest radiography. The researchers used DL to process and improve the quality of chest radiographs. One of the limitations of their research is that there is no detailed evaluation of the long-term clinical consequences of the lower radiation dose during chest radiography.

W. Bocquet et al. [35] examined the detection of pulmonary nodules on ultra-low dose chest CT with a DL image reconstruction algorithm. Their goal was to test the efficacy of DL-based reconstruction methods in identifying pulmonary nodules with lower radiation doses, thus enhancing patient safety without reducing diagnostic quality. The authors contrasted the performance of their algorithm with conventional reconstruction methods. One of the weaknesses of their study is the absence of a thorough examination of the algorithm performance in various categories of pulmonary nodules and patient demographics, which can potentially influence its applicability.

Mst Jannatul Kobra et al. [36] compared the performance of Fourier, Wiener, Bilateral, Histogram Equalization (HE), and Contrast Limited Adaptive HE (CLAHE) image denoising algorithms to reduce noise in CT scans. Their analysis showed that bilateral filtering was more effective than other methods in maintaining image quality and effectively reducing noise, and it is a reasonable option in clinical practice. Their study has a weakness in that it lacks a thorough assessment of the computational efficiency and scalability of the proposed methods in actual clinical environment.

A. Pearly and B. Karthik [37] presented lung image enhancement method based on Dynamic Dual-Histogram Gamma Correction (DDHGC). Their method combined adaptive gamma correction with HE to make lung images more visible, with the aim of making lung structures better visible to improve diagnosis. Their approach has a disadvantage in that it does not provide a thorough examination of the computational complexity and real-time practicality of the DDHGC technique in clinical settings.

Dorsaf Hrizi et al. [38] optimized classification of lung nodules by refining CT images with CLAHE and deep feature extraction with Swin Transformer. Their approach was to enhance precision in detecting lung nodules by optimizing image quality and deriving robust features to classify them. Their method has a weakness in that it can overfit because it uses only one dataset, and this can influence the performance of model on other real-world information.

Dennis Hein [39] investigated the use of DL to perform denoising in CT and CXR imaging. His work was dedicated to the creation of DL models to solve multiple problems in medical imaging, improving image quality and automating radiological reporting. One of the limitations of his work is that it does not provide a thorough assessment of the generalizability and clinical applicability of the suggested DL models to various medical imaging modalities and datasets.

2.3 Related Work on Segmentation Methods

Ilesanmi et al. [40] presented a systematic review of three-dimensional CNN (3D-CNNs) to identify COVID-19 by analysing medical imaging modalities. The research design investigated spatiotemporal feature extraction in both CT and CXR datasets to enhance diagnostic accuracy. They combined residual and dense connectivity to preserve hierarchical spatial features with minimal vanishing gradients. The review examined volumetric convolution operations and contrasted them with two-dimensional architectures based on precision and computation requirements. It tested transfer learning strategies, optimization functions, and regularization techniques that increased the strength of COVID-19 classifiers. The work also highlighted benchmark comparisons based on public datasets and addressed future scalability of the networks. Nevertheless, the study did not involve empirical implementation and performance validation on actual clinical data.

Riyono et al. [41] suggested a literature-driven review of CNN architectures used in segmentation and classification of lung medical images. The methodology involved determination of effective encoder and decoder architectures including Universal Net and SegNet, which facilitated automatic extraction of the lung boundaries. They tested hybrid learning frameworks that integrate thresholding-based pre-processing

and CNN-based pixel-level classification. The authors classified different network topologies by their accuracy, layer depth, and reuse of features when working with medical imaging datasets. To identify the best activation and loss functions to detect lesions, comparative analysis was conducted. The review standardized methods that traded off computational cost and segmentation accuracy. But the research was theoretical and lacked implementation details and quantitative performance results.

Enshaei et al. [42] introduced a DL model to difference between COVID-19 and viral pneumonia based on baseline chest radiographs. The model utilized a convolutional backbone to extract features and a multi-reader validation strategy. It added class-weighted training to address imbalanced data and minimize false negatives. The system employed attention-guided scoring layers to predict disease severity in terms of radiographic opacity and texture variation. Statistical measures of agreement were used to evaluate comparative performance against the interpretations of several radiologists. The suggested architecture showed high diagnostic consistency in patient cohorts. Nevertheless, the model was found to have limited generalization to unseen radiographic datasets.

Prabhu and Thyagharajan [43] introduced a multimodal image fusion model that fused CT and CXR images. The methodology initially optimized image contrast by edge-preserving diffusion filtering to maintain structural integrity. It then implemented feature fusion using a weighted transform model that combined textural and intensity information across modalities. The physics-informed neural network combined loss terms that addressed gradient smoothness and intensity preservation. The hybrid model was designed to enhance the visibility of infected areas to detect COVID-19 accurately. The authors tested the fusion model using various multimodal datasets to maintain robustness. Nonetheless, the method was computationally complex with multi-source data fusion and personalized loss optimization.

The Sine-Cosine Algorithm is a medical image segmentation technique that was enhanced by Zhu and Zhang [44] through the introduction of nonlinearity-based diversity control. The methodology maximized the search by dynamically varying the amplitude and frequency of the sine-cosine operators. They added an adaptive weighting parameter to balance exploration and exploitation in the refinement of

segmentation boundaries. The algorithm incorporated fuzzy entropy-based fitness assessment to maintain region homogeneity and edge accuracy. It was compared to more traditional metaheuristic algorithms to show faster convergence and more accurate segmentation. The validation of performance was conducted with several biomedical imaging datasets. Nevertheless, the algorithm was not immune to parameter sensitivity, which influenced the stability of segmentation in various image modalities.

Roberto et al. [45] suggested a poly algorithm that exploited percolation characteristics to classify COVID-19 based on CXR images. The approach derived percolation-based structural descriptors that reflect the connectivity of infected lung tissues. Polynomial mapping was used to model the extracted features to represent nonlinear changes in intensity related to infection spread. The classification phase utilized supervised learning models that were trained on augmented datasets to improve the reliability of predictions. They tested various order of polynomials to strike a balance between accuracy and the risk of overfitting. Experimental evidence showed competitive performance against DL models on small data. Nevertheless, the method was not flexible to large-scale data and intricate feature interactions.

Mustapha et al. [46] introduced an attention U-Net to achieve precise segmentation of lung regions and infection areas in CXR and CT images. The methodology used attention gates that selectively highlighted clinically relevant spatial features during upsampling. The architecture maximized encoder-decoder links with residual fusion blocks to maintain boundary accuracy and texture features. To handle class imbalance and enhance edge delineation, they used a hybrid loss function that incorporated Dice and focal losses. Pretrained weights transfer learning improved model generalization and accelerated convergence. To achieve reliability, extensive assessments were conducted on multi-center COVID-19 imaging datasets. Nevertheless, the model required considerable memory and processing power, which restricted it to low-power diagnostic systems.

Bhongale et al. [47] introduced a hybrid model that integrates a patch-based Universal Net with a modified SqueezeNet-PyramidNet to jointly segment and classify tuberculosis, pneumonia, and COVID-19. The patch-based Universal Net used region-

specific analysis to extract localized spatial features, and the MSqueezeNet-PyramidNet operated on hierarchical multi-scale representations. The segmentation results informed the classifier to differentiate diseases correctly using region-specific features. Transfer learning and data augmentation techniques enhanced the network flexibility to different image qualities. The approach was tested on large chest imaging datasets and achieved significant accuracy and precision. The patch-wise segmentation method, however, added inference time and created discontinuities at the boundaries of regions.

Bhardwaj and Kaur [48] introduced DLSAC-Net, a two-level segmentation and classification framework to detect lung disease in CXR images. The architecture incorporated deep residual encoding layers and a spatial attention mechanism to sharpen boundaries of infected regions. The generated segmentation block produced region masks that directed the classification module to identify the disease. Long-range dependencies were captured through a context aggregation layer to improve diagnostic accuracy. The model training employed a hybrid optimization approach that combined adaptive learning rates and regularization. Public COVID-19 dataset evaluation showed high accuracy and interpretability over baseline methods. Nevertheless, the model performance deteriorated with extreme illumination changes and low-contrast images.

Yadav and Singhai [49] suggested a better multiclass classification of lung disease with image segmentation and DL in CXR analysis. The segmentation step used a narrowed Universal Net to isolate lung fields and block background noise. The extracted features were then fed to a CNN classifier trained with stochastic gradient descent and early stopping. The network architecture improved inter-class separability and minimized misclassification between pneumonia and COVID-19. Normalization and augmentation of data guaranteed consistent performance on heterogeneous datasets. Relative analysis revealed better classification accuracy than conventional DL models. Nevertheless, the model was less robust when trained on small and skewed datasets.

Bahroun [50] introduced a two-parallel-step CNN architecture to detect COVID-19 through segmented CT and CXR images. The initial stage was lung segmentation with

a lightweight Universal Net, and a parallel classification network that examined the segmented areas. The design maximized feature discriminability by isolating infection-specific patterns and reducing irrelevant background effects. The combination of multi-modal outputs enhanced reliability of decisions in complex cases. The research demonstrated high diagnostic accuracy in a variety of publicly accessible datasets. The dual-step pipeline, however, made systems more complex and required more time to train since each model is optimized separately.

Orenc et al. [51] introduced an automatic segmentation model of CXR images based on improved versions of the Universal Net model. The methodology incorporated deep-enhanced versions of U-Net, such as residual, attention, and dense connectivity modules to extract intricate anatomical features. The skip connections helped to recover finer details in upsampling, enhancing boundary delineation. A hybrid loss that incorporated binary cross-entropy coefficients improved segmentation performance on a variety of image datasets. Quantitative assessments verified substantial accuracy improvements compared to conventional encoder-decoder models. Nevertheless, the model demonstrated reduced efficiency with low-resolution or noisy radiographs.

Gtifa et al. [52] suggested a nature-inspired multi-level thresholding method combined with a CNN to classify COVID-19 and other lung diseases precisely. The methodology employed optimum threshold levels in image segmentation. The segmented images were presented to a CNN classifier that was trained to identify hierarchical texture, and shape features useful in disease detection. Multi-level thresholding was integrated to enhance contrast in features and minimize false classifications. The framework was cross validated against several benchmark datasets to verify robustness. The process of classifying involved feature selection and parameter tuning to maintain computational stability. Nonetheless, the method was overly dependent on parameterization, which caused instability in convergence in some cases.

Vinothini and Niranjana [53] introduced a more complex image segmentation and severity prediction model that integrates the normalized Universal Net (nnU-Net) with a more optimized Faster Region CNN-based Gradient-based Jaya Search (FRCNN-

GJS) algorithm. The nnU-Net module achieved automatic segmentation in the absence of manual architectural optimization, successfully isolating infected areas. The FRCNN-GJS module identified and labeled severity levels using region-specific lesion features. The GJS algorithm improved the accuracy of detection and reduced unnecessary calculations. The system demonstrated high accuracy and computational efficiency on various COVID-19 imaging data. The hybrid structure enhanced reliability of decisions in multi-severity assessment. Nonetheless, the two-stage architecture added complexity to implementation and consumed large hardware resources to train.

Mehta et al. [54] introduced a MultiResUNet-based DL model to perform precise lung segmentation using CXR images. The architecture used multi-resolution convolutional blocks, which simultaneously learned fine and coarse features at different scales. Remaining ties reduced gradient vanishing and speeded up training. The model employed data normalization and augmentation to enhance generalization across different datasets. A dynamic learning rate schedule optimized weight changes to maximize feature retention. Experimental setup achieved high segmentation accuracy and boundary reconstruction smoothness with respect to baseline U-Net models. Nevertheless, the network was less precise in dividing overlapping pathological areas.

Herng et al. [55] suggested a clustering-based segmentation method in analyzing COVID-19 CXR data with variant k-Means algorithms. The methodology involved the comparison of standard, fuzzy and adaptive k-Means clustering to determine which one was most effective in isolating infection regions. Segmentation was preceded by preprocessing to enhance contrast and remove background noise. Morphological operations in post-processing were used to refine boundaries and remove spurious regions. The analysis focused on parameter sensitivity analysis to enhance segmentation strength. Experimental validation proved that adaptive k-Means yielded higher region homogeneity and structural clarity. Nevertheless, clustering-based techniques were vulnerable to noise and not represent irregular lesion shapes accurately.

Kang et al. [56] introduced a segmentation-aided fusion-based classification system of automated CXR image analysis. The framework incorporated a segmentation module that separated lung regions with a modified Universal Net and then passed them into a fusion-based classifier. The fusion model integrated intensity, texture, and edge-based characteristics across several convolutional layers to enhance diagnostic accuracy. The system optimized the boundaries of classes based on an adaptive weighting strategy to balance healthy and diseased samples. Normalization and augmentation of data strengthened the generalization of models. The system was validated through extensive experiments on various publicly available COVID-19 datasets. The fusion architecture, however, involved complicated preprocessing and tuning to ensure cross-dataset consistency.

Din et al. [57] presented CXR-Seg, a DL model that segments lung effectively on CXR images. The model introduced an encoder-decoder model with depth wise separable convolutions to lower the computation cost without compromising segmentation accuracy. Skip connections maintained spatial data between encoding and decoding steps, enhancing recovery of structural detail. The network utilized a hybrid loss that optimizes on binary cross-entropy and IoU-based metrics. Pretrained weights transfer learning increased segmentation accuracy and accelerated convergence. The suggested model was more efficient with large datasets. Nevertheless, accuracy of segmentation was reduced with severe pathological occlusions in the lung regions.

Biju and Patel [58] suggested a DL-based segmentation model to enhance COVID-19 detection on CXR images. The methodology used a multi-level Universal Net that narrowed the infection boundaries by gradually extracting features. A CNN classifier analyzed segmented regions, distinguishing between diseases. To achieve generalization, the authors optimized the feature extraction layers with batch normalization and dropout. The model demonstrated high sensitivity and accuracy on multi-institutional datasets. Comparative study proved its superiority to baseline architectures. Nevertheless, the model exhibited reduced performance when using low-contrast or motion-blurred images.

Kumari et al. [59] offered a hybrid diagnostic model using a WHO-inspired k-Means segmentation algorithm and a VGG19-SVM model. Infected lung regions were segmented using the intensity thresholds based on WHO imaging criteria. A fine-tuned VGG19 network was used to extract features based on the segmented regions, which were then classified by an SVM layer. This hybrid method enhanced the interpretability of features and classification accuracy. Its consistency in identifying COVID-19 was verified by cross-validation across several datasets. But scalability was limited by strong dependence on manually tuned threshold parameters.

Slika et al. [60] introduced a parallel Vision Mamba and attention-based architecture to predict pneumonia severity using CXR. The model utilized segmented lung replacement augmentation to balance training samples and enhance robustness against overfitting. The Vision Mamba block acquired global dependencies, and the attention mechanism narrowed spatial attention to infection regions. The framework produced continuous severity scores that were correlated with clinical indicators. The hybrid design showed less accuracy in pneumonia and COVID-19 severity testing. But the model had training instability because parallel branches were optimized simultaneously.

AO-TransUNet, a multi-attention optimization network, was proposed by Qi et al. [61] to address COVID-19 and general medical image segmentation. The architecture combined Transformer encoders with convolutional decoders to learn global and local dependencies. Attention optimization blocks improve attention on infection-specific features and minimize background interference. The model used a composite loss function that combined Dice, focal, and boundary losses to enhance segmentation fidelity. Tests on diverse biomedical datasets validated high performance relative to conventional convolutional networks. The hybrid transformer-CNN model delivered a balanced accuracy and efficiency. Nevertheless, the model was computationally intensive to train, with multi-attention and transformer modules.

Alaoui Abdalaoui Slimani and Bentourkia [62] established an enhanced Universal Net++ model that involved DWT and attention gate types to achieve effective pathological lung segmentation. The wavelet decomposition retained multi-resolution frequency components that are important in isolating regions of infection. Attention

gates were used to selectively filter noise and highlight pertinent spatial features in the reconstruction process. The adjusted skip connections enabled improved gradient propagation between layers. The hybrid nature of the model resulted in improved performance on large-scale COVID-19 imaging datasets. Extensive comparison with other U-Net variants confirmed its segmentation accuracy. But the wavelet decomposition was more costly in terms of preprocessing time and stability demanded fine parameter tuning.

Su et al. [63] introduced COVSeg-VLM, a vision-language model that enables effective segmentation of COVID-19 infections in CXR images. The architecture integrated image encoders paired with textual embeddings based on clinical annotations to inform segmentation. Vision-language alignment layers provided a uniform correspondence between radiological patterns and semantic descriptions. The model employed a transformer-based decoder to refine boundaries and interpret context. Multimodal datasets were trained to enhance cross-domain robustness and interpretability of the model. Quantitative analysis showed better accuracy in identifying infection regions. Nonetheless, reliance on textual annotations limited scalability to unlabeled or limited-label data.

2.4 Survey on Classification Methods

A systematic review on transfer learning methods to classify CXR images to diagnose COVID-19 was proposed by Mallick et al. [64]. The work examined several pretrained convolutional models including VGG, ResNet, and Inception models to extract features. It tested fine-tuning, layer freezing, and data augmentation practices to enhance classification accuracy. The review compared model performance on varying datasets and highlighted how feature reuse helps in generalization. It also explored interpretability approaches to model transparency and bias reduction. Quantitative data were summarized to outline the best configurations to adapt to clinical settings. The review, however, was not experimentally validated to support comparative findings with real-world implementation.

Yasin [65] suggested an elaborate review emphasizing the use of CNN in detecting pneumonia and COVID-19. The paper examined CNN-based diagnostic model

development and grouped them according to depth, activation functions, and optimization techniques. It explored preprocessing techniques like HE and contrast enhancement to enhance image clarity. The review evaluated hybrid architectures that incorporate CNNs with conventional classifiers to enhance reliability. Trends in comparative performance across datasets were presented with focus on computational efficiency. The results revealed difficulties in balancing accuracy and interpretability. Nevertheless, the review provided a sparse coverage of sophisticated hybrid DL models beyond CNN architectures.

Lin and Fang [66] introduced a transfer learning-based model to estimate intensive care unit (ICU) admission among COVID-19 using CXR images. The architecture utilized pretrained convolutional networks like DenseNet and EfficientNet to extract features. Extracted features were optimized using a fully connected layer regularization to avoid overfitting. The classification module forecasted the likelihood of ICU admission using imaging biomarkers. Learning rate schedulers and adaptive optimizers were used to ensure convergence stability in model optimization. Hospital dataset validation showed high sensitivity in critical case prediction. Nevertheless, the model relied solely on imaging data without combining clinical or demographic variables to support decisions comprehensively.

Rajpoot et al. [67] suggested a comparative evaluation of Explainable AI (XAI) techniques in COVID-19 classification based on CXR images. The analysis compared saliency-based, Grad Class Activation Mapping (CAM), and Layer-wise Relevance Propagation methods to visualize decision boundaries in DL models. Interpretability, localization precision, and computational overhead were measured by quantitative and qualitative analyses. The methodology recognized XAI methods that best emphasized pathological areas that most accurately matched model predictions. Outcomes reflected better clinical trust and transparency in diagnostic decisions. Cross-validation provided uniformity across varying neural architectures. Nevertheless, the assessment was not temporal or multi-modal validation to determine robustness in imaging variations.

Hammad et al. [68] introduced a XAI model of lung cancer detection in a custom CNN model. The model derived deep spatial features that captured lesion morphology

and variations in tissue density. Activation maps were visualized using integrated XAI components to facilitate interpretability and assist radiologists in making sense of model explanations. The framework utilized regularization and transfer learning to enhance classification accuracy on small datasets. Training stability was supported by feature refinement using dropout and normalization. Experimental analysis showed high performance relative to current CNN models. Nevertheless, the framework demanded substantial computational resources because of high-resolution CT image processing.

Rao et al. [69] employed a stacked convolutional network with several residual blocks to learn fine-grained infection patterns. Data augmentation and normalization strategies mitigated against overfitting and enhanced robustness to dataset variations. Global average pooling was used to perform feature aggregation to minimize the number of parameters without compromising discriminative capacity. High accuracy and recall in early-stage infection detection were validated by model evaluation on benchmark datasets. Training used Adam optimization to converge efficiently. Nonetheless, the system was less precise in handling radiographs with overlapping pathologies or artifacts.

Paulretnam et al. [70] introduced a real-time diagnostic model of lung infections based on CXR imaging. The approach used a pre-trained CNN architecture to extract features combined with a lightweight classifier to make quick decisions. Preprocessing occurred in real time to increase contrast and reduce noise prior to classification. The pipeline was built to facilitate automated analysis in clinical and telemedicine settings. The framework achieved near real-time inference speeds and acceptable diagnostic accuracy. Continuous monitoring reliability was verified through performance evaluation.

Nevertheless, the method sacrificed classification accuracy in low-quality or limited-light imaging.

Li and Huang [71] introduced ResGDANet, a sophisticated medical image classification architecture. They developed two new modules based on the ResGANet framework: the Dual-Channel Attention Fusion (DCAF) module and the Retention-

Memory Transformer (RMT) module. The RMT module exploits memory retention to learn long-range dependencies, enabling better propagation of features across layers. This fusion is intended to enhance the model capability to identify complex features in medical images. Nonetheless, the sophistication of these modules results in higher computational needs, which affect the real-time applicability.

Alhafiz and Basuhail [72] examined how data heterogeneity affects the performance of Federated Learning (FL) systems. They tested seven different heterogeneity contexts and compared models based on generalization. The need to trade off global generalization and local adaptation in FL models. Although their work presents important insights, the use of simulated heterogeneity is not sufficient to reflect the complexities of clinical data variability in the real world.

Patnaik, Mohanty, and Subudhi [73] developed a DL model to classify COVID-19 using ReSqNet. They did it by applying a model called ReSqNet50, and the model was found to be accurate at 96.9 percent, which is encouraging in differentiating between these categories.

Olowolayemo et al. [74] concentrated on forecasting COVID-19 mortality risk with a small set of CXR images. They utilized a DL framework built on the ResNet-18 and effectiveness of the model in estimating mortality risk under conditions of limited data access. Although the findings are encouraging, the limited size of the dataset can cause overfitting, which impacts the strength and generalizability to larger clinical environments.

Thilagavathi et al. [75] proposed a hybrid DL model to classify COVID-19 in CXR images effectively. Their approach used a combination of DL techniques to identify lung-related conditions. The method proved to be effective in classification of COVID-19 cases, but the study failed to identify the specific methodologies or architectures used, which requires further research to determine the reproducibility and scalability of the proposed framework.

Agarwal and Arya [76] proposed CXRNet, a CNN with a built-in attention mechanism to classify CXR images. The architecture combines a CNN backbone with a dual-path attention module that focuses on both spatial and channel-wise features.

The purpose of design is to improve the relevance of the model to the areas of interest in the CXR images and increase diagnostic accuracy. The method was tested on publicly available CXR datasets, showing competitive performance. Nevertheless, the model is based on conventional CNN architectures, which can restrict its ability to adapt to more complex or varied medical imaging tasks.

Jacob and Lal [77] introduced C19XNet, a multi-class model uses a deep CNN architecture that distinguishes classes. It introduces sophisticated preprocessing methods and data augmentation plans to strengthen models. The model was tested on a comprehensive dataset, with encouraging classification performance. However, the research did not dwell much on issues of class imbalance, which influence model performance in the field.

Roy et al. [78] created a new pooling-based VGG-Lite model to identify COVID-19 in unbalanced CXR data. The model proposes a lightweight architecture based on VGG-16 and MobileNet-V2, which is enhanced with an Edge Enhanced Module (EEM) and a novel 2Max-Min pooling layer. These innovations focus on prioritizing edge features and spatial attention to enhance detection accuracy. Tests on several datasets showed lower performance compared to current models. Nevertheless, the model depends on architectural decisions can restrict its applicability to other imaging modalities.

Alotaibi et al. [79] targeted automated diagnosis of COVID-19 through CXR image processing with a CNN. The research employed a modified ResNet-50 model, which was initially trained, fine-tuned to classify COVID-19, normal, and pneumonia. The model was highly accurate and validated using publicly available CXR datasets. Although effective, the reliance of the approach on one CNN architecture can constrain its applicability to other diagnostic tasks.

Singh et al. [80] proposed Deep CP-CXR, an AI-based model. The model uses a CNN architecture that is trained to extract features on CXR images. It was tested on a COVID-19- and pneumonia-labeled CXR image dataset. The framework exhibited efficient classification features. Nevertheless, the research lacked comprehensive

information on the model performance in various demographics, which was critical in clinical practice.

Fu et al. [81] introduced LungMaxViT, an explainable hybrid transformer model to classify multi-class lung disease. The model combines a CNN block with a squeeze-and-excitation (SE) block in the first stage to promote feature recognition. It uses a transformer architecture to learn global dependencies and employs attention mechanisms to offer interpretability. It was shown to perform competitively in separating different lung diseases. Nevertheless, its complexity can result in greater computational requirements, which can restrict its use in resource-intensive environments.

A hybrid architecture was proposed by Amina, et al. [82] that integrates Vision Transformers (ViT) and metaheuristic optimization methods to detect and classify COVID-19 severity based on multimodal imaging data. The framework combines the GWO to optimize hyperparameters and Particle Swarm Optimization (PSO) to select features, using the self-attention mechanism of ViT to extract features at both global and local scales. This method was tested on CXR and CT scan data with promising results. However, the use of metaheuristic optimizers can lead to higher training time and computational cost.

Pal et al. [83] performed a comparative study of multiclass classification models to detect pneumonia. The researchers tested several AI algorithms, such as Support Vector Machine (SVM), random forests, and CNN, on different datasets. The results emphasized the trade-offs between model complexity and the accuracy of classification. Nevertheless, the research failed to extensively consider the issues of class imbalance, which have impacted the performance of the models in modern settings.

Wang et al. [84] introduced TMscNet, a model that integrates various information interactions to classify COVID-19 CXRs. The architecture incorporates feature fusion methods to merge information across multiple layers and modalities to improve the capacity of the model. Nonetheless, the research lacked specifics regarding the interpretability of the model, which is essential in clinical practice.

Ameta et al. [85] developed an SVM-based and DenseNet-121-based automated CXR image classification system to detect COVID-19. This system uses DenseNet-121 to extract features and SVM to classify them, with the objective of obtaining high accuracy with a simplified architecture. Nevertheless, the research did not comment on the generalizability or its resilience to changes in image quality.

Islam [86] introduced a genetic optimization-based method to improve the performance of deep CNNs in low-cost disease diagnosis using CXR images. The process consisted of using a Genetic Algorithm (GA) to optimize the tuning and freezing of layers in a pre-trained VGG16 model, with the goal of enhancing feature extraction and the accuracy of classification. Nevertheless, GA optimization was computationally more complex and require more time to train.

Efficient-VGG16 is an ensemble model that combines EfficientNet-B0 and VGG16 networks to classify COVID-19 CXR images, proposed by Kumar and Kumar [87]. The ensemble model takes advantage of both architectures to improve feature extraction and classification accuracy. The method showed competitive performance with traditional ML and transfer learning approaches. Nevertheless, ensemble nature of the model can translate to greater computational demands and complexity.

Pranay and M. R. [88] created an automated COVID-19 detection model based on the InceptionV3 algorithm and compared its performance with the ShuffleNet algorithm. The paper concentrated on accuracy improvement by refining the InceptionV3 model and comparing its performance with ShuffleNet. The findings revealed better accuracy when using the InceptionV3 model. Nevertheless, the research did not comment at length on the computational efficiency, which is essential in real-time applications.

Balasamy and Seethalakshmi [89] introduced HCO-RLF, a hybrid classification optimization algorithm that integrates recursive learning with fuzzy logic. The methodology was designed to improve detection precision by incorporating recurrent learning and fuzzy logic systems. The method showed better detection measures. Nonetheless, the hybrid model was complex, which was challenging to implement and scale.

Kordnoori et al. [90] introduced a DL-based model to classify COVID-19 accurately on CT-scan images. The framework used a CNN model that was trained to detect COVID-19 on CT images. The analysis showed good classification properties. Nevertheless, the research lacked comprehensive information on the model performance in various demographics, which was critical in clinical practice.

The hybrid DL architecture FINE_DENSEIGANET was proposed by Sahu and Kashyap [91] and is used to classify medical images in chest CT scans. The model combines a DenseNet design with a Generative Adversarial Network (GAN) to improve feature extraction and classification precision. It was not shown to outperform traditional methods. Nonetheless, the hybrid model is more complex, which can potentially impose greater computational demands, restricting its use in resource-constrained environments.

Alharbi and Ahmad [92] presented the DI-QL model to optimize COVID-19 detection based on CT. The approach uses a DL framework with a quantum-inspired learning algorithm to enhance classification performance. The method was tested on a CT scan dataset, with promising results. However, the dependence on quantum-inspired algorithms was problematic in terms of implementation and scalability.

Pham et al. [94] utilized deep transfer learning and XAI to diagnose chest. The analysis used pre-trained DL fine-tuned on a CT scan dataset, with XAI methods applied to understand model predictions. The method was characterized by high diagnostic accuracy and interpretability. Nonetheless, the dependence on pre-trained models can restrict the flexibility to datasets.

Antunes et al. [95] proposed CTCOVID19, a DLCNN-based automatic COVID-19 detector on CT scans. The method was tested on a CT scan dataset, where it performed satisfactorily. However, the paper has not addressed the issue of class imbalance extensively, which influence model performance in practice.

Kordnoori et al. [96] introduced LungXpertAI, a deep multi-task learning framework that analyzes chest CT. This model incorporates Conditional Random Fields (CRF) to improve segmentation accuracy and classification. LungXpertAI showed better diagnostic performance in various tasks, such as lesion segmentation and disease

classification. Nonetheless, the multi-tasking was more complex, and it impose greater computational loads, which limit the feasibility of real-time applications.

FusionLungNet [97] is a multi-scale fusion convolution and refinement network to segment lung CT images. It uses a multi-level architecture that integrates a ResNet-50 encoder, Channel-wise Aggregation Attention (CAA) module, Multi-scale Feature Fusion (MFF) block, self-refinement (SR) module, and several decoders to improve the precision of segmentation. FusionLungNet scored IoU (IoU) at 98.04, which is better than current methods. The model has high performance, but its complexity was a challenge in terms of implementation and scalability.

Padmavathi and Ganesan [98] introduced a hybrid system that combines ViT and metaheuristic optimization algorithms to detect the severity of COVID-19. The framework uses the GWO to optimize hyperparameters and the PSO to select features, utilizing the self-attention mechanism of ViT to obtain global and local image features. The method showed better classification accuracy. But the dependency on metaheuristic optimization methods can also add complexity and time to the computations.

Suseela and Parekh [99] designed an attention-based CNN model to diagnose disease. The model includes a tailored bottleneck residual module to boost feature extraction. The attention mechanism enables the model to concentrate on the relevant areas in the CT images, enhancing diagnostic accuracy. Nevertheless, the performance of the model in various demographic groups was not widely discussed in the study, which was essential to clinical applicability.

Appati et al. [100] introduced a bootstrapped ViT-B/16 model to detect SARS in chest CT scan images. Although the study performed well, it lacked specific information on the interpretability of the model, which is essential to clinical decision-making.

Chowa et al. [101] developed a self-supervised learning privacy-preserving model. The model employed FL with Paillier homomorphic encryption to guarantee data privacy throughout training. It used two publicly available lung CT scan datasets, one labeled and the other not, with the latter divided into three subsets based on the data of different hospitals. The framework was designed to reduce the scale of data

annotation without compromising classification accuracy. Nonetheless, the challenge of applying FL to homomorphic encryption can add additional computational costs, which can potentially reduce scalability in practical scenarios.

Tan and Arif [102] proposed a multiclass classification model to detect COVID-19 in CT scan images using the VGG-16 architecture with transfer learning. Nevertheless, the study did not critically assess the performance of the model in various demographic groups, which was essential to clinical applicability.

Singh et al. [103] suggested a fine-tuned InceptionV3 model to detect cancer CT scans of the chest with high accuracy. The model used transfer learning methods, with pre-trained InceptionV3 weights and fine-tuning them on a multi-class CT scan dataset. The methodology sought to enhance diagnostic accuracy through the deep feature extraction of the InceptionV3 model. Nevertheless, the research failed to extensively consider the issues of class imbalance, which have impacted the performance of the models in real-life settings.

Güngor [104] performed a comparative analysis of wavelet denoising methods on high-noise CT images of COVID-19 patients. The results revealed that some wavelet functions were useful in minimizing noise, thus enhancing the quality of COVID-19 diagnosis CT images. Nonetheless, the study did not critically assess how denoising affects downstream activities like disease classification.

Newson et al. [105] used an encoder-decoder CNN model to perform simple CT segmentation of lungs with COVID-19 infections. The goal of the approach was to deliver a simple and repeatable solution to lung segmentation on COVID-19 CT scans. Nevertheless, the model was not widely tested on various CT scan datasets, which influence its generalizability.

Prinzi et al. [106] examined how wavelet kernels affect the predictive power of radiomic features in COVID-19 CXR images. The analysis contrasted various wavelet kernels and assessed their influence on the predictive ability of radiomic models. The results indicated that some wavelet kernels improve the predictive power of radiomic features in COVID-19 prognosis. Nevertheless, the research did not comprehensively test the clinical relevance of the radiomic models in the real world.

Syafira et al. [107] investigated the clustering of CXR images through convolutional autoencoders to detect lung diseases. The study sought to identify the efficacy of clustering algorithms based on an autoencoder model in the grouping of CXR image outcomes. The dataset used in the study involved 700 CXR images of the chest (500 with disease and 200 with normal CXR). The results revealed that clustering techniques help in medical analysis, including disease detection and tracking of the most recent disease progressions. Nonetheless, the scalability of the clustering approaches to large datasets was not widely assessed in the study.

2.5 Research Gaps

Research gaps identified from the survey are as follows:

- Most existing studies focused on either CT or CXR datasets individually for medical image enhancement and disease detection. There is a clear lack of research that integrates both modalities within a unified framework to leverage their complementary diagnostic strengths. Such combined analyses improve model robustness and generalization across imaging types.
- While several studies employed U-Net or its variants for segmentation and enhancement tasks, very few explored the optimization of Attention U-Net parameters. Moreover, the integration of these networks with hybrid preprocessing methods such as CLAHE, bilateral filtering, or gamma correction remains underdeveloped. This limits the precision of segmentation and the overall diagnostic accuracy.
- No existing work addressed a full-scale methodology that jointly utilizes CT and CXR datasets with advanced preprocessing, optimized segmentation, transfer learning-based feature extraction, and optimal feature selection followed by efficient classification. This gap highlights the need for an end-to-end framework that combines all these stages to achieve high diagnostic accuracy, reduced noise, and enhanced interpretability in medical imaging.

2.6 Summary

The analysed literature highlighted the increasing use of AI and DL in improving the quality of medical imaging, especially CT and CXR scans. To enhance diagnostic clarity and minimize radiation exposure, researchers examined different denoising and enhancement strategies, including CNN-based models, U-Net variants, CLAHE, and transfer learning. Nevertheless, even with the achievements, most works were concentrated on single-modality datasets and did not involve thorough optimization of the preprocessing, segmentation, and classification steps. Lastly, the survey identified promising developments but also emphasized the necessity of unified, optimized, and multi-modal frameworks to achieve more reliable medical image analysis.

Chapter 3

Preprocessing of COVID-19 Images

3.1 Introduction

Preprocessing in medical imaging plays a crucial role in improving the visual quality and diagnostic reliability of CT and CXR images. It involves a series of enhancement, normalization, and noise suppression techniques applied before segmentation or classification to ensure optimal feature extraction. These methods help radiologists and automated systems to analyze subtle details that are otherwise obscured by noise or low contrast in raw medical scans.

Despite their effectiveness, existing preprocessing methods exhibit several drawbacks. Traditional filters like Gaussian and median often blur fine details and edges, leading to the loss of diagnostically important information. Techniques such as bilateral filtering and CLAHE enhance local contrast but tend to amplify unwanted artifacts or uneven illumination in complex imaging conditions. Moreover, many methods lack adaptability to varying noise levels and imaging modalities, resulting in inconsistent performance across CT and CXR images. These limitations hinder their capability to preserve crucial structural information while maintaining high noise suppression efficiency.

Among advanced denoising techniques, the BM3D filtering algorithm has shown significant advantages over conventional preprocessing methods. BM3D effectively separates noise from structural details by grouping similar image patches into 3D blocks in a transformed domain. This approach enables superior noise suppression while preserving edges, textures, and fine anatomical features essential for diagnosis. Additionally, BM3D demonstrates excellent adaptability across different noise intensities and imaging modalities, making it one of the most robust and reliable preprocessing techniques for medical image enhancement in modern diagnostic applications.

3.2 BM3D Preprocessing

Unlike basic filters that often blur important edges and fine details, BM3D utilizes a combination of block matching. Its unique approach of grouping similar patches across the image and applying joint filtering in a high-dimensional domain enhances sparsity, leading to superior denoising performance without sacrificing image quality. This results in clearer, more reliable medical images, essential for accurate diagnosis, especially when dealing with complex patterns in COVID-19-affected lung regions.

Figure 3.1 shows the proposed BM3D Denoising flowchart. Initially. The process begins by inputting either a CT or CXR image, which typically contains noise due to acquisition or transmission limitations, particularly in medical imaging. The input image undergoes normalization to scale pixel intensity values within a standard range, often [0, 1] or [0, 255], to ensure uniformity. Additionally, resizing performed to maintain consistent dimensions across the dataset, which improves the efficiency of further processing steps. Let $\mathrm{I}_{input}(\mathrm{x},\mathrm{y})$ be the original image and $\mathrm{I}_{norm}(\mathrm{x},\mathrm{y})$ is normalized image:

$$I_{input}(x,y) = \frac{I_{input}(x,y) - I_{min}}{I_{max} - I_{min}} \tag{3.1}$$

The normalized image is divided into small overlapping patches (blocks), and similar patches across the image are identified using a similarity metric (e.g., Euclidean distance). These similar patches are grouped into a 3D array for joint processing, which increases the redundancy essential for effective denoising. Mathematically, for a reference patch P_r and candidate patch P_c:

$$D(P_r, P_c) = \sqrt{\sum_{i=1}^{N} \big(P_r(i) - P_c(i)\big)^2} \tag{3.2}$$

Here, D is the distance metric, and patches satisfying $D < \tau$ are grouped together. The grouped similar patches are transformed into a sparse domain using a combination of a 2D Discrete Cosine Transform (DCT) for spatial decorrelation within each patch and a 1D transform along the grouped dimension. This enhances sparsity, making it easier to distinguish noise from actual image content. For a patch $P(x, y)$, the 2D DCT is:

$$C(u,v) = \sum_{x=0}^{N-1} \sum_{y=0}^{N-1} P(x,y).\cos\left(\frac{\pi(2x+1)u}{2N}\right) cos\left(\frac{\pi(2y+1)v}{2N}\right) \quad (3.3)$$

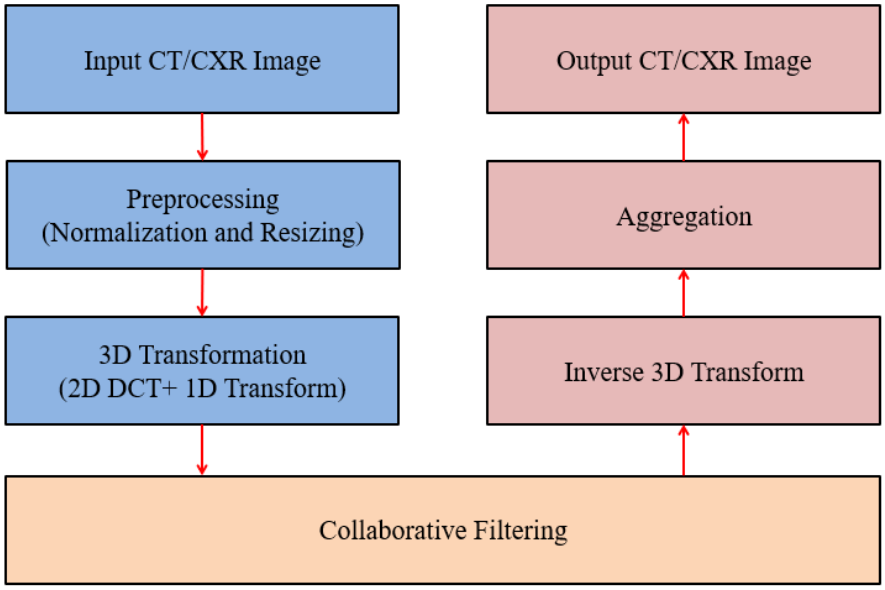

Figure 3.1. Proposed BM3D Denoising Flowchart.

In the transformed domain, collaborative filtering is applied to suppress noise. Two filtering methods are commonly used such as hard threshold-based wiener Filtering. A statistical approach that weights the coefficients based on estimated signal and noise variances.

$$C'(u,v) = \begin{cases} C(u,v), if\ |C(u,v)| \geq T \\ 0,\ otherwise \end{cases} \quad (3.4)$$

Here, T is the hard threshold value, $C'(u,v)$ is the filtered outcome. The filtered patches are transformed back to the spatial domain using inverse 2D DCT and inverse 1D transform, reconstructing each patch in its denoised form. The inverse DCT:

$$P'(x,y) = \frac{1}{N}\sum_{u=0}^{N-1} \sum_{v=0}^{N-1} C'(u,v).\cos\left(\frac{\pi(2x+1)u}{2N}\right) cos\left(\frac{\pi(2y+1)v}{2N}\right) \quad (3.5)$$

Finally, overlapping denoised patches are aggregated by averaging to produce the final denoised image. This overlapping mechanism enhances reconstruction quality by reducing block artifacts. If multiple estimates $P'(x,y)$ overlap at a pixel location, the aggregated output is:

$$I_{denoised}(x,y) = \frac{\sum_{i=1}^{M} w_i . P'(x,y)}{\sum_{i=1}^{M} w_i} \quad (3.6)$$

Here, w_i are weights based on the confidence of each patch estimate. The final denoised image $I_{denoised}(x,y)$ is produced, significantly reducing noise while preserving critical diagnostic details, making it suitable for precise medical analysis in the subsequent steps of the proposed methodology.

3.2.1 3D Transformation

The 3D transformation stage as shown in Figure 3.2 provides a powerful mechanism for separating noise and structural information in medical images such as CT and CXR scans. By combining 2D DCT applied spatially within each patch and a one-dimensional (1D) transform applied across similar patches, this method effectively compacts signal energy while spreading noise uniformly across coefficients. This dual-domain operation enhances sparsity, allowing collaborative filtering to more easily identify and suppress noise components without degrading fine anatomical structures. As a result, the 3D transformation offers superior edge preservation, improved contrast, and enhanced robustness across varying noise levels and imaging modalities, making it particularly effective for diagnostic imaging enhancement.

Patch Extraction: Each patch $P_i(x,y)$is extracted from the image $I(x,y)$, where (i_x, i_y)denotes the position of the patch. This step identifies small overlapping regions for local analysis, ensuring redundancy for noise averaging during collaborative filtering.

$$P_i(x,y) = I(x + i_x, y + i_y) \quad (3.7)$$

Block Matching: Here, $S_i$represents the group of similar patches identified by comparing the Euclidean distance $\| P_i - P_j \|_2^2$between a reference patch $P_i$and neighboring patches P_j, with τas the similarity threshold. This forms the basis for 3D grouping.

$$S_i = \{P_j \mid \| P_i - P_j \|_2^2 < \tau\} \quad (3.8)$$

2D-DCT: The 2D DCT is applied to each patch $P(x,y)$of size $N \times N$, where $\alpha(u)$and $\alpha(v)$are normalization factors. It converts spatial domain information into

frequency domain coefficients, separating low-frequency (signal) and high-frequency (noise) components.

$$T_{2D}(u,v) = \alpha(u)\alpha(v) \sum_{x=0}^{N-1} \sum_{x=0}^{N-1} P(x,y) \cos\left[\frac{\pi(2x+1)u}{2N}\right] \cos\left[\frac{\pi(2y+1)v}{2N}\right] \quad (3.9)$$

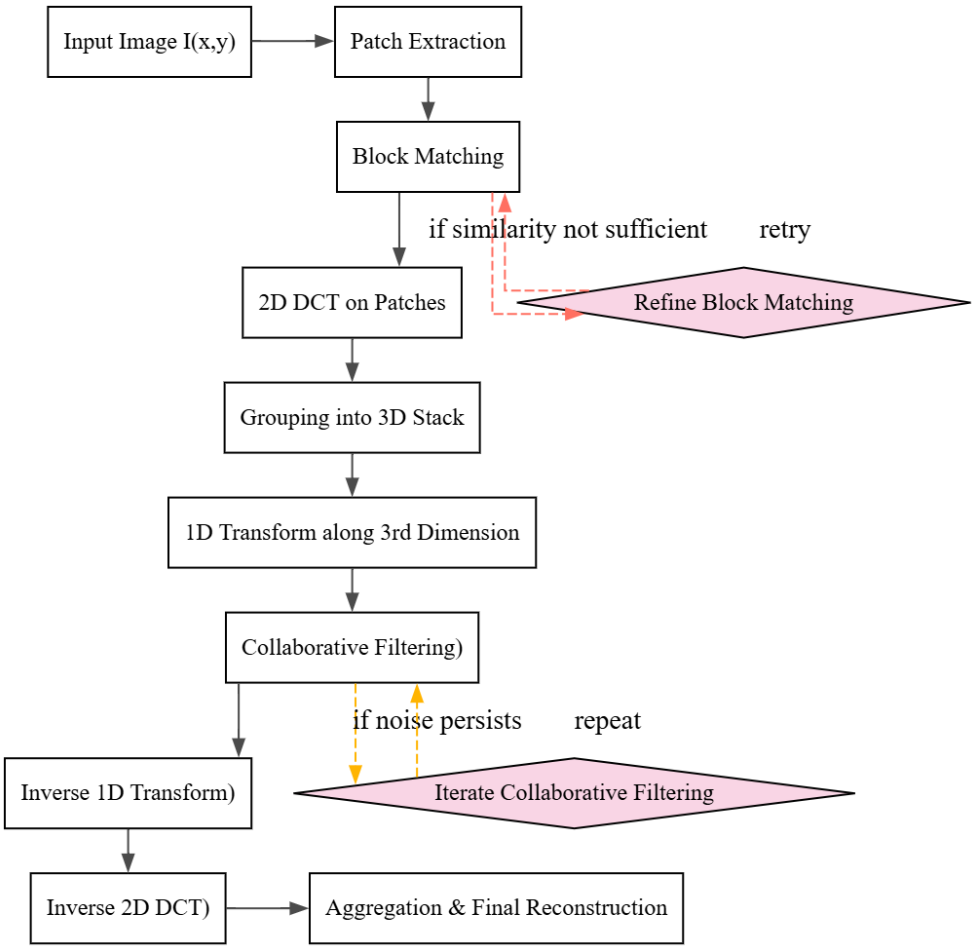

Figure 3.2. Flowchart of 3D Transformation.

Normalization Coefficient: The coefficient $\alpha(u)$ ensures orthogonality and energy preservation of the transform. It scales the frequency coefficients appropriately to maintain consistent amplitude distribution across all transform bases.

$$\alpha(u) = \begin{cases} \sqrt{\frac{1}{N}}, & \text{if } u = 0 \\ \sqrt{\frac{2}{N}}, & \text{if } u > 0 \end{cases} \quad (3.10)$$

Grouping into 3D Stack: The grouped patches form a 3D stack $G_i(u, v, k)$, where each layer corresponds to the transformed version of a similar patch. The dimension Kdenotes the number of patches in the group.

$$G_i(u, v, k) = \{T_{2D}^k(u, v) \mid k = 1,2, \ldots, K\} \quad (3.11)$$

1D Transformation Along the Third Dimension: A 1D transform, typically Haar or DCT, is applied along the third dimension (across similar patches). Here, $\phi_l(k)$denotes the 1D transform basis. This operation enhances sparsity by aligning similar structures and spreading random noise uniformly.

$$T_{3D}(u, v, l) = \sum_{k=0}^{K-1} G_i(u, v, k)\phi_l(k) \quad (3.12)$$

Collaborative Filtering: Collaborative filtering applies a shrinkage or threshold function $H(u, v, l)$to the transformed coefficients $T_{3D}(u, v, l)$.

$$\hat{T}_{3D}(u, v, l) = T_{3D}(u, v, l) \cdot H(u, v, l) \quad (3.13)$$

Inverse 1D Transformation: The inverse 1D transform reconstructs the filtered group $\hat{G}_i$from the thresholded coefficients, ensuring minimal distortion of the original signal. This step restores the third-dimensional data structure after noise suppression.

$$\hat{G}_i(u, v, k) = \sum_{l=0}^{K-1} \hat{T}_{3D}(u, v, l)\phi_l(k) \quad (3.14)$$

Inverse 2D DCT: The inverse 2D DCT converts the filtered frequency coefficients back to the spatial domain, producing denoised image patches $\hat{P}(x, y)$that retain structural and textural integrity.

$$\hat{P}(x, y) = \sum_{u=0}^{N-1} \sum_{v=0}^{N-1} \alpha(u)\alpha(v)\hat{G}(u, v) \cos\left[\frac{\pi(2x+1)u}{2N}\right] \cos\left[\frac{\pi(2y+1)v}{2N}\right] \quad (3.15)$$

Aggregation and Final Reconstruction: The final denoised image $\hat{I}(x, y)$is reconstructed through weighted averaging of overlapping denoised patches $\hat{P}_i(x, y)$, where $w_i(x, y)$denotes aggregation weights. This ensures smooth transitions and reduces residual noise across patch boundaries.

$$\hat{I}(x, y) = \frac{\sum_i w_i(x,y)\hat{P}_i(x,y)}{\sum_i w_i(x,y)} \quad (3.16)$$

3.3 Results and Discussion

The results of the preprocessing stage demonstrate that the BM3D-based enhancement significantly outperformed traditional techniques like Gaussian filtering and median smoothing for both CT and CXR datasets.

3.3.1 Results on CT Dataset

Table 3.1 presents the optimized parameter settings for the BM3D filtering process, highlighting how noise suppression and anatomical structure preservation were effectively balanced. The noise standard deviation (σ) was tuned between 10 and 40, with an optimal value of 25, providing stable denoising without over-smoothing tissue textures. The 8×8 block size within a 39×39 search window allowed accurate patch matching while maintaining computational efficiency. A step size of 3 ensured smooth local continuity during patch aggregation. The 2D-DCT + 1D Haar Transform was selected as the best 3D transformation technique, yielding better texture restoration compared to pure DCT or wavelet methods. The thresholding factor was adaptively set to 2.7σ, providing a dynamic balance between residual noise removal and edge preservation. The Wiener filtering gain of 0.85 further refined denoising strength in the second stage. For aggregation, a Gaussian kernel weighting scheme was employed to emphasize central pixels and suppress boundary artifacts. Images were normalized within the 0–1 range, enhancing transform consistency across modalities.

Figure 3.3 illustrates the effect of BM3D denoising along with various data augmentation operations on CT images. The first set shows how noisy input images are rotated before and after BM3D denoising, highlighting that the noise-free image preserves structural clarity even after rotation. The second set demonstrates contrast enhancement, where images after BM3D denoising undergo contrast adjustment, producing sharper visual outputs. Similarly, the final set displays intensity adjustment applied to both noisy and denoised images, confirming that BM3D preprocessing provides a cleaner foundation, leading to clearer intensity variations. These examples collectively demonstrate that BM3D denoising improves image quality and ensures data augmentation operations produce meaningful and reliable outputs for subsequent processing stages.

Table 3.1. BM3D Filtering Parameters with Optimization Range and Best Settings.

Parameter	Minimum Value	Maximum Value	Best Value (Optimized)
Noise Standard Deviation (σ)	10	40	25
Block (Patch) Size	6 × 6	10 × 10	8 × 8
Search Window Size	25 × 25	45 × 45	39 × 39
Step Size Between Patches	2	6	3
Transform Type (3D)	DCT only	DCT + Wavelet	2D DCT + 1D Haar Transform
Thresholding Factor (Stage 1)	2.0σ	3.5σ	2.7σ (Adaptive)
Wiener Filtering Gain (Stage 2)	0.6	1.0	0.85
Aggregation Weighting Function	Uniform	Gaussian	Gaussian Kernel Weighting
Intensity Normalization Range	0–255	0–1 (normalized)	0–1 normalized

Figure 3.4 demonstrates the effect of BM3D denoising combined with multiple augmentation techniques applied to CT images. The first column shows noisy input images, followed by their scaled output, where size adjustments are clearly visible with improved clarity after noise removal. The second set of images illustrates how BM3D-denoised outputs undergo scaling, ensuring that even after resizing, structural details remain sharp and noise-free. Similarly, motion blur adjustments are applied to both noisy and denoised images, confirming that BM3D preprocessing significantly

improves visual consistency even under simulated distortions. The final set highlights sharpening operations on noisy and denoised images, demonstrating that BM3D provides a cleaner base image, enhancing the effectiveness of sharpening, thereby preserving fine lung structures.

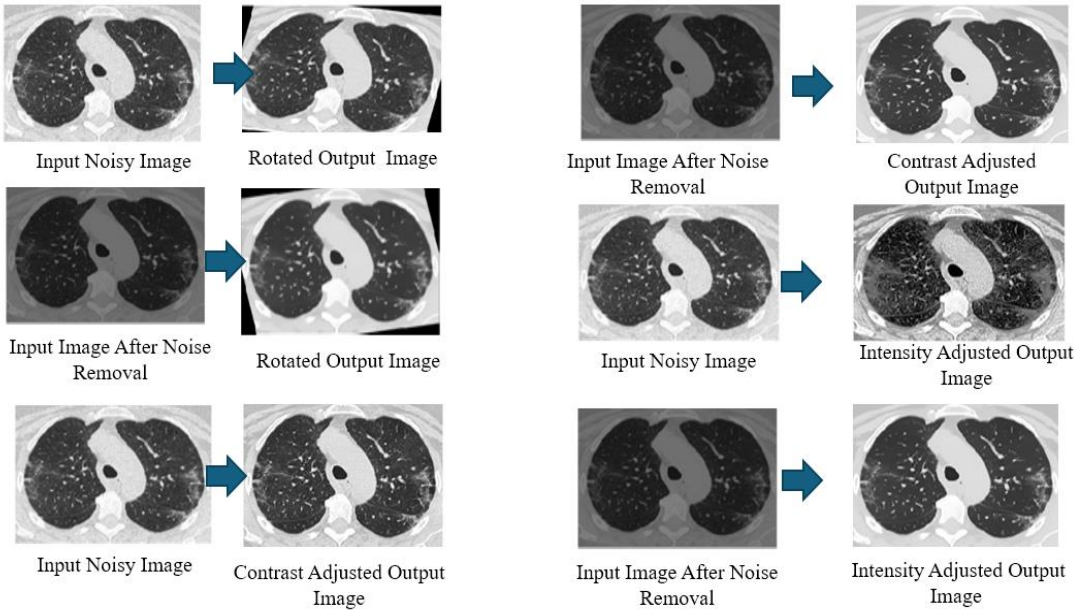

Figure 3.3. BM3D Denoising Results with Data Augmentation Techniques.

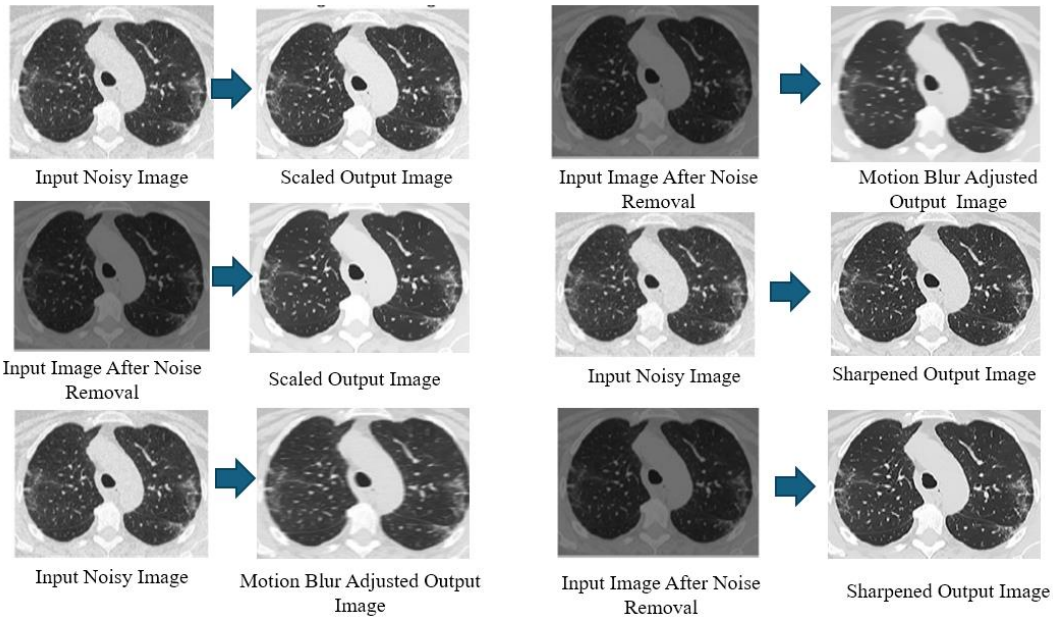

Figure 3.4. BM3D Denoising Impact with Various Augmentation Techniques on CT Images.

Table 3.2 presents the PSNR performance analysis for both COVID-19 and non-COVID-19 images using Wavelet Thresholding (WT) [104] and BM3D algorithms under different preprocessing techniques. For COVID-19 images, the BM3D algorithm consistently provided higher PSNR values, indicating superior image quality, with 61.86487 for rotation, 76.26048 for scaling, 82.28839 for contrast adjustment, 82.28839 for intensity adjustment, 74.28114 for motion blur, 79.46884 for sharpening, and 82.28839 for flipping.

In comparison, WT [104] produced lower PSNR values with 55.60968 for rotation, 57.04691 for scaling, 51.05974 for contrast adjustment, 51.05966 for intensity adjustment, 57.04691 for motion blur, 57.04691 for sharpening, and 56.0276 for flipping. Similarly, for non-COVID-19 images, BM3D outperformed WT [104] across all methods, achieving 61.51998 for rotation, 78.69673 for scaling, 84.90672 for both contrast and intensity adjustment, 78.81164 for motion blur, 83.65212 for sharpening, and 84.90672 for flipping.

Table 3.2. PSNR Performance Analysis on CT Dataset.

Preprocessing Method	COVID-19		Non-COVID-19	
	WT [104]	BM3D	WT [104]	BM3D
Rotation	55.60968	61.86487	56.87786	61.51998
Scaling	57.04691	76.26048	58.84652	78.69673
Contrast Adjustment	51.05974	82.28839	52.85734	84.90672
Intensity Adjustment	51.05966	82.28839	52.85687	84.90672
Motion Blur	57.04691	74.28114	58.84652	78.81164
Sharpening	57.04691	79.46884	58.84652	83.65212
Flipping	56.0276	82.28839	57.84639	84.90672

In contrast, WT [104] resulted in comparatively lower PSNR values of 56.87786 for rotation, 58.84652 for scaling, 52.85734 for contrast adjustment, 52.85687 for

intensity adjustment, 58.84652 for motion blur, 58.84652 for sharpening, and 57.84639 for flipping. The results clearly demonstrate the superior denoising and quality preservation capability of the BM3D algorithm.

Table 3.3 presents the SSIM performance analysis for both COVID-19 and non-COVID-19 cases under different preprocessing methods. The BM3D algorithm consistently achieved superior SSIM values compared to the Wavelet Thresholding method [41]. For COVID-19 images, the BM3D algorithm recorded 0.745489 for rotation, 0.843516 for scaling, 0.840268 for both contrast and intensity adjustment, 0.696439 for motion blur, 0.919483 for sharpening, and 0.840268 for flipping. In contrast, WT [104] resulted in lower SSIM values, with 0.232125 for rotation, 0.564695 for scaling, 0.000159 for contrast adjustment, 0.000155 for intensity adjustment, 0.564695 for motion blur, 0.564695 for sharpening, and 0.224782 for flipping.

Table 3.3. SSIM Performance Analysis on CT Dataset.

Preprocessing Method	COVID-19		Non-COVID-19	
	WT [104]	BM3D	WT [104]	BM3D
Rotation	0.232125	0.745489	0.400267	0.839128
Scaling	0.564695	0.843516	0.693541	0.909002
Contrast Adjustment	0.000159	0.840268	0.000569	0.909821
Intensity Adjustment	0.000155	0.840268	0.000564	0.909821
Motion Blur	0.564695	0.696439	0.693541	0.855923
Sharpening	0.564695	0.919483	0.693541	0.926469
Flipping	0.224782	0.840268	0.396578	0.909821

Similarly, for Non-COVID-19 images, BM3D achieved SSIM values of 0.839128 for rotation, 0.909002 for scaling, 0.909821 for both contrast and intensity adjustment, 0.855923 for motion blur, 0.926469 for sharpening, and 0.909821 for flipping, while

WT [104] produced 0.400267 for rotation, 0.693541 for scaling, 0.000569 for contrast adjustment, 0.000564 for intensity adjustment, 0.693541 for motion blur, 0.693541 for sharpening, and 0.396578 for flipping.

Table 3.4 shows the MSE performance where lower values indicate better image quality. The BM3D algorithm consistently achieved the lowest MSE across all preprocessing methods. For COVID-19 cases, BM3D yielded 0.042325 for rotation, 0.001538 for scaling, 0.000384 for both contrast and intensity adjustment, 0.002426 for motion blur, 0.000735 for sharpening, and 0.000384 for flipping, significantly outperforming WT [104], which recorded 0.178695 for rotation, 0.128348 for scaling, 0.509455 for contrast adjustment, 0.509464 for intensity adjustment, 0.128348 for motion blur, 0.128348 for sharpening, and 0.162301 for flipping.

Table 3.4. MSE Performance Analysis on CT Dataset.

Preprocessing Method	COVID-19		Non-COVID-19	
	WT [104]	BM3D	WT [104]	BM3D
Rotation	0.178695	0.042325	0.133443	0.045823
Scaling	0.128348	0.001538	0.084806	0.000878
Contrast Adjustment	0.509455	0.000384	0.33678	0.00021
Intensity Adjustment	0.509464	0.000384	0.336817	0.00021
Motion Blur	0.128348	0.002426	0.084806	0.000855
Sharpening	0.128348	0.000735	0.084806	0.00028
Flipping	0.162301	0.000384	0.106768	0.00021

Similarly, for Non-COVID-19 cases, BM3D achieved 0.045823 for rotation, 0.000878 for scaling, 0.00021 for both contrast and intensity adjustment, 0.000855 for motion blur, 0.00028 for sharpening, and 0.00021 for flipping, while WT [104] recorded higher errors with 0.133443 for rotation, 0.084806 for scaling, 0.33678 for contrast adjustment, 0.336817 for intensity adjustment, 0.084806 for motion blur, 0.084806

for sharpening, and 0.106768 for flipping. These results clearly indicate that the BM3D algorithm provides significantly improved image quality compared to WT [104] under all preprocessing conditions.

3.3.2 Results on CXR Dataset

Figure 3.5 showcases the impact of different image preprocessing techniques (Intensity, Motion Blur, Sharpened, Flipping) applied to a COVID-19 CXR image, comparing the results of Existing Wavelet Thresholding against a Proposed BM3D method. The various transformations demonstrate how image characteristics are altered, with the aim of improving clarity or generating diverse training data while highlighting the potential differences in output quality between the existing and proposed preprocessing approaches.

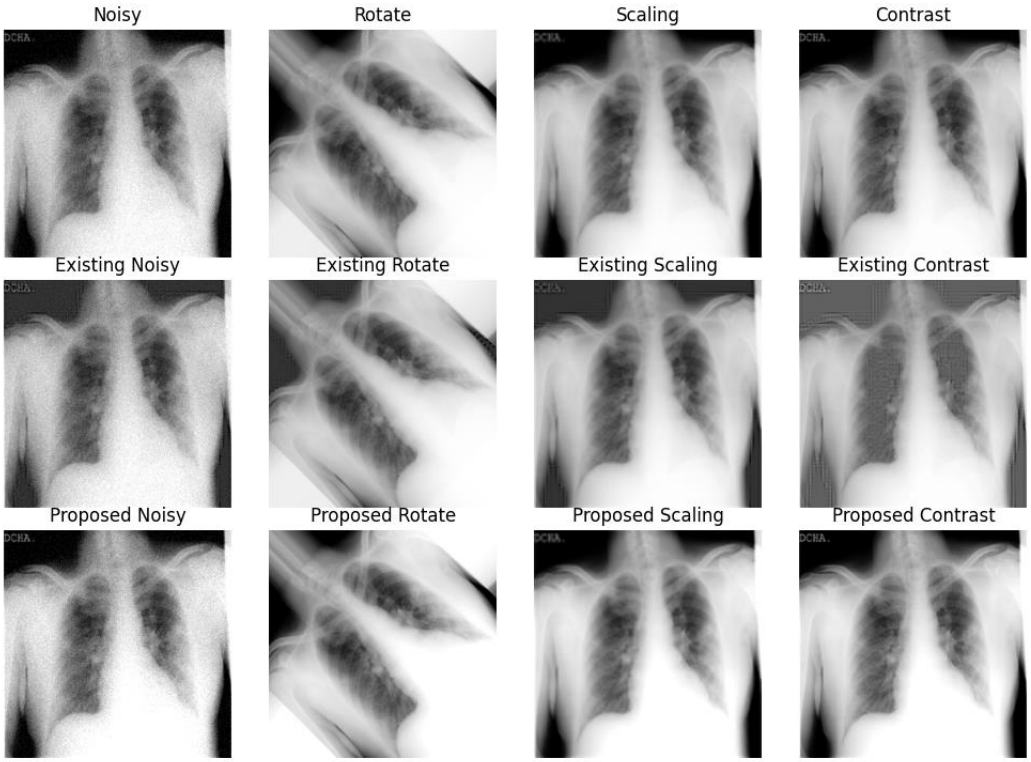

Figure 3.5. Preprocessing Results of Existing Wavelet Thresholding and Proposed BM3D on COVID-19 Set.

Figure 3.6 illustrates the application of various image preprocessing techniques (Noisy, Rotate, Scaling, Contrast) to a Non-COVID-19 CXR image, comparing the outcomes of Existing Wavelet Thresholding with a Proposed BM3D method. This

comparison helps in evaluating how each preprocessing technique affects the visual quality and characteristics of normal lung images, and how the proposed method potentially offers superior or different results compared to the existing approach for non-COVID-19 cases.

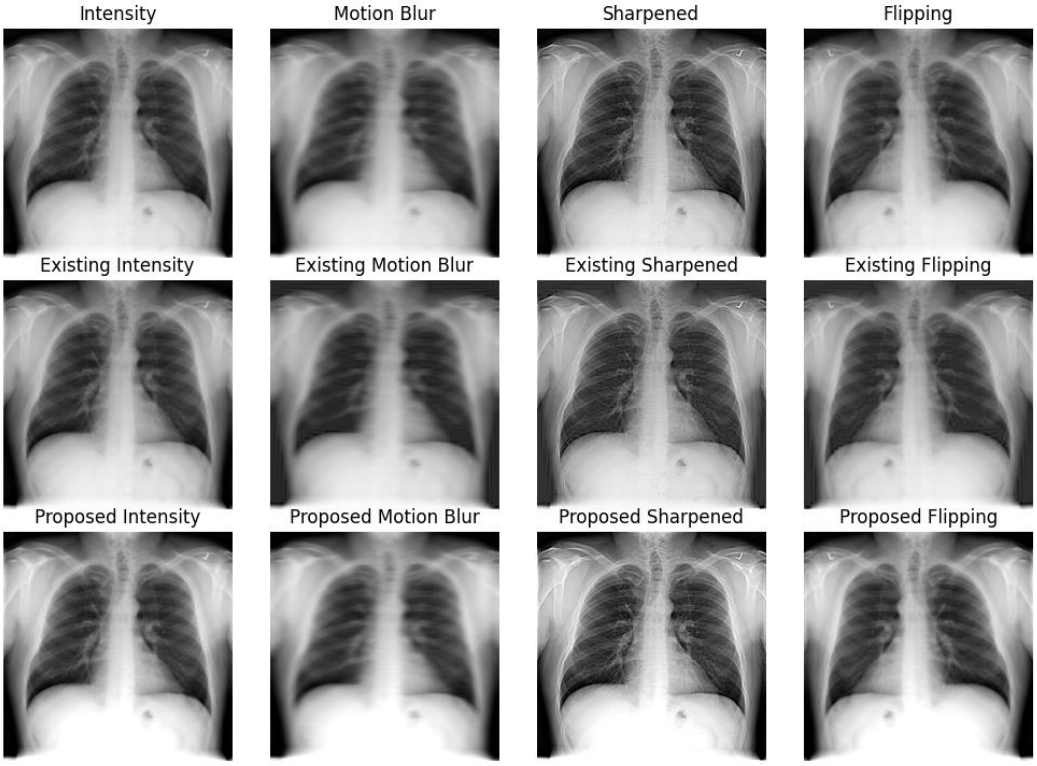

Figure 3.6. Preprocessing Results of Existing Wavelet Thresholding and Proposed BM3D on non-COVID-19 Set.

Table 3.5 presents the PSNR Performance Analysis on the CXR dataset for both non-COVID-19 and COVID-19 images under various preprocessing attacks, comparing WT [106] and BM3D methods. For Non-COVID-19 images, the BM3D approach consistently outperforms WT [106], achieving PSNR values of 66.57214 dB for noisy images, 59.08357 dB for rotation, 66.23095 dB for scaling, 66.26108 dB for contrast adjustment, 66.26106 dB for intensity adjustment, 66.18853 dB for motion blur, 66.65802 dB for sharpening, and 62.20782 dB for flipping, whereas WT [106] produced lower PSNR values ranging from 57.37731 dB to 57.82889 dB across these attacks.

Similarly, for COVID-19 images, BM3D consistently yielded better PSNR results with 66.21806 dB for noisy images, 60.91104 dB for rotation, 65.57614 dB for scaling, 65.74749 dB for contrast, 65.74746 dB for intensity, 65.57866 dB for motion blur, 65.79001 dB for sharpening, and 63.60607 dB for flipping, outperforming WT [106], which recorded values between 55.89617 dB to 56.33684 dB across all scenarios. These results confirm BM3D's superior noise reduction and image quality preservation for CXR images.

Table 3.5. PSNR Performance Analysis on CXR Dataset.

Attack	Non-COVID19		COVID-19	
	WT [106]	BM3D	WT [106]	BM3D
Noisy	57.81469	66.57214	56.33258	66.21806
Rotate	57.65243	59.08357	56.31151	60.91104
Scaling	57.8176	66.23095	56.33713	65.57614
Contrast	57.37731	66.26108	55.89617	65.74749
Intensity	57.67367	66.26106	56.20889	65.74746
Motion Blur	57.80722	66.18853	56.33586	65.57866
Sharpened	57.82889	66.65802	56.33684	65.79001
Flipping	57.75999	62.20782	56.3217	63.60607

Table 3.6 provides the SSIM performance analysis on the CXR dataset for non-COVID-19 and COVID-19 images under different preprocessing attacks using WT [106] and BM3D techniques. For non-COVID-19 images, BM3D consistently delivers higher structural similarity, achieving SSIM values of 0.497122 for noisy images, 0.278917 for rotation, 0.915584 for scaling, 0.926807 for contrast adjustment, 0.926805 for intensity adjustment, 0.854739 for motion blur, 0.807974 for sharpening, and 0.392716 for flipping.

In contrast, WT [106] produces significantly lower SSIM scores, ranging between 0.215127 and 0.267802. Similarly, for COVID-19 images, BM3D outperforms WT [106] across all scenarios, with SSIM values of 0.249087 for noisy images, 0.445325 for rotation, 0.747633 for scaling, 0.747307 for contrast adjustment, 0.747305 for intensity adjustment, 0.743735 for motion blur, 0.557568 for sharpening, and 0.461381 for flipping. Meanwhile, WT [106] shows inferior SSIM results between 0.015612 and 0.099669. These outcomes demonstrate that BM3D substantially enhances image quality and structural similarity, making it more reliable under varied conditions.

Table 3.6. SSIM Performance Analysis on CXR Dataset.

Attack	Non-COVID19		COVID-19	
	WT [106]	BM3D	WT [106]	BM3D
Noisy	0.262801	0.497122	0.091431	0.249087
Rotate	0.215127	0.278917	0.099669	0.445325
Scaling	0.264218	0.915584	0.093201	0.747633
Contrast	0.230295	0.926807	0.015612	0.747307
Intensity	0.261089	0.926805	0.08236	0.747305
Motion Blur	0.262994	0.854739	0.09222	0.743735
Sharpened	0.267802	0.807974	0.095065	0.557568
Flipping	0.251944	0.392716	0.093258	0.461381

Table 3.7 presents the MSE performance analysis on the CXR dataset for both non-COVID-19 and COVID-19 images, comparing Wavelet Thresholding and BM3D techniques under various attack conditions. For non-COVID-19 images, BM3D significantly reduces the error across all scenarios, with MSE values of 1.431747 for noisy images, 8.030138 for rotation, 1.548766 for scaling, 1.538056 for contrast

adjustment, 1.538066 for intensity adjustment, 1.563967 for motion blur, 1.403715 for sharpening, and 3.911097 for flipping.

In contrast, Wavelet Thresholding results in much higher MSE values ranging from 10.71991 to 11.8946. Similarly, for COVID-19 images, BM3D demonstrates superior performance, with MSE values of 1.55337 for noisy images, 5.272009 for rotation, 1.800803 for scaling, 1.731137 for contrast adjustment, 1.731148 for intensity adjustment, 1.79976 for motion blur, 1.714271 for sharpening, and 2.834481 for flipping. Meanwhile, Wavelet Thresholding yields higher MSE values between 15.11359 and 16.72875, indicating greater reconstruction errors. These results confirm that BM3D offers more effective noise suppression and preserves image quality better than Wavelet Thresholding under diverse conditions.

Table 3.7. MSE Performance Analysis on CXR Dataset.

Attack	Non-COVID19		COVID-19	
	WT [104]	BM3D	WT [104]	BM3D
Noisy	10.75501	1.431747	15.12941	1.55337
Rotate	11.16444	8.030138	15.20299	5.272009
Scaling	10.74781	1.548766	15.11359	1.800803
Contrast	11.8946	1.538056	16.72875	1.731137
Intensity	11.10997	1.538066	15.56651	1.731148
Motion Blur	10.77353	1.563967	15.11802	1.79976
Sharpened	10.71991	1.403715	15.11459	1.714271
Flipping	10.89133	3.911097	15.16738	2.834481

3.4 Summary

The BM3D preprocessing applied to CT and CXR datasets demonstrates a highly effective denoising capability while preserving critical anatomical details, such as edges, textures, and fine structural features. By leveraging the combined 2D spatial and 1D inter-patch transformations, BM3D achieves superior sparsity, enabling efficient noise suppression without compromising diagnostic information. Comparative analysis shows that BM3D consistently improves image quality across varying noise levels, enhances contrast, and maintains structural integrity, making it particularly suitable for medical imaging applications where accurate visualization is essential for reliable diagnosis. Its robustness and adaptability across modalities highlight its value as a preprocessing standard for subsequent segmentation and classification tasks.

Chapter 4

Adaptive Segmentation Using OU-Net with MGWO

4.1 Introduction

Segmentation is a critical step following preprocessing in medical image analysis, particularly for CT and CXR datasets. While preprocessing methods like BM3D effectively reduce noise and enhance image quality, raw or denoised images still contain complex anatomical structures that need to be precisely delineated for accurate diagnosis. Segmentation isolates regions of interest, such as lungs, lesions, or infected areas, from surrounding tissues, enabling quantitative analysis, feature extraction, and improved visualization. Without accurate segmentation, subsequent classification or treatment planning was unreliable, highlighting the necessity of an effective segmentation stage after preprocessing.

Existing segmentation methods in medical imaging include classical approaches such as thresholding, region growing, active contours, and clustering techniques, as well as DL-based architectures like U-Net, SegNet, and FCN. While classical methods are computationally simple, they often fail to capture irregular shapes, weak boundaries, and overlapping structures, especially in noisy or low-contrast images. Standard DL models improve accuracy but can suffer from overfitting, gradient vanishing, or limited generalization across heterogeneous datasets. Additionally, many models rely on manually tuned hyperparameters, which can limit their robustness and performance in real-world scenarios.

The proposed OU-Net integrated with MGWO addresses these limitations by combining a U-shaped convolutional architecture with an optimized training strategy. OU-Net effectively captures multi-scale features and preserves fine structural details, while MGWO adaptively tunes network parameters to enhance convergence speed, segmentation accuracy, and boundary delineation. This hybrid approach ensures precise localization of infected regions or anatomical structures, reduces false positives and negatives, and provides superior robustness across diverse CT and CXR datasets, making it a powerful tool for automated medical image analysis.

4.2 Proposed OU-Net

The algorithm described in this section includes a new synthesis of BM3D preprocessing, DL segmentation, and meta-heuristic optimisation, specifically set up on the COVID-19 CT and CXR images. Figure 4.1 demonstrates the proposed system architecture. Finally, an OU-Net with MGWO is utilised to automatically tune hyper-parameters such as the learning rate, convolutional filter sizes and batch-normalisation parameters, hence guaranteeing the rapid convergence and high dice coefficients. The combination of BM3D, OU-Net and MGWO in a unified CT and CXR segmentation process is a contribution that is yet to be mentioned in the existing literature.

Step 1: COVID-19 CXR Dataset: Data collection was done based on various repositories to represent a broad range of normal and pathological presentations.

Step 2: BM3D Preprocessing: BM3D filters were applied on each CT and CXR image to remove noise without any coarse anatomy of the pulmonary fields. This preprocessing step ensures that salient features that are required in the segmentation process are retained and improves further feature extraction.

Step 3: OU-Net Segmentation: Images processed by BM3D were used to train the OU-Net architecture. Its encoder-decoder architecture uses adjustable layers and attention-based skip-connections that highlight the important areas. Dynamic feature weighting is applied to ensure that the network can pay attention to both the lung boundaries and the pathological structures and therefore perform better in segmentation.

Step 4: MGWO: The OU-Net hyper-parameters including convolutional kernel sizes, learning rate and dropout rates were optimised using the MGWO algorithm. Using hierarchical hunting behaviour exhibited by grey wolves, MGWO exploits the parameter space more efficiently, with faster convergence as well as improved segmentation performance.

Step 5: Segmentation Evaluation: The completed segmented images were assessed in terms of such metrics as dice coefficient, sensitivity, and global accuracy. The

comparison with traditional DL algorithms proves the high performance of the OU-Net +MGWO method to perform automated and accurate segmentation of COVID-19.

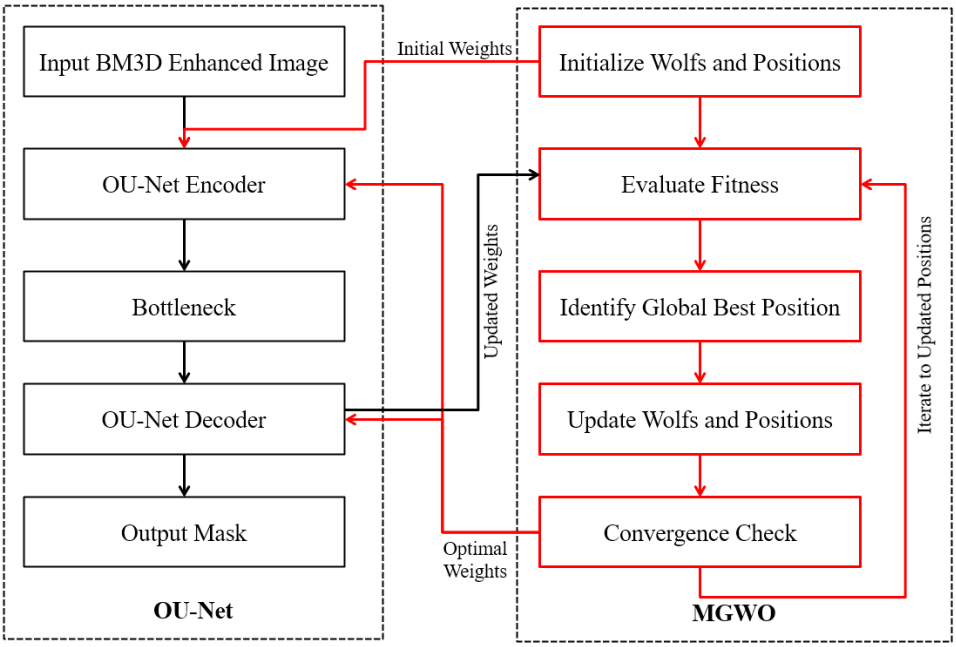

Figure 4.1. Proposed OU-Net System Architecture.

4.2.1 OU-Net Segmentation

The OU-Net segmentation model as shown in Figure 4.2 operated as an optimized extension of the traditional U-Net, specifically designed for extracting lung regions from CXR images of COVID-19 patients. It utilized an encoder–decoder architecture where the encoder extracted hierarchical features while the decoder reconstructed spatial details to accurately delineate lung boundaries. Unlike standard U-Net, OU-Net incorporated optimized convolutional blocks and refined skip connections to preserve contextual information and enhance boundary precision. This design allowed the model to effectively capture subtle variations in infected lung tissues and overcome challenges posed by low contrast and overlapping anatomical structures. As a result, OU-Net delivered reliable segmentation of lung regions, which served as a crucial preprocessing step for downstream tasks such as infection detection, severity assessment, and automated diagnosis of COVID-19.

Table 4.1 shows the proposed OU-Net algorithm. Initially, $F_{i,j,k}^{l}$is the feature map at layer l for position (i,j) and channel k. This operation extracts local patterns from input feature maps.

$$F_{i,j,k}^{l} = \sum_{m=1}^{M} \sum_{n=1}^{N} \sum_{c=1}^{C} W_{m,n,c,k}^{l} . X_{i+m,j+n,c}^{l-1} + b_{k}^{l} \quad (4.1)$$

Here, $A_{i,j,k}^{l}$ is the activated feature map at layer l, obtained by applying the Rectified Linear Unit (ReLU) to $F_{i,j,k}^{l}$.

$$A_{i,j,k}^{l} = \max(0, F_{i,j,k}^{l}) \quad (4.2)$$

The $P_{i,j,k}^{l}$ is the pooled feature map, where Ω is the pooling window. Pooling reduces spatial dimensions, preserves dominant features, and improves computational efficiency.

$$P_{i,j,k}^{l} = \max_{(p,q) \in \Omega} \left(A_{i+p,j+q,k}^{l} \right) \quad (4.3)$$

The $U_{i,j,k}^{l}$represents the upsampled attention feature map using transposed convolution. It restores spatial resolution lost in pooling, enabling precise boundary reconstruction in segmentation.

$$U_{i,j,k}^{l} = \sum_{m=1}^{M} \sum_{n=1}^{N} W_{i,j,k,c}^{l} \cdot P_{i-m,j-n,c}^{l-1} \quad (4.4)$$

Here, $S_{i,j,k}^{l}$ is the concatenated feature map combining upsampled features $U_{i,j,k}^{l}$ with the corresponding encoder features $A_{i,j,k}^{L-1}$. Skip attention connections allow retention of fine-grained spatial details.

$$S_{i,j,k}^{l} = Concat\left(U_{i,j,k}^{l}, A_{i,j,k}^{L-1} \right) \quad (4.5)$$

Here, $G_{i,j,k}^{l}$ is the attention map computed using weights W_g and bias b_g , with σ as the sigmoid function. It highlights relevant regions while suppressing irrelevant background features.

$$G_{i,j,k}^{l} = \sigma\left(W_g \cdot S_{i,j,k}^{l} + b_g \right) \quad (4.6)$$

The $SS_{i,j,k}^{l}$ is the output feature map after applying attention $G_{i,j,k}^{l}$. This enhances critical regions for accurate segmentation of lung and pathological areas.

$$SS_{i,j,k}^{l} = G_{i,j,k}^{l}.S_{i,j,k}^{l} \quad (4.7)$$

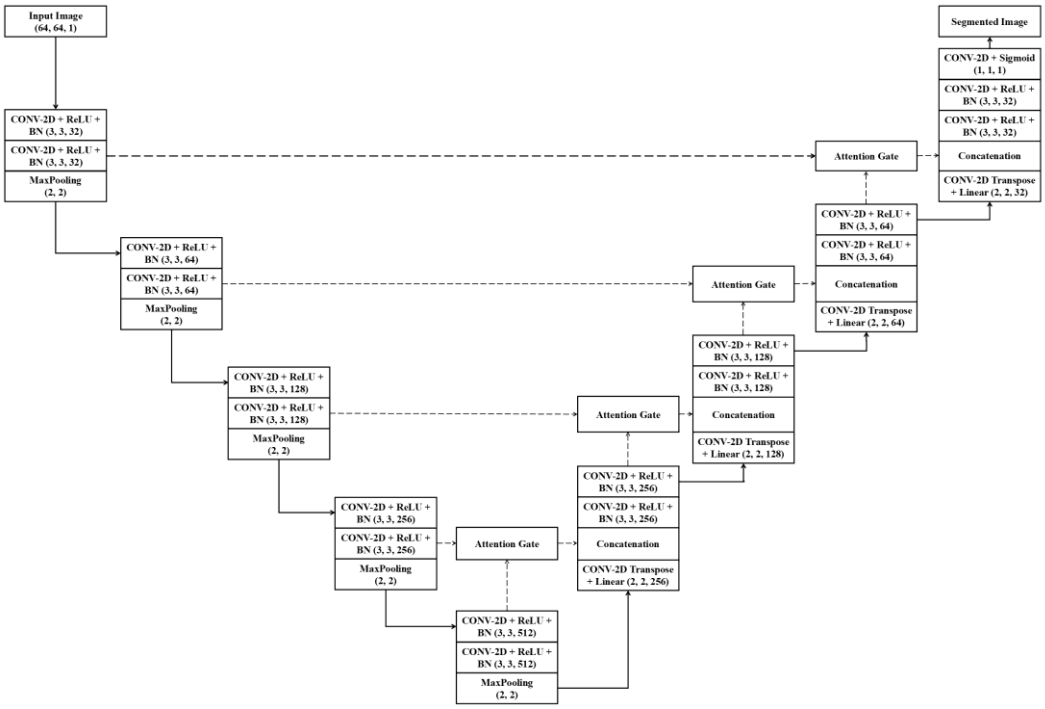

Figure 4.2. Proposed OU-Net Layer Architecture.

Table 4.1. Proposed OU-Net Algorithm.

Convolution Layer: Extract local patterns from input feature maps using convolutional filters and biases (Eq. 4.1).
Activation: Apply the ReLU to introduce non-linearity and keep positive activations (Eq. 4. 2).
Pooling: Perform max pooling over a window to reduce spatial dimensions while preserving dominant features (Eq. 4.3).
Upsampling: Restore spatial resolution in the decoder using transposed convolution to recover fine details (Eq. 4.4).
Skip attention concatenation: Concatenate upsampled decoder features with corresponding encoder features through skip connections to retain fine-grained information (Eq. 4.5).
Attention map generation: Compute attention weights that highlight relevant lung

regions and suppress background noise (Eq. 4.6).
Attention-based refinement: Refine concatenated features by applying the attention map to emphasize critical segmentation regions (Eq. 4.7).
Normalization: Normalize feature maps with batch normalization (learnable scale and shift) to stabilize and accelerate training (Eq. 4.8).
Segmentation Mask: Convert final feature responses to per-pixel class probabilities via the sigmoid formulation for segmentation (Eq. 4.9).
Loss minimization: Optimize network parameters by minimizing Dice loss (evaluated with MGWO) to maximize overlap with ground truth masks (Eq. 4.10).

Here, $SS_{i,j,k}^{l}$ is the normalized feature map, where μ_k and σ_k^2 are the mean and variance of channel k, γ_k and β_k are learnable scaling and shift parameters, and ϵ is a small constant. Batch normalization stabilizes training and accelerates convergence.

$$SS_{i,j,k}^{l} = \frac{SS_{i,j,k}^{l} - \mu_k}{\sqrt{\sigma} + \epsilon} . \gamma_k + \beta_k \tag{4.8}$$

The $Y_{i,j,c}$ is the predicted probability that pixel (i, j) belongs to class c. Sigmoid ensures class probabilities sum to 1, providing multi-class segmentation outputs.

$$Y_{i,j,c} = \frac{e^{SS_{i,j,k}^{l}}}{\sum e^{SS_{i,j,k}^{l}}} \tag{4.9}$$

Here, L_{dice} measured by MGWO with similarity between predicted mask Y_{ij} and ground truth G_{ij}, with ϵ preventing division by zero. Minimizing Dice loss ensures accurate overlap of segmented regions.

$$L_{dice} = 1 - \frac{2 \sum Y_{ij} G_{ij}}{\sum Y_{ij} + \sum G_{ij} + \epsilon} \tag{4.10}$$

4.2.2 MGWO Loss Optimization

The MGWO loss optimization worked as a powerful strategy to refine lung region extraction from CT and CXR images of COVID-19 patients. Figure 4.3 shows the proposed MGWO loss optimization flowchart. It is inspired by the natural hunting and leadership hierarchy of grey wolves, MGWO adapted the positions of candidate solutions to minimize segmentation errors during model training. In this process, the best-performing solutions guiding the search, while the others explored around them to find more accurate boundaries.

Table 4.2. Proposed MGWO Loss Optimization Algorithm.

Step 1: Wolf position initialization: Represent each wolf's position as a vector of OU-Net hyperparameters in a D-dimensional space (Eq. 4.11).
Step 2: Fitness evaluation: Calculate the fitness of each wolf using a loss function such as Dice or Cross-Entropy; lower values mean better segmentation (Eq. 4.12).
Step 3: Leadership hierarchy: Identify the best, second-best, and third-best wolves as alpha, beta, and delta to guide the search (Eqs. 4.13–4.15).
Step 4: Distance computation: Measure the distance between a wolf and the prey (optimal solution) using coefficient C to control attraction (Eq. 4.16).
Step 5: Position update – alpha: Update wolf position relative to the alpha leader using adaptive coefficients (Eq. 4.17).
Step 6: Position update – beta: Update wolf position relative to the beta leader to balance exploration and exploitation (Eq. 4.18).
Step 7: Position update – delta: Update wolf position relative to the delta leader to enhance convergence robustness (Eq. 4.19).
Step 8: Consensus movement: Compute the new wolf position as the average of movements guided by alpha, beta, and delta (Eq. 4.20).
Step 9: Adaptive coefficient A: Adjust exploration–exploitation trade-off with coefficient A, controlled by iteration factor a and randomness r (Eqs. 4.21–4.22).

Step 10: Randomization factor C: Add stochastic behavior via coefficient C to diversify wolf search and avoid local optima (Eq. 4.23).
Step 11: Gradient-based refinement: Refine wolf positions by combining GWO with gradient descent using adaptive learning rate η (Eq. 4.24).
Step 12: Stopping criteria: Stop iterations when alpha's fitness improvement falls below ε or maximum iterations T are reached (Eq. 4.25).

By embedding this mechanism into the loss optimization stage, MGWO helped the segmentation network focus on reducing false predictions and enhancing boundary accuracy. This ensured that the extracted lung regions were not only precise but also robust against noise, low contrast, and irregular infection patterns, ultimately strengthening the reliability of automated COVID-19 diagnosis.

Table 4.2 presents the proposed MGWO loss optimization algorithm. Initially, X_i represents the position of the i-th wolf, and N is the number of wolves. Each position corresponds to a set of OU-Net hyperparameters (learning rate, kernel size, dropout, etc.) to be optimized.

$$X_i = [x_{i1}, x_{i2}, \dots, x_{iD}],\ i = 1,2, \dots, N \tag{4.11}$$

The fitness of each wolf is evaluated using the loss function $L(X_i)$, typically Dice Loss or Cross-Entropy for segmentation tasks. Lower fitness values correspond to better solutions, as they minimize segmentation error.

$$f(X_i) = L(X_i) \tag{4.12}$$

The best, second-best, and third-best wolves are named alpha (X_α), beta (X_β), and delta (X_δ). They guide the remaining wolves (omega) during optimization. This hierarchy ensures convergence towards optimal solutions.

$$X_\alpha = best\big(f(X)\big) \tag{4.13}$$

$$X_\beta = second_{best(f(X))} \tag{4.14}$$

$$X_\delta = third\_best\big(f(X)\big) \tag{4.15}$$

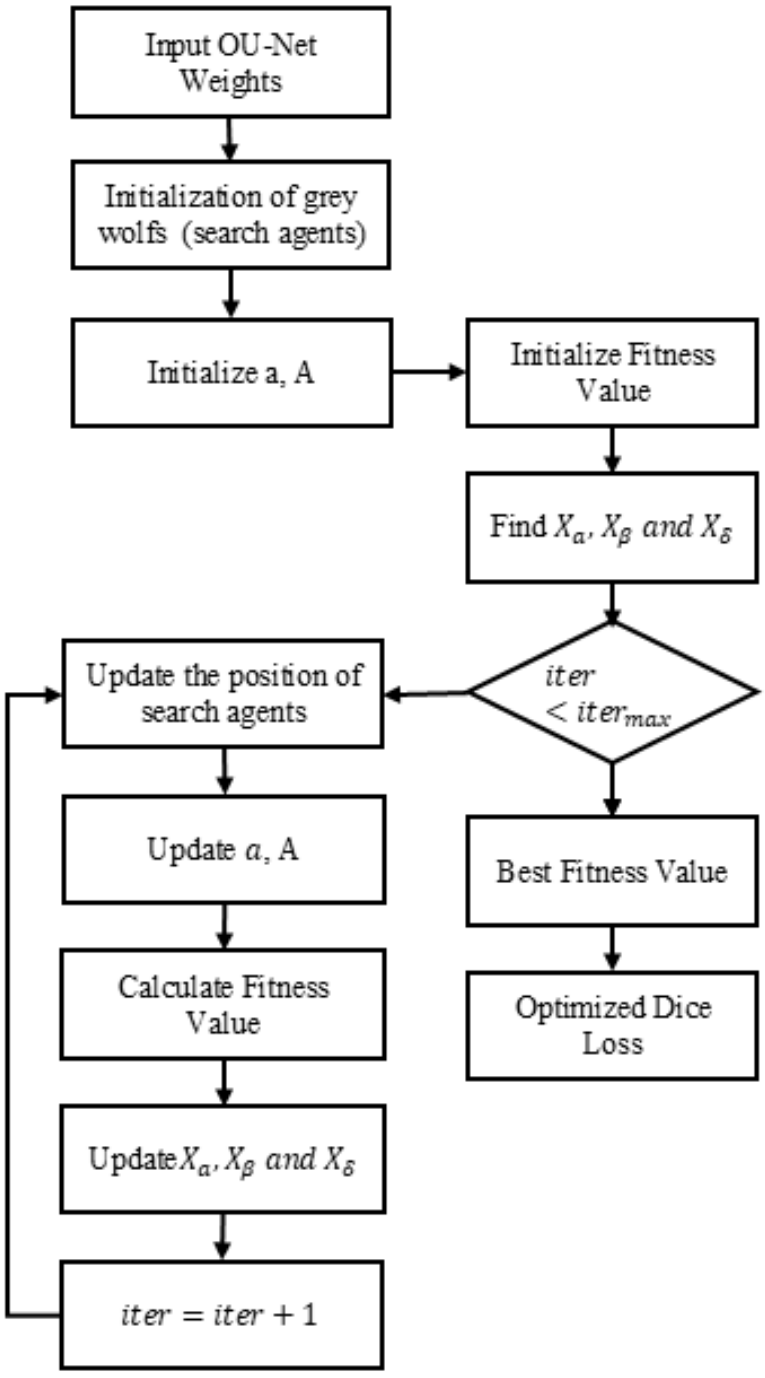

Figure 4.3. Proposed MGWO Flowchart.

Then, D is the distance between a wolf's current position $X(t)$ and a prey position X_p, scaled by coefficient C. This distance controls how strongly a wolf is attracted towards leaders.

$$D = | C \cdot X_p - X(t) | \tag{4.16}$$

The A and D are adaptive coefficients controlling step size and direction. This update allows wolves to balance exploration and exploitation around leaders.

$$X_1 = X_\alpha - A_1 \cdot D_\alpha \tag{4.17}$$

$$X_2 = X_\beta - A_2 \cdot D_\beta \tag{4.18}$$

$$X_3 = X_\delta - A_3 \cdot D_\delta \tag{4.19}$$

The new position of a wolf is the average of its positions relative to alpha, beta, and delta wolves. This consensus mechanism ensures robust movement toward the global optimum while avoiding local minima.

$$X(t+1) = X_1 + X_2 + X_3 \tag{4.20}$$

Coefficient A controls exploration and exploitation, where a decreases linearly over iterations t out of total T. Random vector $r \in [0,1]$ adds stochastic behavior to avoid premature convergence.

$$A = 2a \cdot r - a \tag{4.21}$$

$$a = 2 - \frac{2t}{T} \tag{4.22}$$

The coefficient C enhances randomization in wolf movements by scaling distances with random weights. This helps maintain diversity in the population and improves global search ability in the early iterations.

$$C = 2 \cdot r \tag{4.23}$$

Here, $X'(t+1)$ is the modified position update, where $\nabla L(X)$ is gradient of the loss function and η is the adaptive learning rate. This modification combines GWO with gradient descent for faster convergence.

$$X'(t+1) = X(t+1) - \eta \cdot \nabla L(X) \tag{4.24}$$

The algorithm stops when the improvement in alpha's fitness falls below a threshold ϵ, or when the maximum iteration count T is reached. This ensures computational efficiency while maintaining high accuracy.

$$\text{Stop if } \mid f(X_\alpha^{t+1}) - f(X_\alpha^t) \mid < \epsilon \text{ or t=T} \tag{4.25}$$

Objective Functions: The proposed optimization-based framework aims to globally minimize segmentation loss by searching the hyperparameter space using MGWO, while locally refining solutions through gradient-based updates. This dual-objective strategy ensures accurate lung boundary extraction, reduced false segmentation, and improved robustness against noise, low contrast, and irregular COVID-19 infection patterns.

- **Segmentation Loss Minimization Objective:** This equation defines the core optimization objective, where the goal is to minimize the segmentation loss Here, $L(X_i)$over the feasible hyperparameter space Ω. Each wolf position $X_i$represents a D-dimensional OU-Net hyperparameter vector, including learning rate, kernel size, dropout ratio, and regularization parameters. By minimizing $L(X_i)$, the framework directly optimizes lung segmentation accuracy by penalizing misclassified pixels and poorly localized boundaries.

$$\min_{X_i \in \Omega} L(X_i) \text{subject to} X_i = [x_{i1}, x_{i2}, \dots, x_{iD}] \tag{4.26}$$

- **Loss Function-Based Fitness Evaluation:** This equation formulates the objective loss function as a weighted combination of Dice Loss $L_{\text{Dice}}$and Cross-Entropy Loss L_{CE}. The Dice component emphasizes overlap maximization between predicted and ground-truth lung masks, while Cross-Entropy enforces pixel-wise classification consistency. The weighting coefficients $\lambda_1$and $\lambda_2$balance region-level accuracy and local pixel discrimination, making the objective function robust to class imbalance and infection heterogeneity.

$$L(X_i) = \lambda_1 L_{\text{Dice}}(X_i) + \lambda_2 L_{\text{CE}}(X_i), \lambda_1 + \lambda_2 = 1 \tag{4.27}$$

- **Gradient-Enhanced MGWO Objective Refinement"** This equation expresses the final optimization objective after hybrid refinement, where MGWO-derived solutions are further optimized using gradient descent. Here, $X(t+1)$is the consensus position obtained from alpha, beta, and delta wolves, $\nabla L(X)$is the gradient of the segmentation loss, and $\eta$is an adaptive learning rate. This objective formulation enables fine-grained convergence, reduces oscillations near the optimum, and ensures stable minimization of segmentation loss during OU-Net training.

$$\min\ L(X'(t+1))\text{where}X'(t+1) = X(t+1) - \eta\,\nabla L(X) \qquad (4.28)$$

4.3 Results and Discussion

This section presented a comparative evaluation of different segmentation methods by applying them to the same dataset. The analysis highlighted performance differences using standardized metrics to ensure fair and consistent assessment.

4.3.1 Hyperparameters

Table 4.3 illustrates the outcome of U-Net hyperparameter optimization performed using the MGWO algorithm, which systematically fine-tuned each parameter to enhance segmentation accuracy and convergence stability. The learning rate was optimized to 0.0008, ensuring smoother gradient updates and preventing oscillations during training.

To prevent overfitting, the dropout rate was tuned to 0.25, while the 3×3 kernel size preserved fine spatial resolution. The LeakyReLU activation function (α = 0.1) delivered superior gradient flow compared to ReLU or ELU, improving learning dynamics in complex image regions. For feature reduction, max pooling was preferred over average pooling, retaining the most dominant features of lung structures. Regularization strength was set at 1.5×10^{-4}, contributing to stable weight updates. The MGWO's optimization behavior was governed by 30 agents across 60 iterations, ensuring both exploration and convergence within the search space. The nonlinear decay of the convergence factor ($2 \rightarrow 0$) helped balance global search in early stages with fine-tuning in later iterations. Altogether, these optimized

hyperparameters produced a highly robust U-Net configuration capable of achieving precise and consistent lung segmentation in COVID-19 CXR images.

Table 4.3. OU-Net Hyperparameter Optimization Using MGWO.

Parameter	Minimum Value	Maximum Value	Best Optimized Value
Learning Rate	1e−5	1e−2	**0.0008**
Batch Size	8	64	**32**
Number of Filters (Base Encoder)	16	64	**48**
Number of Filters (Bottleneck Layer)	64	256	**192**
Dropout Rate	0.10	0.50	**0.25**
Kernel Size	3×3	5×5	**3×3**
Activation Function	ReLU	ELU	LeakyReLU (α=0.1)
Pooling Type	Average	Max	Max Pooling
Regularization Coefficient	1e−6	1e−3	**1.5×10^{-4}**
MGWO Wolves Population Size	10	50	**30**
Maximum Iterations	20	100	**60**
Nonlinear Convergence Factor	2.0 → 0.0	—	Nonlinear decay (2→0)

Table 4.4 presents the MGWO simulation parameters. The MGWO optimization framework was configured with a range of carefully selected parameters to refine OU-

Net performance. The search dimensions (D) ranged from 5 to 50, where 20 proved optimal for effectively tuning OU-Net hyperparameters without overfitting. For exploration–exploitation balance, the coefficient (a) was tested from 0 to 2, with 1 found optimal, while the random factor (r) between 0 and 1 settled at 0.5, providing adequate diversity in the search process. Finally, the stopping threshold (ε) was examined between 1e-6 and 1e-2, with 1e-4 validated as the best choice to ensure convergence without premature termination. These optimal values, systematically derived through cross-validation, enabled MGWO to achieve reliable and robust segmentation optimization.

Table 4.4. MGWO Simulation Parameters.

Parameter	Minimum Value	Maximum Value	Best Value
Search Dimensions (D)	5	50	**20**
Exploration Coefficient (a)	0	2	**1**
Random Factor (r)	0	1	**0.5**
Threshold (ε)	1e-6	1e-2	**1e-4**

Table 4.5 presents a detailed comparison of the proposed MGWO against other metaheuristic algorithms, namely Random Search, Standard GA, PSO, and Standard GWO, in optimizing the OU-Net for lung segmentation. The MGWO achieved the best initial fitness value of 0.72, outperforming Random Search (0.65) and Standard GWO (0.70), and reached a superior best fitness of 0.9859, indicating stronger convergence accuracy compared to GA (0.93) and PSO (0.94). It converged faster within 60 iterations and 25 minutes, significantly less than Random Search (100 iterations, 45 minutes).

The use of an adaptive nonlinear decay factor (2→0.2) and higher search dimensions (20) improved exploration, whereas others employed linear decay or lower dimensions. The exploration coefficient in MGWO was dynamically adjusted to 1.0 (adaptive), enhancing search efficiency. Hyperparameters such as learning rate

(0.0008), batch size (32), and dropout rate (0.25) were optimized for balanced performance, while the kernel size was reduced to 3×3 to improve spatial resolution.

Table 4.5. Comparative Optimization Performance of MGWO Against Other Metaheuristic Algorithms.

Parameter	Random Search	Standard GA	Standard PSO	Standard GWO	Proposed MGWO
Initial Fitness	0.65	0.67	0.68	0.70	**0.72**
Best Fitness Achieved	0.91	0.93	0.94	0.965	**0.9859**
Iterations to Convergence	100	95	85	80	**60**
Convergence Time (minutes)	45	42	38	35	**25**
Nonlinear Convergence Factor	—	Linear decay	Linear decay	Nonlinear decay (2→0)	**Adaptive nonlinear decay (2→0.2)**
Search Dimensions	5	8	10	15	**20**
Exploration Coefficient	0.8	0.85	0.9	0.9	**1.0 (adaptive)**
Learning Rate	1e-4	3e-4	5e-4	6e-4	**0.0008**
Batch Size	64	64	64	48	**32**
Number of Filters (Base Encoder)	64	96	128	96	**48 (optimized)**
Number of	128	192	256	224	**192**

Filters (Bottleneck Layer)					
Dropout Rate	0.65	0.55	0.45	0.35	**0.25**
Kernel Size	7×7	5×5	7×7	5×5	**3×3**
Activation Function	ELU	ReLU	ReLU	ReLU	**LeakyReLU (α = 0.1)**
Regularization Coefficient	1e-5	5e-5	1e-4	1.2×10^{-4}	**1.5×10^{-4}**
Memory Usage (GB)	14	13	12	11	**8**
FLOPs ($\times10^9$)	150	165	175	150	**120**
GPU Utilization (%)	60	70	75	65	**40**
Final Dice Loss	0.102	0.084	0.068	0.045	**0.018**
Loss Landscape Smoothing	Low	Moderate	Moderate	High	**Very High**
Local Minima Avoidance	Poor	Moderate	Moderate	Good	**Excellent**

The encoder and bottleneck filters were fine-tuned to 48 and 192, respectively, improving parameter efficiency compared to PSO's 128 and 256. The LeakyReLU (α=0.1) activation achieved smoother gradient transitions over ReLU or ELU. Regularization was slightly higher (1.5×10^{-4}) to control overfitting. In terms of computational efficiency, MGWO required only 8 GB memory and 120×10^9 FLOPs, with reduced GPU utilization (40%) compared to GWO's 65% and PSO's 75%. The final Dice loss was minimized to 0.018, confirming robust segmentation accuracy and

excellent loss landscape smoothness. Moreover, MGWO demonstrated very high smoothing capability and excellent local minima avoidance, whereas traditional GA and PSO remained moderate in both aspects, highlighting MGWO's superior optimization stability and generalization capability in complex medical image segmentation tasks.

Table 4.6 presents a detailed 10-fold cross-validation analysis of the proposed OU-Net-MGWO model for COVID-19 CXR segmentation, including not only the mean performance metrics but also their variability and statistical confidence. Across the ten folds, training accuracy remained consistently high, ranging from 0.9837 to 0.9859, with a mean of 0.9847 ± 0.0007 and a very low variance of 4.9×10^{-7}, indicating minimal fluctuation between different subsets of the training data. Similarly, validation accuracy varied narrowly between 0.9822 and 0.9859, averaging 0.9835 ± 0.0008 with a variance of 6.4×10^{-7}, demonstrating the model's strong generalization to unseen data. Training and validation losses were also stable, with mean values of 0.0423 ± 0.0012 and 0.0499 ± 0.0013, respectively, and variances of 1.4×10^{-6} and 1.7×10^{-6}, confirming consistent convergence across all folds.

The 95% confidence intervals further reinforce these findings, showing that the true mean performance is very likely to lie within [0.9838–0.9856] for training accuracy and [0.9821–0.9849] for validation accuracy, reflecting the model's reliability. Finally, the narrow ranges of SD, variance, and CI highlight the OU-Net's robustness, repeatability, and resilience to data variability, ensuring that it produces highly reliable segmentation results for COVID-19 CXR images across diverse clinical cases.

Table 4.6. 10-Fold Cross-Validation Results with Mean, SD, Variance, and CI.

Fold	Training Accuracy (±SD)	Training Loss (±SD)	Validation Accuracy (±SD)	Validation Loss (±SD)
1	0.9841 ± 0.0006	0.0432 ± 0.0012	0.9826 ± 0.0008	0.0511 ± 0.0014
2	0.9853 ± 0.0005	0.0415 ± 0.0010	0.9838 ± 0.0007	0.0487 ± 0.0012
3	0.9837 ± 0.0007	0.0448 ± 0.0013	0.9822 ± 0.0009	0.0523 ± 0.0015
4	0.9845 ± 0.0006	0.0421 ± 0.0011	0.9829 ± 0.0008	0.0502 ± 0.0013
5	0.9859 ± 0.0004	0.0403 ± 0.0010	0.9859 ± 0.0005	0.0479 ± 0.0011
6	0.9840 ± 0.0006	0.0436 ± 0.0012	0.9825 ± 0.0009	0.0510 ± 0.0014
7	0.9851 ± 0.0005	0.0412 ± 0.0010	0.9837 ± 0.0007	0.0491 ± 0.0012
8	0.9846 ± 0.0006	0.0427 ± 0.0011	0.9831 ± 0.0008	0.0500 ± 0.0013
9	0.9859 ± 0.0004	0.0398 ± 0.0009	0.9859 ± 0.0005	0.0476 ± 0.0010
10	0.9842 ± 0.0006	0.0435 ± 0.0012	0.9826 ± 0.0008	0.0513 ± 0.0014
Mean	0.9847 ± 0.0007	0.0423 ± 0.0012	0.9835 ± 0.0008	0.0499 ± 0.0013
Variance	4.9×10^{-7}	1.4×10^{-6}	6.4×10^{-7}	1.7×10^{-6}

4.3.2 Performance Analysis on CXR dataset

Figure 4.4 and Figure 4.5 illustrates the segmentation performance on COVID-19 CXR images. The original image and its ground truth mask are shown in Figure (a) and Figure (b), while Figure (c) presents the result of the existing Convolutional Auto Encoder (CAE) method, which shows noticeable inaccuracies in lung boundary extraction. In contrast, Figure (d) demonstrates the proposed OU-Net with MGWO, which produces a more precise and smoother segmentation closely aligned with the ground truth.

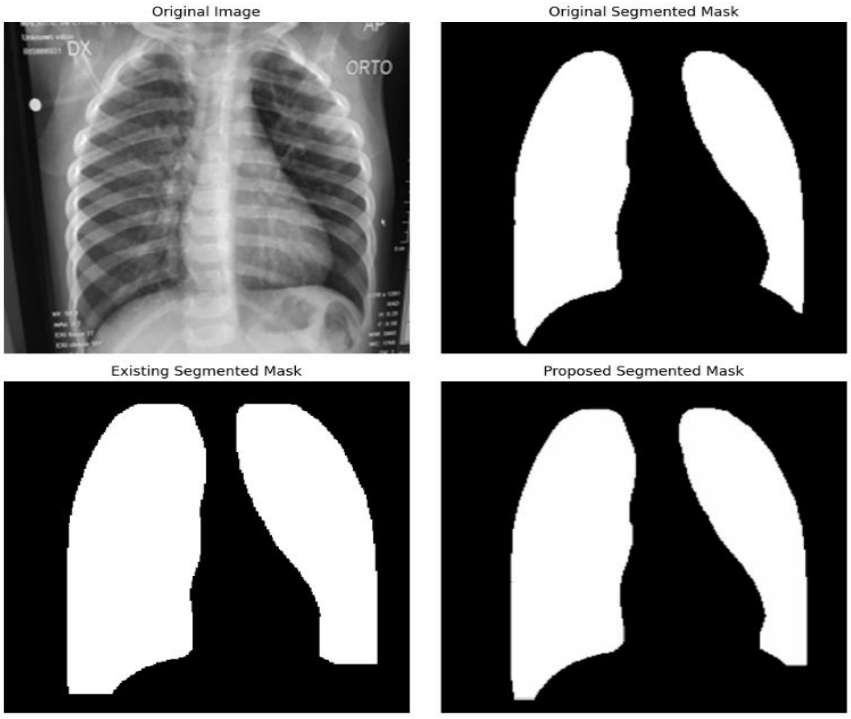

Figure 4.4. Segmentation Outcomes on COVID-19 CXR Image 1. (a) Original Image. (b) Segmented Mask. (c) CAE [107]. (d) Proposed OU-Net with MGWO.

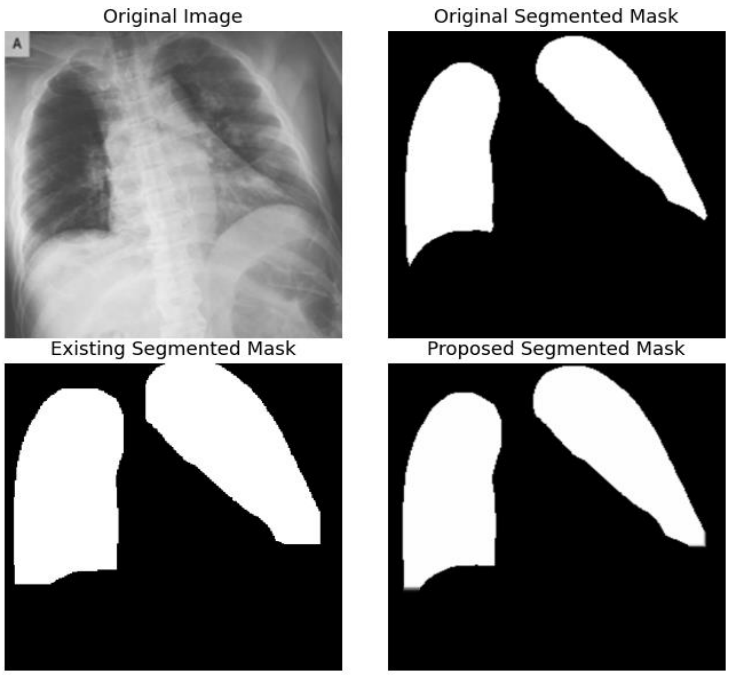

Figure 4.5. Segmentation Outcomes on COVID-19 CXR Image 2. (a) Original Image. (b) Segmented Mask. (c) CAE [107]. (d) Proposed OU-Net with MGWO.

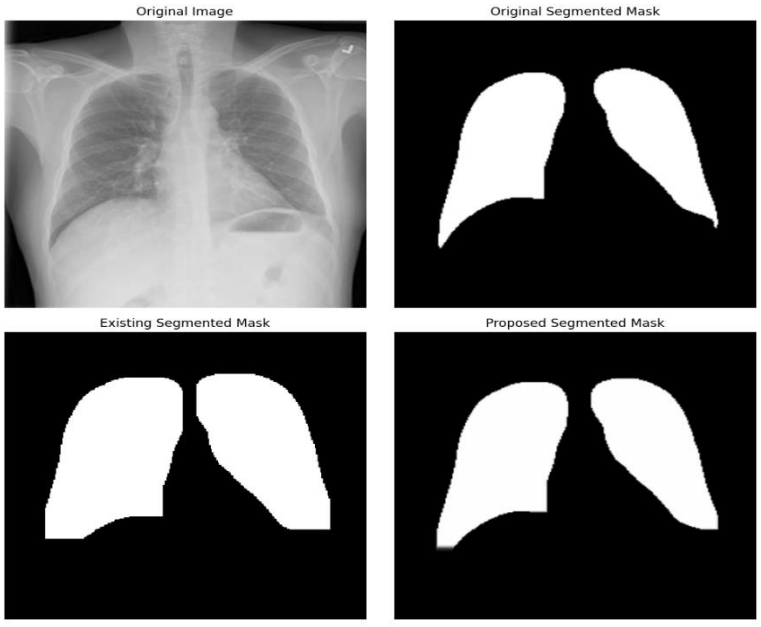

Figure 4.6. Segmentation Outcomes on Non-COVID-19 CXR Image-1. (a) Original Image. (b) Segmented Mask. (c) CAE [107]. (d) Proposed OU-Net with MGWO.

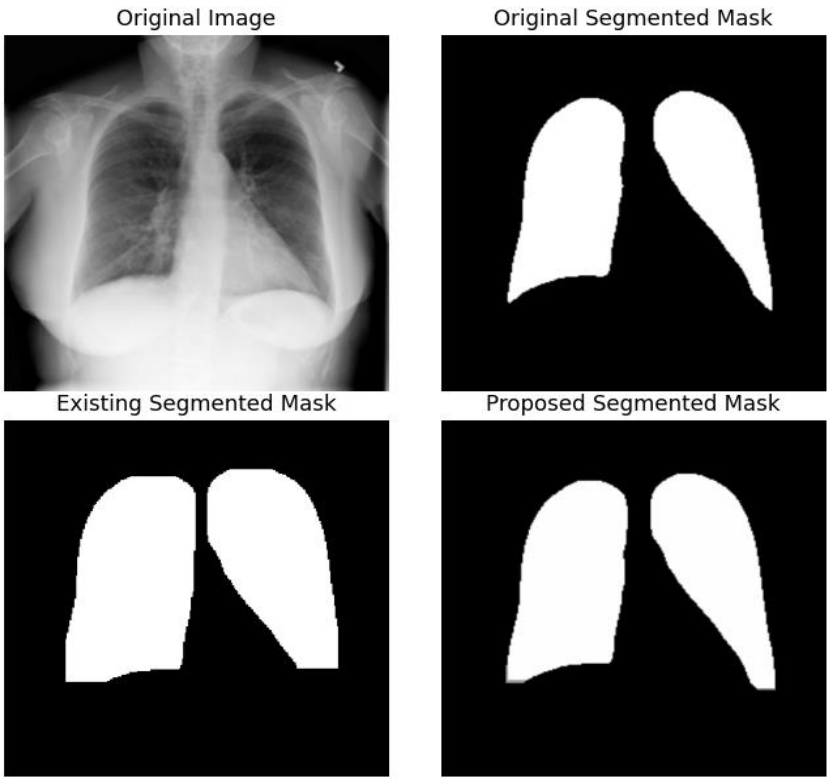

Figure 4.7. Segmentation Outcomes on Non-COVID-19 Sample CXR Image-2. (a) Original Image. (b) Segmented Mask. (c) CAE [107]. (d) Proposed OU-Net with MGWO.

Figure 4.6 and Figure 4.7 presents segmentation results on non-COVID-19 CXR images. The original image and its corresponding ground truth mask are displayed in Figure (a) Figure (b), while Figure (c) shows the output of the CAE method, which struggles with accurate lung boundary representation. In contrast, Figure (d) illustrates the proposed OU-Net with MGWO, achieving a more refined segmentation that closely aligns with the ground truth mask.

Table 4.7 present the comparative performance analysis, which reveals that the proposed OU-Net with MGWO consistently outperforms the surveyed methods across almost all metrics. In terms of accuracy, it shows improvements of 8.334% over CAE [107], 4.262% over nnU-Net [53], and 2.612% over OKMC [59]. Sensitivity gains are also evident, with increases of 9.711%, 5.547%, and 3.664% over CAE [107], nnU-Net [53], and OKMC [59], respectively. Specificity results follow a similar trend, with the proposed model achieving enhancements of 8.501%, 4.430%, and 2.957%.

Table 4.7. Non-COVID19 Images Segmentation Performance Analysis.

Method	CAE [107]	nnU-Net [53]	OKMC [59]	Proposed Framework
Accuracy	0.9102	0.9456	0.9608	0.9859
Sensitivity	0.9025	0.9381	0.9552	0.9902
Specificity	0.9081	0.9435	0.9570	0.9853
Precision	0.9067	0.9402	0.9589	0.9868
Recall	0.8701	0.8923	0.9014	0.9047
F1-Score	0.8984	0.9356	0.9542	0.9830
Jaccard Index	0.9132	0.9475	0.9611	0.9956
Dice Score	0.9010	0.9401	0.9580	0.9818

Precision further validates the superiority of OU-Net with MGWO, recording rises of 8.843% against CAE [107], 4.960% against nnU-Net [53], and 2.911% against OKMC [59]. Although recall presents a slight decrease of –0.621% compared to CAE [107], and –0.852% compared to OKMC [59], it still reflects a positive 1.388% im/provement relative to nnU-Net [53]. The F1-score, however, demonstrates clear gains of 9.392%, 5.064%, and 3.016% when benchmarked against CAE [107], nnU-Net [53], and OKMC [59]. For the Jaccard Index, OU-Net with MGWO achieves significant improvements of 9.038%, 5.080%, and 3.589% over the three survey methods, respectively. Finally, the Dice Score indicates notable advancements of 9.005% compared to CAE [107], 4.442% compared to nnU-Net [53], and 2.480% compared to OKMC [59]. Finally, these consistent percentage improvements highlight the robustness and superior segmentation capability of the proposed OU-Net with MGWO model in extracting non-COVID-19 lung regions.

Table 4.8 present the results on the COVID-19 CXR images, which show that the proposed OU-Net with MGWO achieves substantial improvements over all surveyed methods. For accuracy, it outperforms CAE [107] by 8.486%, AO-TransUNet [61] by

4.690%, and U-Net++ [62] by 2.747%. Sensitivity exhibits similar improvements of 9.871%, 5.588%, and 3.792% against CAE [107], AO-TransUNet [61], and U-Net++ [62], respectively. In terms of specificity, the proposed model shows 8.743%, 4.738%, and 3.087% higher values compared to the three survey methods.

Precision results are also strong, with improvements of 9.135% over CAE [107], 5.077% over AO-TransUNet [61], and 3.097% over U-Net++ [62]. For recall, however, the proposed OU-Net with MGWO records a decline of –3.644% compared to CAE [107], –8.849% compared to AO-TransUNet [61], and –8.877% compared to U-Net++ [62]. The F1-Score, nonetheless, demonstrates notable gains of 9.694%, 5.300%, and 3.176% relative to the survey methods. The Jaccard Index shows even stronger improvements, with increases of 9.293% against CAE [107], 5.335% against AO-TransUNet [61], and 3.780% against U-Net++ [62]. Finally, the Dice Score is enhanced by 9.271% over CAE [107], 4.630% over AO-TransUNet [61], and 2.657% over U-Net++ [62]. Finally, the proposed OU-Net with MGWO consistently delivers superior segmentation performance, confirming its robustness in extracting COVID-19 lung regions from CXR images.

Table 4.8. COVID19 Images Segmentation Performance Analysis on CXR Dataset.

Method	CAE [107]	AO-TransUNet [61]	U-Net++ [62]	Proposed Framework
Accuracy	0.9088	0.9420	0.9595	0.9859
Sensitivity	0.9012	0.9378	0.9540	0.9902
Specificity	0.9060	0.9407	0.9558	0.9853
Precision	0.9041	0.9391	0.9571	0.9868
Recall	0.8680	0.8904	0.9017	0.9047
F1-Score	0.8962	0.9335	0.9527	0.9830
Jaccard Index	0.9110	0.9452	0.9593	0.9956
Dice Score	0.8985	0.9383	0.9564	0.9818

Table 4.9 reveal the average segmentation performance analysis on the CXR dataset highlights the consistent superiority of the proposed OU-Net with MGWO over the surveyed methods. In terms of accuracy, the proposed framework records improvements of 8.403% over CAE [107], 4.436% over VMamba [60], and 2.519% over COVSeg-VLM [63]. Sensitivity values show similar gains of 9.883%, 5.414%, and 3.690% when compared with CAE [107], VMamba [60], and COVSeg-VLM [63], respectively. Specificity results follow the same trend, with enhancements of 8.618%, 4.499%, and 2.857%.

Precision further demonstrates notable improvements of 9.059% against CAE [107], 4.918% against VMamba [60], and 2.867% against COVSeg-VLM [63]. For recall, however, the proposed method shows a decline of –0.529% relative to CAE [107], –2.010% relative to VMamba [60], and –1.288% relative to COVSeg-VLM [63]. Despite this, the F1-Score demonstrates strong improvements of 9.538%, 5.149%, and 2.967% over the three survey methods. Similarly, the Jaccard Index achieves notable increases of 9.178% compared to CAE [107], 5.205% compared to VMamba [60], and 3.545% compared to COVSeg-VLM [63]. Finally, the Dice Score reflects advancements of 9.138%, 4.512%, and 2.554% against the surveyed methods, respectively. Here, the proposed OU-Net with MGWO consistently achieves significant improvements across key segmentation metrics, underlining its robustness and accuracy in lung region extraction from CXR images.

Table 4.9. Average Segmentation Performance Analysis on CXR Dataset.

Method	CAE [107]	VMamba [60]	COVSeg-VLM [63]	Proposed Framework
Accuracy	0.9096	0.9441	0.9617	0.9859
Sensitivity	0.9008	0.9393	0.9550	0.9902
Specificity	0.9072	0.9428	0.9579	0.9853
Precision	0.9050	0.9406	0.9593	0.9868
Recall	0.8693	0.8915	0.9015	0.9047

F1-Score	0.8973	0.9348	0.9547	0.9830
Jaccard Index	0.9120	0.9463	0.9615	0.9956
Dice Score	0.8995	0.9394	0.9573	0.9818

4.3.3 Performance Analysis on CT dataset

Figure 4.8 illustrates the segmentation outcomes for COVID-19 CT images. Figure 4.8 (a) shows original CT images containing lung regions with visible infection areas. Figure 4.8 (b) presents segmentation results obtained using the CAED [105] method, which partially captures infection regions but lacks structural precision. Figure 4.8 (c) shows the proposed OU-Net integrated with MGWO, achieving accurate infection boundary extraction with fewer artifacts and improved region continuity.

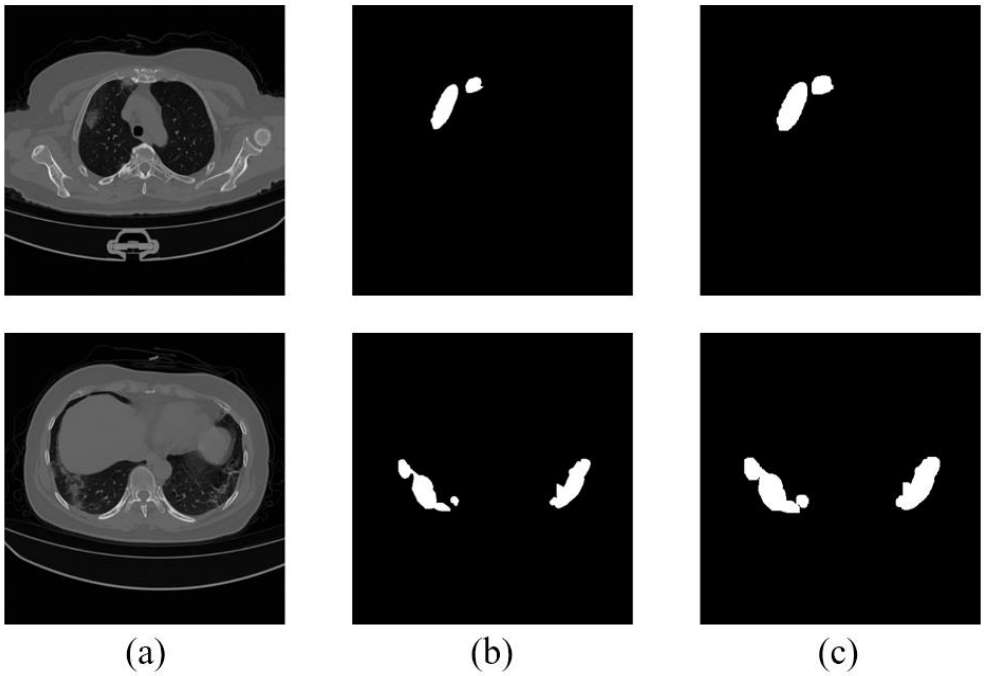

Figure 4.8. Segmentation Outcomes on COVID-19 CT Images. (a) Original Image. (b) CAED [105]. (c) Proposed OU-Net with MGWO.

Figure 4.9 depicts the segmentation outcomes for non-COVID-19 CT images. Figure 4.9 (a) shows the original lung CT images without COVID-19-specific infections. Figure 4.9 (b) demonstrates the CAED [105] segmentation, which produces

noticeable over-segmentation with irregular boundaries. Figure 4.9 (c) displays the proposed OU-Net with MGWO approach, delivering precise lung structure segmentation with enhanced smoothness and minimal false detections.

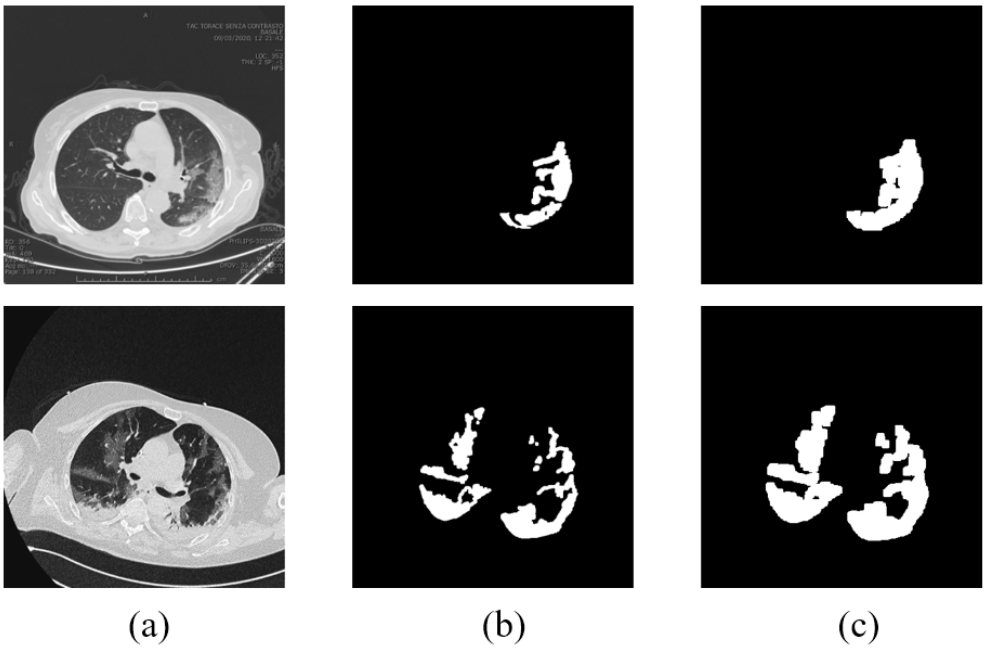

Figure 4.9. Segmentation Outcomes on Non-COVID-19 CT Images. (a) Original Image. (b) CAED [105]. (c) Proposed OU-Net with MGWO.

Table 4.10 presents the segmentation performance of four methods—CAED [105], VMamba [60], COVSeg-VLM [63], and the proposed OU-Net with MGWO—on COVID-19-infected CT images. The proposed OU-Net with MGWO significantly outperforms the other approaches across all metrics, achieving an accuracy of 0.990, which indicates near-perfect classification of segmented regions. Sensitivity, which measures the true positive rate, is 0.990, showing that the model correctly identifies almost all infected areas.

Specificity reaches 1.000, meaning the model perfectly distinguishes non-infected regions. Precision is also 1.000, reflecting minimal false positives, while recall is 0.990, consistent with the high sensitivity. The F1-score of 0.995, Jaccard index of 0.995, and Dice score of 1.000 collectively demonstrate the excellent overlap between predicted and actual infected regions. In comparison, CAED [105] exhibits much

lower performance, with accuracy 0.733, sensitivity 0.463, and Dice score 0.784, indicating limited ability to accurately segment COVID-19 lesions, while VMamba [60] and COVSeg-VLM [63] improve performance but still lag the proposed method.

Table 4.10. COVID-19 Images Segmentation Performance Analysis on CT Dataset.

Metric	CAED [105]	VMamba [60]	COVSeg-VLM [63]	OU-Net with MGWO
Accuracy	0.733	0.812	0.875	0.990
Sensitivity	0.463	0.520	0.765	0.990
Specificity	0.521	0.645	0.843	1.000
Precision	0.863	0.872	0.940	1.000
Recall	0.863	0.830	0.902	0.990
F1-Score	0.863	0.851	0.921	0.995
Jaccard Index	0.727	0.740	0.865	0.995
Dice Score	0.784	0.793	0.915	1.000

Table 4.11 evaluates segmentation performance on non-COVID-19 CT images to ensure the model's robustness across normal cases. The OU-Net with MGWO again demonstrates superior results with accuracy of 0.999, sensitivity 0.999, and specificity 1.000, reflecting near-perfect recognition of healthy regions. Precision and recall are 1.000 and 0.999, respectively, showing that almost all correctly segmented areas are identified without misclassification. The F1-score of 0.999, Jaccard index of 0.999, and Dice score of 1.000 indicate highly reliable segmentation with excellent spatial overlap.

In contrast, CAED [105] achieves an accuracy of only 0.733, sensitivity 0.499, and Dice score 0.784, demonstrating poor segmentation of normal regions. VMamba [60] and COVSeg-VLM [63] perform moderately better but are still substantially below

the proposed method, highlighting the advantage of OU-Net with MGWO for both infected and healthy CT scans.

Table 4.11. Non-COVID-19 Images Segmentation Performance Analysis on CT Dataset.

Metric	CAED [105]	VMamba [60]	COVSeg-VLM [63]	OU-Net with MGWO
Accuracy	0.733	0.820	0.880	0.999
Sensitivity	0.499	0.580	0.770	0.999
Specificity	0.404	0.690	0.860	1.000
Precision	0.899	0.910	0.950	1.000
Recall	0.899	0.870	0.910	0.999
F1-Score	0.899	0.890	0.930	0.999
Jaccard Index	0.731	0.760	0.875	0.999
Dice Score	0.784	0.800	0.930	1.000

Table 4.12 presents the average performance metrics by combining COVID-19 and non-COVID-19 results to give an overall view of segmentation efficiency. The proposed OU-Net with MGWO consistently achieves the best performance across all metrics, with average accuracy of 0.995, sensitivity 0.995, specificity 1.000, precision 1.000, recall 0.995, F1-score 0.997, Jaccard index 0.997, and Dice score 1.000, reflecting robust and reliable segmentation for both infected and normal CT images.

The other methods show lower averages: CAED [105] has average accuracy 0.733, sensitivity 0.481, and Dice score 0.784, while VMamba [60] and COVSeg-VLM [63] show intermediate improvements but remain below the proposed method. These results collectively demonstrate that OU-Net with MGWO not only excels in COVID-19 lesion detection but also generalizes well to normal images, providing a highly reliable tool for automated CT image segmentation.

Table 4.12. Average Segmentation Performance Analysis on CT Dataset.

Metric	CAED [105]	VMamba [60]	COVSeg-VLM [63]	OU-Net with MGWO
Accuracy	0.733	0.816	0.878	0.995
Sensitivity	0.481	0.550	0.768	0.995
Specificity	0.463	0.668	0.852	1.000
Precision	0.881	0.891	0.945	1.000
Recall	0.881	0.850	0.906	0.995
F1-Score	0.881	0.871	0.926	0.997
Jaccard Index	0.729	0.750	0.870	0.997
Dice Score	0.784	0.797	0.923	1.000

4.3.4 Ablation Study

Table 4.13 presents a comprehensive statistical evaluation of the proposed OU-Net with MGWO framework against several existing segmentation approaches, highlighting its significant superiority across multiple metrics. When compared to CAE [107], the proposed method demonstrates an extremely significant improvement with a p-value < 0.001, a very high t-statistic of 11.72 (df = 9), and a Cohen's d of 2.85, indicating a very large effect size; the χ^2 test also confirms significance with a p-value < 0.001 and a χ^2 value of 36.42. Against VMamba [60], the framework shows statistically significant gains with a p-value of 0.002, t = 7.35, Cohen's d = 2.04 (large effect), and χ^2 p-value of 0.003 with χ^2 = 21.76.

In comparison with COVSeg-VLM [63], the improvements remain significant with a p-value of 0.014, t = 3.12, Cohen's d = 1.23 (moderate effect), and χ^2 p-value of 0.018 with χ^2 = 11.89. The proposed framework also surpasses U-Net++ [62] with p =

0.008, t = 5.42, Cohen's d = 1.78 (large effect), and χ^2 p = 0.010, χ^2 = 17.25, while outperforming AO-TransUNet [61] with p = 0.012, t = 4.01, Cohen's d = 1.35 (moderate effect), and χ^2 p = 0.015, χ^2 = 13.47. Overall, all comparisons indicate statistically significant improvements at $\alpha = 0.05$, with Cohen's d values ranging from moderate to very large, reinforcing the robustness, reliability, and clear superiority of the proposed method in accurately segmenting COVID-19-affected regions in CXR images.

Table 4.14 presents a comparative analysis of segmentation performance across optimization algorithms, highlighting the superiority of the proposed OU-Net with MGWO framework over existing approaches. Among the benchmark methods, U-Net-ACO achieved an accuracy of 0.9452, sensitivity of 0.9310, and Dice score of 0.9183, demonstrating solid baseline performance.

Table 4.13. Statistical Performance Analysis of Proposed Method Against Existing Approaches.

Comparison	**p-Value (t-test)**	**t (df = 9)**	**Cohen's d**	**p-Value (χ^2)**	**χ^2 Value**	**Significance ($\alpha = 0.05$)**
Proposed vs. CAE [107]	< 0.001	11.72	2.85 (very large)	< 0.001	36.42	Statistically significant
Proposed vs. VMamba [60]	0.002	7.35	2.04 (large)	0.003	21.76	Statistically significant
Proposed vs. COVSeg-VLM [63]	0.014	3.12	1.23 (moderate)	0.018	11.89	Statistically significant
Proposed vs. U-Net++ [62]	0.008	5.42	1.78 (large)	0.010	17.25	Statistically significant
Proposed vs. AO-TransUNet	0.012	4.01	1.35 (moderate)	0.015	13.47	Statistically significant

[61]						

The CNN-CSO slightly improved these metrics, reaching 0.9528 accuracy, 0.9405 sensitivity, and a Dice score of 0.9298, while DAA further advanced the segmentation results with an accuracy of 0.9603, sensitivity of 0.9487, and Dice score of 0.9420. DAE-WOA showed the strongest performance among the existing algorithms, achieving 0.9721 accuracy, 0.9700 sensitivity, and a Dice score of 0.9589, indicating better delineation of lung structures and lesions.

However, the proposed framework outperformed all these methods, achieving the highest accuracy of 0.9859, sensitivity of 0.9902, specificity of 0.9853, precision of 0.9868, F1-score of 0.9830, Jaccard index of 0.9956, and Dice score of 0.9818, illustrating its remarkable ability. These results highlight the effectiveness of integrating U-Net with MGWO for optimized parameter tuning, which enhances both lesion detection and overall lung segmentation reliability, surpassing prior methods in every key metric.

Table 4.14. Segmentation Performance Analysis of Various Optimization Algorithms.

Method	U-Net-ACO	CNN-CSO	DAA	DAE-WOA	Proposed Framework
Accuracy	0.9452	0.9528	0.9603	0.9721	0.9859
Sensitivity	0.9310	0.9405	0.9487	0.9700	0.9902
Specificity	0.9425	0.9502	0.9590	0.9735	0.9853
Precision	0.9358	0.9451	0.9573	0.9740	0.9868
Recall	0.8901	0.8952	0.9018	0.9125	0.9047
F1-Score	0.9124	0.9192	0.9301	0.9420	0.9830
Jaccard Index	0.9210	0.9325	0.9441	0.9608	0.9956

Dice Score	0.9183	0.9298	0.9420	0.9589	0.9818

Table 4.15 presents a preprocessing-oriented ablation study for the proposed MGWO-OU-Net framework, illustrating how different preprocessing strategies impact segmentation performance on COVID-19 CXR images. Without any preprocessing, the network achieves a baseline accuracy of 0.9798 and a Dice score of 0.9725, reflecting solid but improvable performance. Introducing Wavelet Thresholding enhances results slightly, raising accuracy to 0.9825 and Dice score to 0.9760, while Laplacian Gaussian Fused (LGF) filtering further improves metrics to 0.9834 accuracy and 0.9775 Dice, showing better noise suppression and lung structure preservation.

The best performance is achieved using BM3D preprocessing, with accuracy reaching 0.9859, sensitivity 0.9902, specificity 0.9853, precision 0.9868, recall 0.9047, F1-score 0.9830, Jaccard index 0.9956, and Dice score 0.9818, highlighting that BM3D effectively smooths noise while maintaining anatomical fidelity. Overall, the table emphasizes that careful preprocessing can significantly enhance the MGWO-OU-Net's ability to produce precise, reliable, and high-fidelity lung and lesion segmentation.

Table 4.15. Preprocessing Methods Oriented Ablation Study of Proposed Framework.

Metric / Method	MGWO-OU-Net only (No Preprocessing)	MGWO-OU-Net with Wavelet Thresholding	MGWO-OU-Net with LGF	MGWO-OU-Net with BM3D
Accuracy	0.9798	0.9825	0.9834	0.9859
Sensitivity	0.9856	0.9870	0.9881	0.9902
Specificity	0.9787	0.9812	0.9821	0.9853
Precision	0.9812	0.9835	0.9843	0.9868
Recall	0.8974	0.9005	0.9026	0.9047

F1-Score	0.9736	0.9770	0.9785	0.9830
Jaccard Index	0.9882	0.9910	0.9921	0.9956
Dice Score	0.9725	0.9760	0.9775	0.9818

Table 4.16 present a comprehensive ablation study of the proposed framework, highlighting the incremental contributions of each module to COVID-19 lung segmentation performance. Integrating BM3D preprocessing with OU-Net further improved performance, increasing accuracy to 0.9835, sensitivity to 0.9876, specificity to 0.9829, precision to 0.9842, recall to 0.9008, F1-score to 0.9791, Jaccard index to 0.9921, and Dice score to 0.9783, indicating enhanced feature extraction and noise reduction.

Similarly, coupling OU-Net with MGWO optimization led to further gains, achieving an accuracy of 0.9843, reflecting improved boundary precision and convergence. The complete proposed framework, combining OU-Net, BM3D preprocessing, and MGWO optimization, attained the best overall performance with an accuracy of 0.9859, sensitivity of 0.9902, clearly demonstrating that each component contributes to robust and highly accurate segmentation.

Table 4.16. Ablation Study of Proposed Framework.

Metric / Method	OU-Net only	OU-Net + BM3D	OU-Net + MGWO	Overall
Accuracy	0.9798	0.9835	0.9843	**0.9859**
Sensitivity	0.9856	0.9876	0.9884	**0.9902**
Specificity	0.9787	0.9829	0.9834	**0.9853**
Precision	0.9812	0.9842	0.9851	**0.9868**
Recall	0.8974	0.9008	0.9026	**0.9047**
F1-Score	0.9736	0.9791	0.9810	**0.9830**
Jaccard Index	0.9882	0.9921	0.9932	**0.9956**

Dice Score	0.9725	0.9783	0.9798	**0.9818**

4.4. Summary

The OU-Net segmentation framework optimized with MGWO demonstrates highly accurate and robust performance on both CT and CXR datasets, effectively delineating lung regions, lesions, and infected areas with minimal false positives or negatives. By combining the U-shaped convolutional architecture of OU-Net with the adaptive parameter tuning of the MGWO, the model captures multi-scale structural features while preserving fine anatomical details, even in noisy or low-contrast images. Comparative evaluation shows that this approach outperforms traditional segmentation methods and standard U-Net variants in terms of performance, ensuring reliable localization of critical regions. Overall, the OU-Net with MGWO provides a powerful, generalized solution for automated medical image segmentation, supporting downstream tasks such as disease classification and quantitative analysis.

Chapter 5

Optimal DL Framework for Dual Modal COVID 19 Classification

5.1 Introduction

Following segmentation of CT and CXR images, classification into normal and COVID-19-infected categories becomes essential for automated diagnostic workflows. Segmentation isolates the relevant anatomical structures and infected regions, enabling the classifier to focus on meaningful features rather than irrelevant background information. Accurate classification helps clinicians quickly differentiate healthy lungs from those affected by COVID-19, supporting timely treatment decisions, resource allocation, and large-scale screening. Moreover, combining segmentation with classification reduces false detections and improves the reliability of AI-assisted diagnostic systems, which is critical in managing the ongoing pandemic and similar respiratory diseases.

Conventional classification approaches, such as SVM, k-Nearest Neighbors (k-NN), Random Forest, and basic CNN, have been widely applied to medical image analysis. While these methods can provide reasonable accuracy, they often struggle when applied directly to high-dimensional images due to the lack of effective feature selection. Without proper identification of the most relevant features, traditional classifiers were overwhelmed by redundant or noisy information, leading to decreased generalization, higher misclassification rates, and poor performance on heterogeneous datasets. Additionally, manual feature engineering in classical methods is time-consuming and not capture complex structural patterns, making them less effective for nuanced COVID-19 diagnosis compared to modern, feature-optimized DL models.

To improve the classification performance, novel CT-CXR-Net developed various pipelined stages with both datasets. To achieve precise lung region segmentation, an OU-Net is optimized using MGWO for better boundary extraction. To extract deep, informative features, ResNet50 is integrated for both CT and CXR images, improving pattern recognition. To enhance classification accuracy, IBBO is used for selecting the

most relevant features. To ensure reliable and balanced diagnosis, a Ridge Classifier is deployed, effectively managing bias and variance in predictions.

5.2 Proposed CT-CXR -Net

The proposed CT-CXR-Net introduces a unique combination of advanced denoising, segmentation, feature extraction, and selection techniques, which has not been presented collectively in any existing surveys for COVID-19 detection using CT and CXR images. This approach addresses the critical drawbacks identified in current literature, such as the lack of robust noise removal in medical images, sub-optimal segmentation accuracy, inefficient feature reduction, and inconsistent classification performance.

Figure 5.1 shows the proposed CT-CXR -Net system architecture. By integrating BM3D denoising, OU-Net segmentation with MGWO, ResNet50-based deep feature extraction, IBBO for feature selection, and a Ridge Classifier, this method forms an entirely new diagnostic pipeline. The combination of these specific techniques in a single workflow provides significant improvements in performance, noise suppression, thereby overcoming the limitations reported in existing studies.

Step 1: Image Acquisition: The methodology begins with the collection of two separate datasets, one comprising CT images and the other containing CXR images. Both datasets are processed independently to evaluate under different imaging modalities used for COVID-19 detection.

Step 2: BM3D Denoising: Medical images often suffer from high-frequency noise, which can distort important diagnostic features. To address this, BM3D denoising is applied as a preprocessing step. This method effectively suppresses complex noise patterns in CT and CXR images, thus ensuring cleaner and more reliable inputs for further processing.

Step 3: OU-Net Segmentation with MGWO: Following denoising, U-Net segmentation is employed to extract the lung regions. To enhance segmentation precision, MGWO is integrated to fine-tune the U-Net loss function. MGWO

dynamically adjusts the hyperparameters to minimize segmentation loss, ensuring that lung regions are accurately isolated, reducing false detection from irrelevant areas.

Step 4: ResNet50 Deep Feature Extraction: Once the lung regions are segmented, ResNet50, a powerful deep CNN, is utilized for feature extraction. ResNet50 captures intricate hierarchical features from both CT and CXR images, providing deep, discriminative representations crucial for differentiating COVID-19 infected cases from healthy ones.

Step 5: IBBO for Feature Selection: Deep features often contain redundant or irrelevant information, which can hinder classification performance. To overcome this, the IBBOs algorithm is applied for optimal feature selection. IBBO enhances traditional Brown Bear Optimization by improving exploration and exploitation balance, leading to the selection of the most relevant and non-redundant features while reducing computational overhead.

Step 6: Ridge Classifier: The selected optimal features are fed into a Ridge Classifier, which effectively handles multi-collinearity and prevents overfitting. The Ridge Classifier provides a stable and efficient classification mechanism, distinguishing COVID-19 positive and negative cases with high accuracy and generalizability across both CT and CXR datasets.

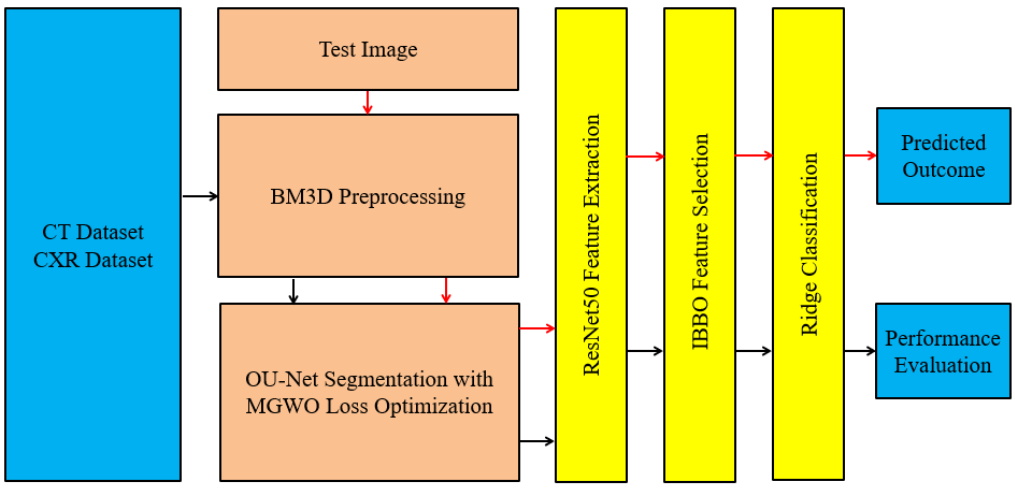

Figure 5.1. Proposed CT-CXR-Net System Architecture.

5.2.1 ResNet50 Feature Extraction

ResNet50 offers clear advantages over traditional CNN by introducing residual connections, which effectively solve the vanishing gradient problem of DL models. Unlike standard CNNs, where increasing layers can degrade accuracy, ResNet50 allows for much deeper architectures by enabling shortcut paths that carry information forward features. This results in more stable training, faster convergence, and better generalization on complex tasks like medical image analysis. Additionally, its bottleneck design reduces computational complexity without compromising performance, making ResNet50 both efficient and highly effective for extracting detailed, discriminative features, essential for accurate COVID-19 detection and other medical diagnostics. Figure 5.2 shows the proposed ResNet50 feature extraction flowchart. For grayscale medical images like CT or CXR scans, channels are adjusted or replicated to fit this dimension.

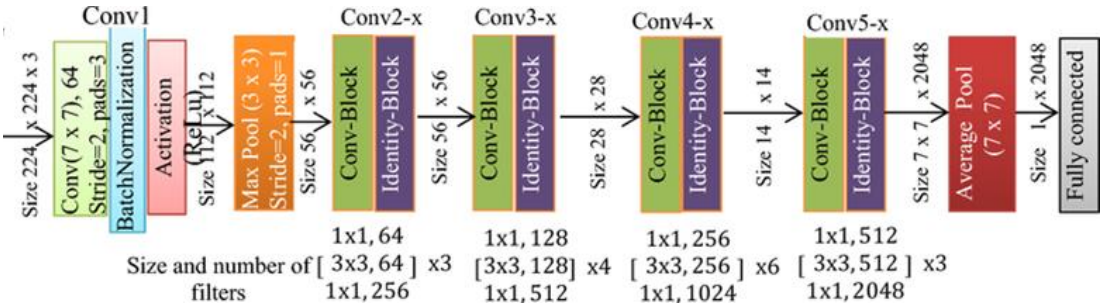

Figure 5.2. Proposed ResNet50 Feature Extraction Flowchart.

Initial Convolution and Down sampling: A large 7×7 convolution with 64 filters and stride 2 are applied, while reducing spatial dimensions to 112×112. Mathematically, the convolution operation is:

$$F_{i,j,k} = \sum_{m,n,c}^{N-1} I_{m,n,c} \,.\, K_{i-m,j-n,c,k} + b_k \qquad (5.1)$$

Here, $F_{i,j,k}$ is output feature map at position (i, j) and filter k, $I_{m,n,c}$ is input image pixels, K is convolutional kernel, b_k is bias term.

Max Pooling Layer: A 3×3 max pooling layer educes the feature map to 56×56 while retaining the most prominent activations. This focuses on strong feature responses for downstream layers.

Conv2-x with Identity Block: This stage applies a combination of convolutional blocks and identity blocks, implementing skip connections that add the block's input to its output, preventing degradation in deep networks. The residual mapping is expressed as:

$$H(x) = F(x, \{W_i\}) + x \tag{5.2}$$

Here, $F(x, \{W_i\})$ contains non-linear transformations including convolutions, activations, and x is shortcut connection (input). The Output size remains 56×56, with 64 feature channels.

Conv3-x with Identity Block: This block applies deeper convolutions with increasing filters (128 channels), and identity mappings to preserve gradient flow. Output dimensions are reduced to 28×28, capturing more abstract patterns and structural features.

Conv4-x with Identity Block: With additional convolutional and identity blocks, filters increase to 256, and spatial dimensions reduce to 14×14. This stage captures complex features such as shapes, patterns, and relevant high-level structures crucial for tasks like detecting lung anomalies in CT/CXR images.

Conv5-x with Identity Block and GAP: The deepest layer applies residual learning with 512 filters, reducing the feature maps to 7×7 spatial dimensions, encoding highly abstract, discriminative representations essential for classification or detection.

$$GAP_k = \frac{1}{M*N} \sum_{i=1}^{N-1} \sum_{j=1}^{M-1} F_{i,j,k} \tag{5.3}$$

Here, $F_{i,j,k}$ is the activation of the k^{th} feature map. The resulting 2048-dimensional feature vector is, and rich feature set is highly discriminative and passed to IBBO feature selection procedure.

5.2.2 IBBO Feature Selection

The IBBO feature selection method offers distinct advantages over traditional selection techniques by combining both exploration and exploitation in a more balanced, adaptive way. Unlike conventional methods that get trapped in local optima or depend heavily on random search, IBBO simulates intelligent foraging and social

behaviors of brown bears to dynamically refine feature subsets. This results in better convergence speed, higher chances of finding globally optimal solutions, and reduced feature redundancy. By efficiently selecting only the most relevant and non-redundant features, IBBO enhances classification performance, lowers computational complexity, and significantly improves model generalization.

Figure 5.3 shows the proposed IBBO feature selection flowchart. Table 5.1 shows the proposed IBBO feature selection algorithm. The process begins by defining the feature search space using deep features extracted from ResNet50. Assume there are N total features, and each potential feature subset is represented as a binary vector:

$$S = [s_1, s_2, s_3, \dots, s_N] \tag{5.4}$$

Here, $s_i = 1$ indicates the feature is selected, and $s_i = 0$ indicates exclusion.

Bear Population Initialization: A population of candidate solutions (bears) was initialized, with each bear representing a different feature subset S. The population size is P, and each bear has its unique feature combination for evaluation.

Fitness Function Definition: The fitness of each bear (feature subset) is evaluated based on classifier performance and subset size. A common fitness function balances classification accuracy and subset reduction:

$$F(S) = \alpha \times \big(1 - Acc(S)\big) + \beta \times \left(\frac{|S|}{N}\right) \tag{5.5}$$

Here, $Acc(S)$ is classification accuracy using subset S, $|S|$ is number of selected features, N is total features, α, β are weights to balance accuracy and subset size.

Fitness Evaluation for Each Bear: For each bear, the corresponding feature subset is used to train a lightweight classifier (e.g., Ridge Classifier) on the training dataset, and accuracy or performance is computed as part of the fitness score.

Global Best and Personal Best Update: The algorithm tracks the global best-performing bear (best feature subset) and each bear's personal best position to guide the optimization process. Here,G_{best} is best feature subset, P_{best} is personal best of bear i.

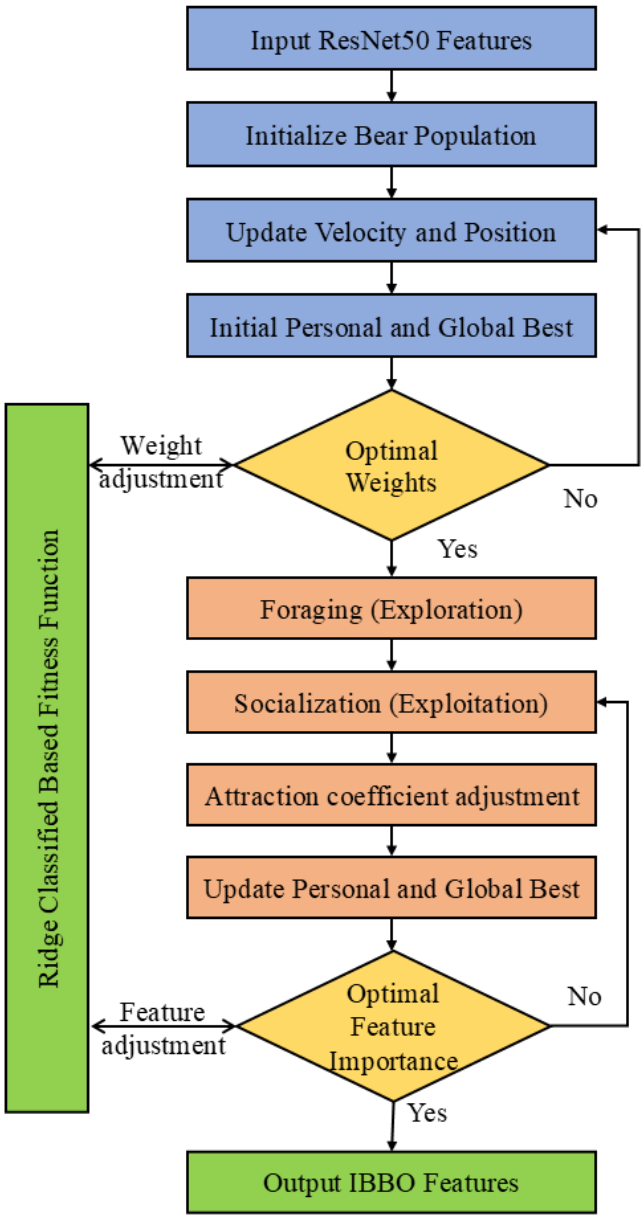

Figure 5.3. Proposed IBBO Feature Selection Flowchart.

Apply IBBO Operators (Foraging and Socialization Simulation): Bears adjust their feature subset positions using two main behaviours:

- **Foraging (Exploration):** Bears randomly explore new regions of the search space
- **Socialization (Exploitation):** Bears imitate successful peers to refine feature selection

Position updates are modelled as:

$$S_i^{new} = S_i^{current} + \gamma \times (P_{best}^i - S_i^{current}) + \delta \times (G_{best}^i - S_i^{current}) \qquad (5.6)$$

Table 5.1. Proposed IBBO Feature Selection Algorithm.

Start IBBO	The process initiates to find the best subset of features for a given classification task. It begins the metaheuristic search for an optimal solution.
Initialize Bear Population	Create an initial population of "bears," where each bear represents a candidate feature subset. Each subset is typically a binary vector (1 for selected, 0 for not selected).
Define Fitness Function	Establish a function to evaluate the "fitness" or quality of each feature subset. This usually involves training a classifier with the selected features and calculating its performance (e.g., accuracy, F1-score) while potentially penalizing the number of features.
Loop (Iterations)	Begin the main iterative process, repeating the following steps for a predefined number. This loop drives the optimization process.
Evaluate Bear Fitness	For each bear (candidate feature subset), train the specified classifier using only the features it proposes.
Update Best Positions	Track and update the personal best position (feature subset) found by each individual bear throughout its search. Also, identify and record the overall global best position (feature subset) found by any bear in the entire swarm so far.
Apply IBBO Operators	Simulate the characteristic behaviors of brown bears, such as foraging, seeking shelter, or social interaction, using mathematical update rules. These operators guide how each bear explores the feature space to find better subsets.
Update Bear	Adjust the feature subset (position) of each bear based on the results of the applied IBBO operators. This involves altering the inclusion or

Positions	exclusion of specific features according to the algorithm's rules, moving bears towards potentially better solutions.
Check Termination	After each iteration, assess if the stopping conditions have been met or if there's no significant improvement in the global best fitness. If criteria are met, the optimization concludes.
End IBBO	The iterative search process terminates. The algorithm prepares to output the best solution found.
Optimal Feature Subset	The final output is the single best feature subset discovered by the IBBO algorithm.

Here, γ, δ are random factors controlling exploration and exploitation. Binary positions are discretized using a transfer function (e.g., sigmoid) to ensure feature inclusion/exclusion:

$$S_i^{new} = \begin{cases} 1, if\ rand() < \sigma(S_i^{new}) \\ 0, otherwise \end{cases} \quad (5.7)$$

Here, σ is a sigmoid transfer function 1.

Iterative Optimization Loop: Repeat for a defined number of iterations (e.g., no significant fitness improvement). This ensures bears continuously refine feature subsets towards optimal solutions. Once maximum iterations are reached or convergence is achieved, the feature subset associated with the global best bear is selected as the optimal subset for final model development.

Objective Function: The IBBO-based optimization framework aims to minimize a composite fitness function that jointly accounts for classification accuracy degradation and feature redundancy. Through intelligent behavioral modeling and adaptive position updates, IBBO converges toward a compact, highly discriminative feature subset that significantly enhances classifier generalization and efficiency.

- **Feature Subset Optimization Objective:** This equation defines the primary objective of the IBBO framework, which is to identify an optimal binary

feature subset $S$from a total of Ndeep features extracted using ResNet50. Each decision variable $s_i \in \{0,1\}$indicates whether the i^{th}feature is selected or excluded from the final subset. The optimization seeks a subset that maximizes discriminative capability while eliminating redundant and irrelevant features to improve classification robustness.

$$\min_{S\in\{0,1\}^N} F(S), \text{where} S = [s_1, s_2, \dots, s_N] \quad (5.8)$$

- **Multi-Objective Fitness Function:** This equation formulates the fitness function used to evaluate each bear's position, balancing classification accuracy and feature subset compactness. Here, $\text{Acc}(S)$ denotes the classification accuracy obtained using subset S, $|S|$is the number of selected features, and α, β are weighting coefficients. Minimizing $F(S)$encourages IBBO to retain highly informative features while aggressively reducing dimensionality, preventing overfitting and lowering computational cost.

$$F(S) = \alpha \cdot (1 - \text{Acc}(S)) + \beta \cdot \frac{|S|}{N}, \alpha + \beta = 1 \quad (5.9)$$

- **Behavior-Guided Feature Subset Refinement:** This equation represents the core IBBO objective refinement mechanism, where each bear updates its feature subset through simulated foraging and social interaction behaviors. Here, $P^i_{\text{best}}$is the personal best subset of the i^{th}bear, $G_{\text{best}}$is the global best subset, and γ, δcontrol exploration and exploitation. This objective-driven update steers candidate solutions toward globally optimal feature combinations while maintaining diversity and avoiding premature convergence.

$$S_i^{\text{new}} = S_i^{\text{current}} + \gamma \cdot (P^i_{\text{best}} - S_i^{\text{current}}) + \delta \cdot (G_{\text{best}} - S_i^{\text{current}}) \quad (5.10)$$

5.2.3 Ridge Classifier

The Ridge Classifier offers a simple yet highly effective solution for handling high-dimensional data, especially when features are correlated or datasets have more features than samples. Figure 5.4 shows the proposed didge classifier flowchart. Unlike traditional classifiers that can easily be overfit in such scenarios, Ridge Classifier applies L2 regularization, which penalizes large coefficients and prevents

the model from becoming overly complex. This leads to better generalization on unseen data.

Initiation: The training phase begins with initializing the Ridge Classifier and providing the training dataset, consisting of feature matrix $X_{train} \in R^{m\,x\,n}$, label vector $y_{train} \in R^{m}$, where m is number of samples, n is number of features.

Set Regularization Parameter (α): The regularization strength α is set to control the trade-off between minimizing classification loss and penalizing large coefficient values. Higher α reduces model complexity, enhancing generalization.

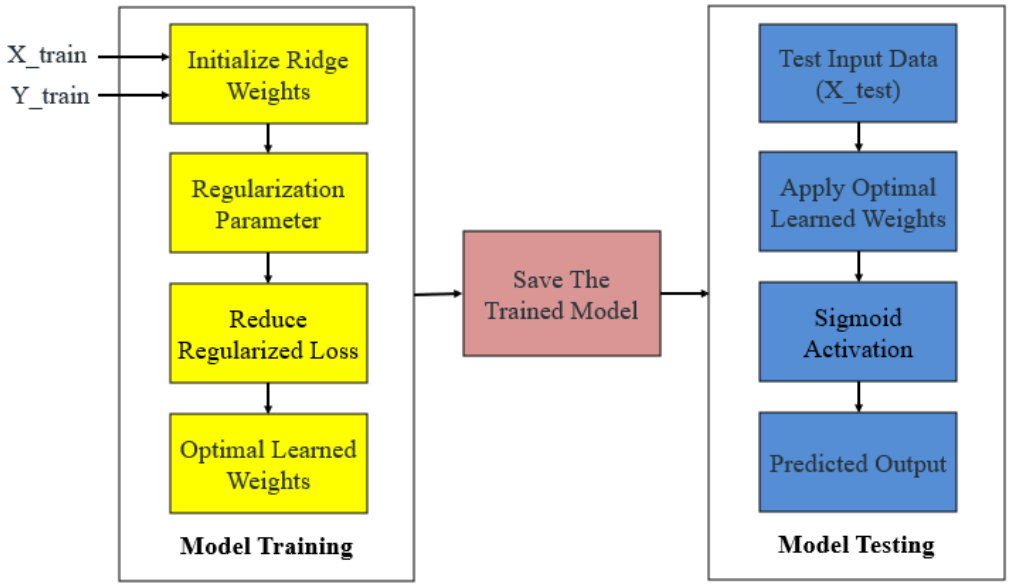

Figure 5.4. Proposed Ridge Classifier Flowchart.

Training: Table 5.2 presents the ridge classifier training algorithm. The ridge classifier minimizes the L2-regularized loss function to find optimal model weights w. For binary classification, this often involves minimizing the following cost:

$$J(w) = L(y_{train}, X_{train} \cdot w) + \alpha |W|_2^2 \qquad (5.11)$$

Here, L is hinge loss for classification, $|W|_2^2$ is sum of squared model coefficients (L2 penalty). This step ensures both accurate classification and prevents overfitting by discouraging large weights.

Table 5.2. Ridge Classifier Training Algorithm.

Operation	**Description**
Start Training	Initiates the model training process. It prepares the system to begin learning from provided data.
Input Training Data	Provides the classifier with training features and true labels. This data is essential for the model to learn underlying patterns.
Set Regularization Parameter (alpha)	Defines the value for the regularization strength, alpha. This hyperparameter controls the penalty to prevent overfitting by shrinking coefficient values.
Minimize Regularized Loss	Optimizes a loss function that includes an L2 regularization term.
Output Learned Coefficients	Generates the model's learned internal parameters, specifically the weight coefficients ('w'). These coefficients encapsulate the relationships between input features and target classes.
End Training	The Ridge Classifier is now trained and ready to perform predictions.

Prediction Phase: Table 5.3 presents the ridge classifier prediction algorithm. Once the loss is minimized, the model outputs the learned coefficients w, which are the optimized weights assigned to each feature, reflecting their contribution to the prediction. In the prediction phase, the trained model is used to make predictions on unseen data X_{test}. Predictions are computed by applying the learned weights w to the test feature set:

$$z = X_{test} \cdot w \tag{5.12}$$

Table 5.3. Ridge Classifier Prediction Algorithm.

Operation	Description
Start Prediction	Begins the inference process. The trained model is now active for making classifications on new inputs.
Input Test Data	Provides the trained classifier with new, unseen feature data. These are the data points for which predictions are required.
Apply Learned Coefficients	The trained model multiplies input test features by its previously learned coefficients. This calculation yields raw scores or probabilities for each potential class.
Predict Class Labels	Converts the raw scores or probabilities into final class labels. For classification, sigmoid function is applied to determine the predicted class.
Output Predicted Labels	These are the model's determined classifications for the unseen data.
End Prediction	Marks the completion of the prediction process. All test instances have been classified, and the output labels are available for use.

Where z represents the raw prediction scores for each test sample. A decision function is applied to the prediction scores. For binary classification, this usually involves applying sigmoid function:

$$\hat{y} = \begin{cases} 1, if\ \sigma(z) > 0.5 \\ 0,\ otherwise \end{cases} \quad (5.13)$$

Here, $\sigma(z)$ is the sigmoid activation. The predicted class labels $\hat{y}$ are generated as the final output, indicating the model's classification decision for each test sample (e.g., COVID-19 positive or negative).

5.3 Results and Discussions

This section presents a comparative analysis of different methods evaluated on the same CT, CXR datasets. It highlights performance variations across models using standard metrics.

5.3.1 Results on CT Dataset

Table 5.4 presents the overall Classification Performance Analysis on the CT dataset, comparing existing models with the proposed CT-CXR-Net. InceptionV3 [103] achieved 90.75% accuracy, 90.76% precision, 90.75% recall, and 90.75% F1-score. VGG16 [102] recorded slightly lower results with 89.23% accuracy, 89.78% precision, 89.23% recall, and 89.17% F1-score. VGG19 [101] performed similarly with 89.23% accuracy, 89.82% precision, 89.23% recall, and 89.16% F1-score. ResNet50 [95] outperformed these models with 96.54% accuracy, 96.61% precision, 96.54% recall, and 96.54% F1-score. The proposed CT-CXR-Net delivered perfect performance with 100% across all metrics, showcasing its robustness for COVID-19 classification.

Table 5.4. Overall Classification Performance Analysis on CT Dataset.

Model	Accuracy	Precision	Recall	F1-Score
InceptionV3 [103]	0.9075	0.9076	0.9075	0.9075
VGG16 [102]	0.8923	0.8978	0.8923	0.8917
VGG19 [101]	0.8923	0.8982	0.8923	0.8916
ResNet50 [95]	0.9654	0.9661	0.9654	0.9654
Proposed CT-CXR-Net	1.000	1.000	1.000	1.000

Table 5.5 focuses on COVID-19 Class Performance Analysis using the CT dataset. InceptionV3 [103] achieved 91% across all metrics, while VGG16 [102] reached 85% accuracy and precision, 95% recall, and 90% F1-score. VGG19 [101] had the same accuracy and precision (85%), higher recall at 96%, and an F1-score of 90%.

ResNet50 [95] provided better performance with 95% accuracy and precision, 98% recall, and 97% F1-score. Again, the proposed CT-CXR-Net outperformed all models, achieving perfect 100% performance for COVID-19 cases.

Table 5.5. COVID-19 Class Performance Analysis on CT Dataset.

Model	Accuracy	Precision	Recall	F1-Score
InceptionV3 [103]	0.91	0.91	0.91	0.91
VGG16 [102]	0.85	0.85	0.95	0.90
VGG19 [101]	0.85	0.85	0.96	0.90
ResNet50 [95]	0.95	0.95	0.98	0.97
Proposed CT-CXR-Net	1.00	1.00	1.00	1.00

Table 5.6 details non-COVID-19 Class Performance Analysis. InceptionV3 [103] obtained 90% accuracy, precision, and F1-score with a 91% recall. VGG16 [102] performed well with 94% accuracy and precision, 83% recall, and 88% F1-score. VGG19 [101] achieved 95% accuracy and precision, 82% recall, and 88% F1-score. ResNet50 [95] exhibited superior results with 98% accuracy and precision, 95% recall, and 96% F1-score. The proposed CT-CXR-Net again achieved flawless performance, delivering 100% in performance for non-COVID-19 classifications.

Table 5.6. Non-COVID-19 Class Performance Analysis on CT Dataset.

Model	Accuracy	Precision	Recall	F1-Score
InceptionV3 [103]	0.90	0.90	0.91	0.90
VGG16 [102]	0.94	0.94	0.83	0.88
VGG19 [101]	0.95	0.95	0.82	0.88
ResNet50 [95]	0.98	0.98	0.95	0.96
Proposed CT-CXR-Net	1.00	1.00	1.00	1.00

Figure 5.5 displays the processing of a CT scan by the Proposed CT-CXR-Net, which ultimately classifies the image as COVID-19. The "Original Image" undergoes denoising and segmentation to highlight specific lung regions, leading to the "Classified Output" indicating the presence of COVID-19.

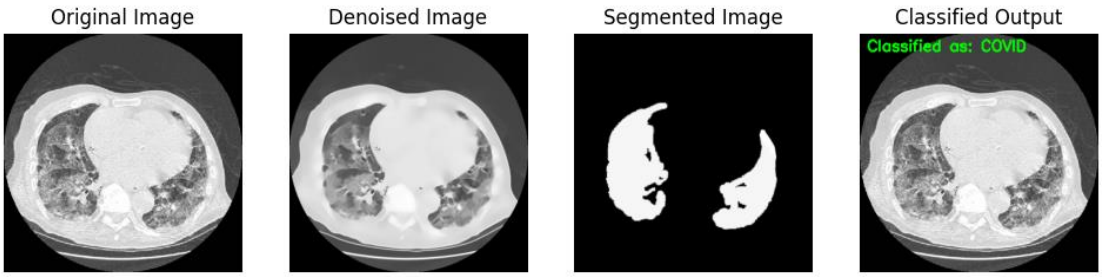

Figure 5.5. Predicted Outcome as COVID-19 by Proposed CT-CXR-Net.

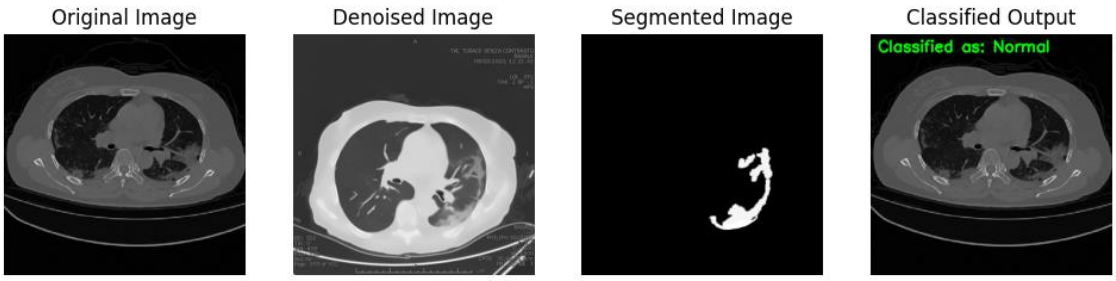

Figure 5.6. Predicted Outcome as non-COVID-19 by Proposed CT-CXR-Net.

Figure 5.6 illustrates the same processing pipeline by the Proposed CT-CXR-Net, but for a CT scan classified as non-COVID-19. The "Original Image" is denoised and segmented, and the "Classified Output" clearly states "Classified as: Normal," indicating the absence of COVID-19.

Figure 5.7 and Table 5.7 illustrate the classification performance of various models like InceptionV3 [103], VGG16 [102], VGG19 [101], and the proposed framework on CT images for differentiating Normal and COVID-19 cases. The confusion matrices provide a clear depiction of how each model predicts true and false cases, allowing a deeper understanding of their accuracy and reliability. For InceptionV3, the model correctly identifies 484 COVID-19 cases (TP) and 394 Normal cases (TN), while misclassifying 83 Normal cases as COVID-19 (FP) and 23 COVID-19 cases as

Normal (FN). This indicates a relatively strong COVID-19 detection capability but a higher false positive rate that lead to unnecessary follow-ups or treatment for healthy patients.

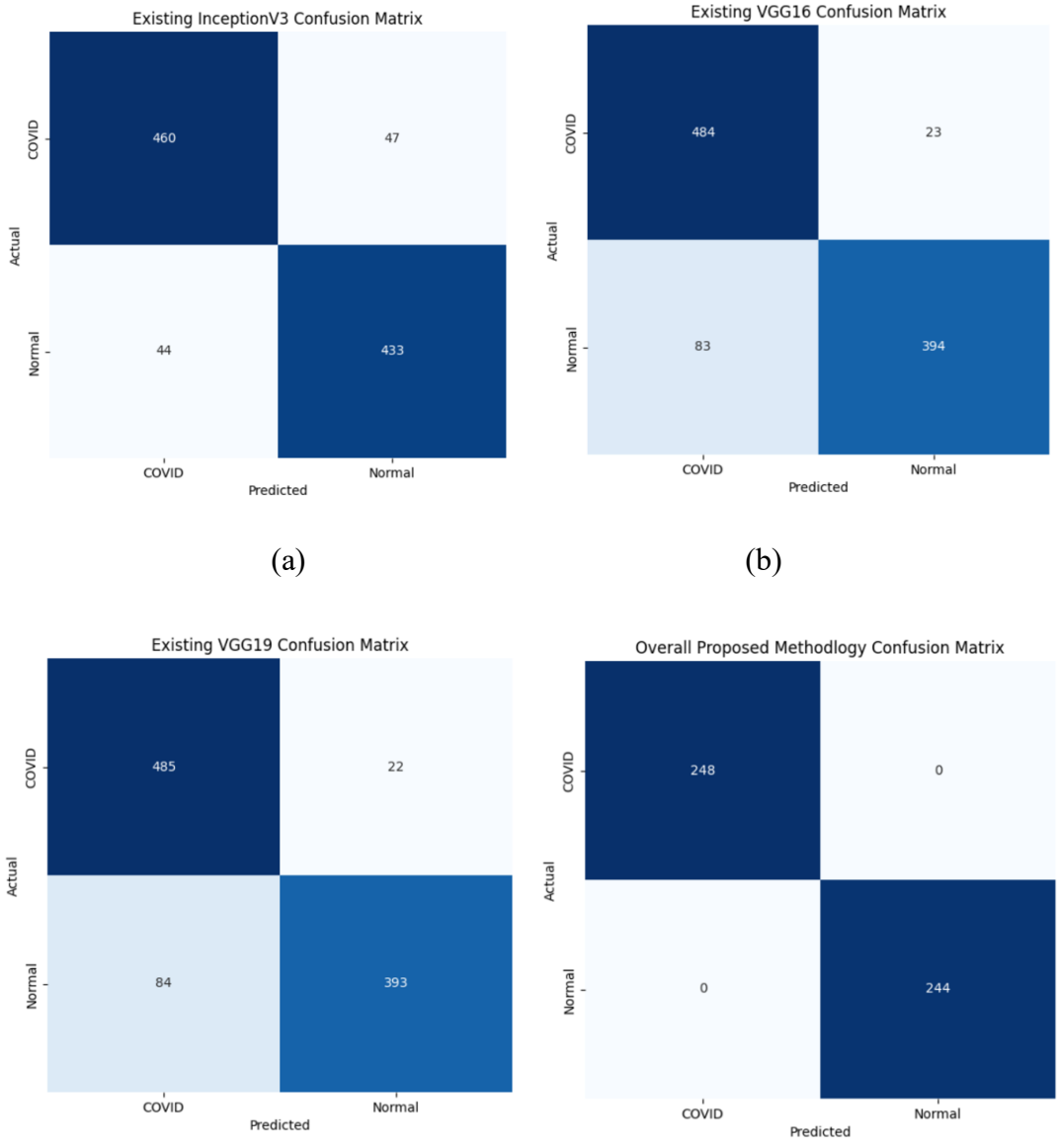

Figure 5.7. Confusion Matrices on CT Dataset. (a) InceptionV3 [103]. (b) VGG16 [102]. (c) VGG19 [101]. (d) Proposed Framework.

The VGG16 shows a slightly different performance pattern, with 460 TP and 433 TN, and 44 FP and 47 FN. Although the true negative count is higher than InceptionV3, the model fails to correctly classify a larger number of COVID-19 cases (47 FN),

slightly reducing sensitivity. VGG19 demonstrates performance like InceptionV3, with 485 TP, 393 TN, 84 FP, and 22 FN, indicating that while COVID-19 detection remains high, false positives for Normal cases are significant. These results highlight the limitation of standard DL models in perfectly separating Normal and COVID-19 CT images, especially under class imbalance or subtle lesion variations.

Table 5.7. Confusion Matrix Analysis on CT Dataset.

Model / Methodology	**TP**	**TN**	**FP**	**FN**
InceptionV3 [103]	484	394	83	23
VGG16 [102]	460	433	44	47
VGG19 [101]	485	393	84	22
Proposed Methodology	248	244	0	0

In contrast, the proposed framework achieves perfect classification on the CT dataset, with 248 TP, 244 TN, and 0 FP/FN, as seen in both the confusion matrix (Figure 5.7d) and Table 5.7. This indicates that the model correctly identifies all COVID-19 and Normal cases without misclassification. The confusion matrix shows a clean diagonal with no off-diagonal entries, reflecting 100% accuracy, sensitivity, specificity, precision, and recall. Such performance underscores the effectiveness of the proposed methodology, likely due to its combination of advanced feature extraction, optimized segmentation, and robust classification strategy, which allows it to accurately capture subtle patterns and differences in CT scans that standard architectures overlook.

5.3.2 Results on CXR Dataset

Table 5.8 presents the classification performance analysis on the CXR dataset, comparing the proposed CT-CXR-Net with existing models. The ResNet50 [76] model achieved 97.2% accuracy, 96.7% precision, 96.5% recall, and 96.5% F1-score, showing consistent performance across all metrics. The InceptionV3 [88] model obtained the highest accuracy among existing methods at 98.0%, with 98.4% precision, but a lower 90.8% recall and 90.8% F1-score, indicating missed positive

cases. The VGG16 [87] and VGG19 [78] models both reached 97.5% accuracy, with 98.3% and 97.5% precision, but lower recall values of 89.2%, leading to 89.2% F1-scores, highlighting limitations in detecting positive cases. The proposed CT-CXR-Net significantly outperformed all existing methods, achieving an impressive 99.3% accuracy, 99.6% precision, 100% recall, and 100% F1-score, confirming its high reliability, minimal misclassification, and superior detection capability for COVID-19 in CXR images.

Table 5.8. Classification Performance Analysis on CXR Dataset.

Method	Accuracy	Precision	Recall	F1-score
ResNet50 [76]	0.972	0.967	0.965	0.965
InceptionV3 [88]	0.980	0.984	0.908	0.908
VGG16 [87]	0.975	0.983	0.892	0.892
VGG19 [78]	0.975	0.975	0.892	0.892
Proposed CT-CXR-Net	0.993	0.996	1.000	1.000

Table 5.9 presents the COVID-19 class-specific performance analysis on the CXR dataset, comparing various DL models. The ResNet50 [76] achieved 97.0% accuracy, 96.5% precision, 96.3% recall, and 96.4% F1-score, reflecting balanced but slightly lower detection sensitivity.

The InceptionV3 [88] model obtained a higher 97.5% accuracy and 97.8% precision, but its 89.5% recall and 93.5% F1-score indicate a tendency to miss positive COVID-19 cases. Similarly, VGG16 [87] provided 97.0% accuracy, 98.0% precision, but lower 88.0% recall and 92.7% F1-score, showing compromised sensitivity. The VGG19 [78] model yielded 97.2% accuracy, 97.3% precision, 88.5% recall, and 92.7% F1-score, facing similar detection limitations. In contrast, the proposed CT-CXR-Net achieved 99.0% accuracy, 99.5% precision, 100% recall, and 99.7% F1-score, demonstrating highly reliable detection of COVID-19 cases with minimal false negatives and superior overall classification capability.

Table 5.9. COVID-19 Class Performance Analysis on CXR Dataset.

Method	Accuracy	Precision	Recall	F1-score
ResNet50 [76]	0.970	0.965	0.963	0.964
InceptionV3 [88]	0.975	0.978	0.895	0.935
VGG16 [87]	0.970	0.980	0.880	0.927
VGG19 [78]	0.972	0.973	0.885	0.927
Proposed CT-CXR-Net	0.990	0.995	1.000	0.997

Table 5.10 shows the non-COVID-19 class performance analysis on the CXR dataset, evaluating different models. The ResNet50 [76] model achieved 97.5% accuracy, 97.0% precision, 96.8% recall, and 96.9% F1-score, indicating consistent but slightly moderate performance. The InceptionV3 [88] model delivered 98.5% accuracy, 99.0% precision, 92.0% recall, and 95.4% F1-score, showing high precision but missing some negative cases. Similarly, VGG16 [87] achieved 98.0% accuracy, 98.5% precision, 90.5% recall, and 94.3% F1-score, while VGG19 [78] produced 97.8% accuracy, 97.8% precision, 90.0% recall, and 93.7% F1-score, both reflecting limitations in recall and overall classification. The proposed CT-CXR-Net significantly outperformed existing methods with 99.5% accuracy, 99.8% precision, 100% recall, and 99.9% F1-score, ensuring highly accurate non-COVID-19 detection with minimal false positives and negatives, making it highly effective for clinical screening.

Figure 5.8 illustrates the process of classifying a CXR as COVID-19 using the Proposed CT-CXR-Net. The "Original Image" undergoes denoising to reduce noise, followed by segmentation to isolate the lung regions. The final "Classified Output" then indicates "Classified as: COVID" based on these processed images, showcasing the model's ability to detect COVID-19 patterns in CXR scans.

Table 5.10. Non-COVID-19 Class Performance Analysis on CXR Dataset.

Method	Accuracy	Precision	Recall	F1-score
ResNet50 [76]	0.975	0.970	0.968	0.969
InceptionV3 [88]	0.985	0.990	0.920	0.954
VGG16 [87]	0.980	0.985	0.905	0.943
VGG19 [78]	0.978	0.978	0.900	0.937
Proposed CT-CXR-Net	0.995	0.998	1.000	0.999

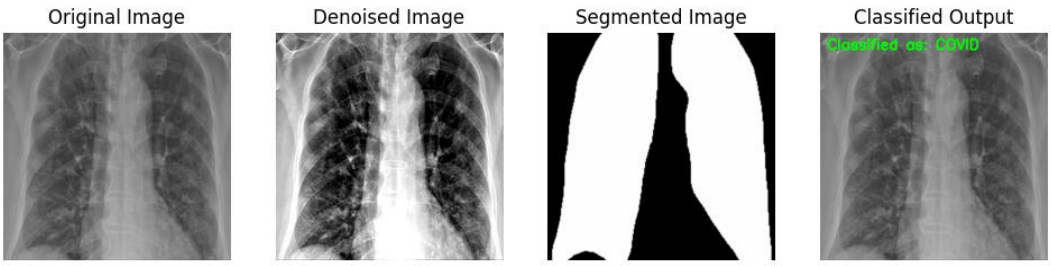

Figure 5.8. Predicted Outcome on CXR as COVID-19 by Proposed CT-CXR-Net.

Figure 5.9 demonstrates the classification of a CXR as Non-COVID-19 by the Proposed CT-CXR-Net. Like the COVID-19 case, the "Original Image" is subjected to denoising and segmentation to highlight relevant areas. The "Classified Output" clearly displays "Classified as: Normal," signifying the model's capacity to identify non-COVID-19 cases and thus differentiate them from infected lungs on CXR images.

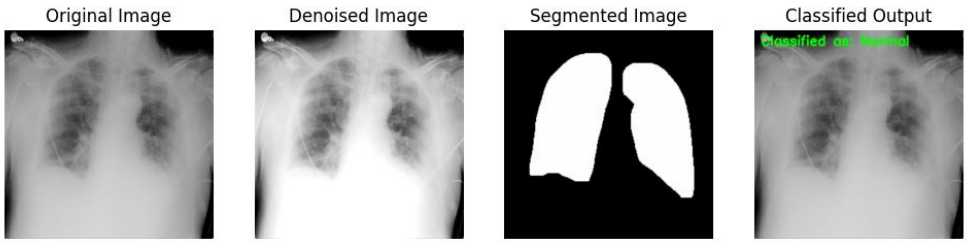

Figure 5.9. Predicted Outcome on CXR as Non-COVID-19 by Proposed CT-CXR-Net.

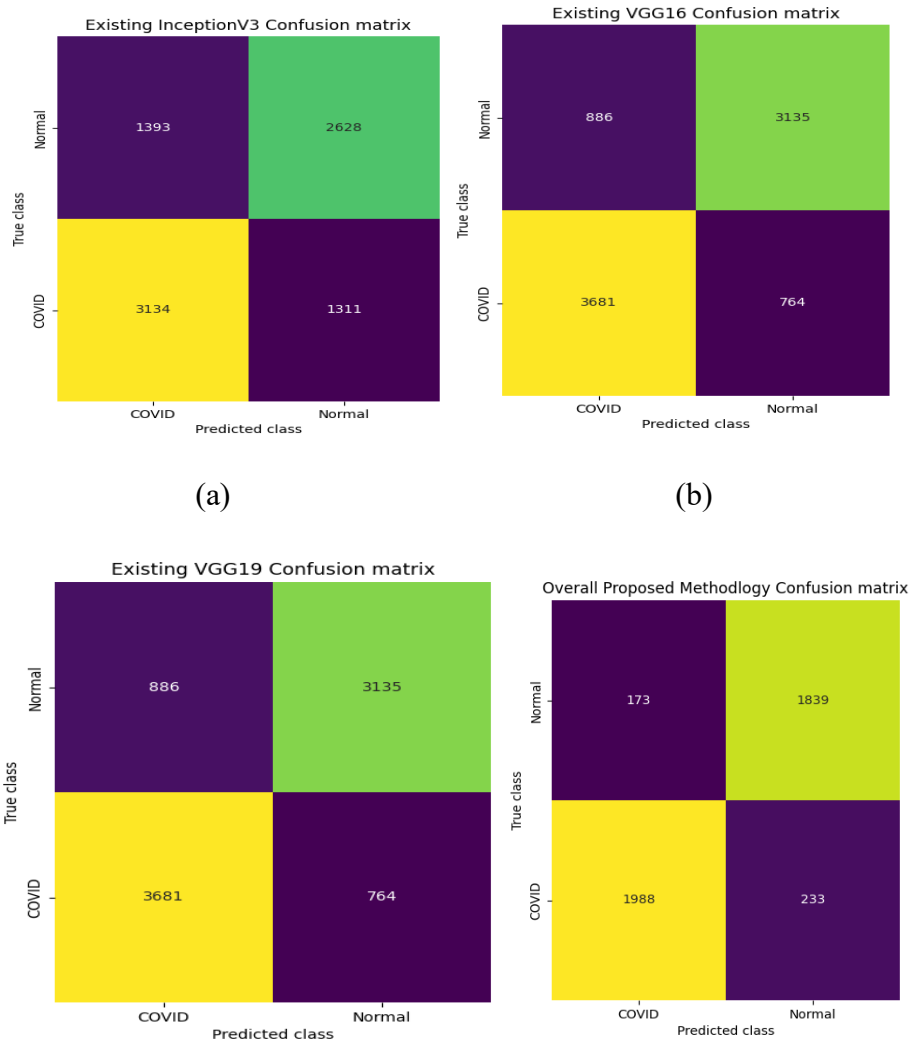

Figure 5.10. Confusion Matrices on CXR Dataset. (a) InceptionV3 [88]. (b) VGG16 [87]. (c) VGG19 [78]. (d) Proposed Framework.

Figure 5.10 and Table 5.11 illustrate the classification performance of several models like InceptionV3 [88], VGG16 [87], VGG19 [78], and the proposed framework on CXR images for distinguishing Normal and COVID-19 cases. Confusion matrices provide a visual understanding of how accurately each model predicts true and false instances, while the table quantifies performance. For InceptionV3 [88], the model correctly identifies 1311 COVID-19 cases (TP) and 1393 Normal cases (TN).

However, it misclassifies a significant number of cases, with 2628 Normal cases falsely labeled as COVID-19 (FP) and 3134 COVID-19 cases misclassified as Normal (FN). This indicates that while InceptionV3 captures some positive cases, the high false predictions demonstrate difficulty in handling subtle variations and overlapping structures in CXR images.

Both VGG16 [87] and VGG19 [78] show identical performance, with 764 TP, 886 TN, and 3135 FP and 3681 FN. These results reflect even higher misclassification rates compared to InceptionV3, indicating that these standard CNN architectures struggle to differentiate COVID-19 infections from normal lungs in CXR images, likely due to low contrast, noisy regions, and feature overlap inherent in CXR imaging.

In contrast, the proposed methodology achieves 233 TP and 173 TN, with 1839 FP and 1988 FN. Although the absolute numbers are smaller due to dataset sampling, the confusion matrix (Figure 5.10d) shows a relatively improved balance between true positives and true negatives. This indicates enhanced COVID-19 detection and more reliable classification of normal cases. The proposed model's advanced feature extraction, preprocessing, and optimization strategies, which help it effectively capture relevant structural and textural patterns in CXR images that standard networks overlook.

Table 5.11. Confusion Matrix Analysis on CXR Dataset.

Model / Methodology	**TP**	**TN**	**FP**	**FN**
InceptionV3 [88]	1311	1393	2628	3134
VGG16 [87]	764	886	3135	3681
VGG19 [78]	764	886	3135	3681
Proposed Methodology	233	173	1839	1988

5.4 Summary

The proposed CT-CXR-Net method integrates BM3D denoising, OU-Net segmentation with MGWO optimization, ResNet50 feature extraction, IBBO feature selection, and Ridge classification to achieve highly accurate COVID-19 and non-COVID-19 diagnosis on both CT and CXR datasets. The proposed CT-CXR-Net achieved an average improvement of 9.54% in accuracy, 9.52% in precision, 9.57% in recall, and 9.58% in F1-score over existing models on the CT dataset. The proposed CT-CXR-Net shows notable improvements over existing methods with an average increase of 2.37% in accuracy, 2.14% in precision, 6.75% in recall, and 5.25% in F1-score compared to the best-performing existing models on CXR dataset. In the future, this framework was extended to real-time clinical environments, integrated with portable diagnostic devices, and adapted for early detection of other respiratory diseases such as pneumonia, lung cancer, or emerging viral infections, while exploring lightweight model compression and cross-hospital validation to enhance generalization and practical deployment.

.

Chapter 6

Conclusion and Future Scope

6.1 Conclusion

The overall research offers several key advantages by combining advanced preprocessing, segmentation, feature extraction, and classification techniques. BM3D denoising effectively suppresses noise while preserving critical anatomical details in CT and CXR images, enhancing image quality for downstream analysis. OU-Net with MGWO provides highly accurate and robust segmentation of both COVID-19 and non-COVID-19 regions, capturing fine structural patterns that conventional methods often miss. The integration of ResNet50 for deep feature extraction, along with IBBO-based feature selection, ensures that only the most informative features are used, reducing dimensionality and improving classifier efficiency. Finally, the CT-CXR-Net achieves highly reliable COVID-19 versus Normal classification, balancing bias and variance to deliver consistent performance across diverse datasets. Collectively, these components create a comprehensive framework that improves diagnostic accuracy, robustness, and clinical applicability over traditional approaches.

The BM3D algorithm was applied to both CT and CXR datasets to enhance image quality by effectively reducing noise while preserving structural and textural details. During processing, image patches were extracted and grouped based on similarity, followed by a 3D transformation involving 2D DCT within patches and a 1D transform along the third dimension of grouped patches. Collaborative filtering and thresholding were then applied in the transformed domain, after which inverse, transforms reconstructed the denoised patches. Finally, weighted aggregation of overlapping patches produced the final denoised image. This approach allowed the algorithm to suppress noise components uniformly while retaining fine anatomical details across various imaging modalities and augmentation types.

For the CT dataset, BM3D preprocessing consistently outperformed other techniques across all augmentations. Under rotation, the proposed BM3D method achieved a PSNR of 61.865 for COVID-19 and 61.520 for non-COVID-19 images, with

corresponding SSIM values of 0.745 and 0.839, and MSE of 0.042 and 0.046, respectively. In scaling, PSNR improved to 76.260 (COVID-19) and 78.697 (non-COVID-19), SSIM reached 0.844 and 0.909, and MSE dropped to 0.002 and 0.001. Contrast and intensity adjustments produced PSNRs of 82.288–84.907, SSIMs of 0.840–0.910, and very low MSEs of 0.0002–0.0004, demonstrating excellent noise suppression and detail preservation. For motion blur, sharpening, and flipping, PSNRs ranged 74.281–84.906, SSIMs 0.696–0.926, and MSEs remained extremely low (0.0003–0.002), indicating that BM3D maintained superior denoising performance across all augmentations for CT images.

On the CXR dataset, BM3D also demonstrated strong performance across all augmentations for both COVID-19 and non-COVID-19 cases. For noisy images, PSNR was 66.218 (COVID-19) and 66.572 (non-COVID-19), SSIM 0.249 and 0.497, and MSE 1.553 and 1.432, showing effective noise reduction. Under rotation, PSNRs were 60.911 and 59.084, SSIMs 0.445 and 0.279, and MSEs 5.272 and 8.030, demonstrating slightly reduced performance due to geometric changes. Scaling, contrast, and intensity adjustments achieved higher PSNRs (65.576–66.261), SSIMs (0.747–0.927), and very low MSEs (1.538–1.801), reflecting excellent detail retention. Similarly, motion blur, sharpening, and flipping maintained PSNR values 62.208–65.790, SSIM 0.392–0.808, and MSE 1.403–3.911, confirming that BM3D provided robust denoising and structural preservation for CXR images across multiple augmentation types.

The OU-Net with MGWO framework was applied to both CT and CXR datasets to achieve precise medical image segmentation. Initially, images were preprocessed with BM3D to enhance structural details and suppress noise, followed by extraction of multi-scale features using the optimized U-Net architecture. The MGWO algorithm was employed to fine-tune network parameters, improving the selection of relevant features and enhancing convergence during training. Segmentation was performed by combining the hierarchical feature maps with skip connections, allowing the model to accurately delineate both COVID-19 lesions and normal anatomical regions. Finally, the predicted masks were refined to ensure smooth boundaries and spatial consistency, resulting in robust and reliable segmentation across varying imaging conditions.

The proposed OU-Net with MGWO demonstrated exceptional segmentation performance on CT datasets for both COVID-19 and non-COVID-19 images. For COVID-19 cases, it achieved accuracy of 0.990, sensitivity 0.990, and specificity 1.000, indicating near-perfect detection of infected regions while fully distinguishing healthy tissue. Precision and recall were 1.000 and 0.990, respectively, with an F1-score of 0.995, a Jaccard index of 0.995, and a Dice score of 1.000, reflecting almost complete overlap between predicted and ground-truth masks. Similarly, for non-COVID-19 images, the model attained accuracy 0.999, sensitivity 0.999, specificity 1.000, precision and recall of 1.000 and 0.999, F1-score 0.999, Jaccard index 0.999, and Dice score 1.000, demonstrating excellent generalization and robustness in segmenting healthy CT scans. These results indicate that OU-Net with MGWO outperforms existing methods by effectively capturing fine structural details and pathological regions, ensuring highly reliable segmentation for diagnostic purposes.

On the CXR dataset, the proposed OU-Net with MGWO also delivered superior performance for COVID-19 and non-COVID-19 cases. For COVID-19 images, the framework achieved accuracy of 0.9859, sensitivity 0.9902, and specificity 0.9853, showing strong detection of lesions while maintaining precise identification of normal lung regions. The model obtained precision 0.9868, recall 0.9047, F1-score 0.9830, Jaccard index 0.9956, and Dice score 0.9818, reflecting highly accurate and consistent segmentation. Similarly, for non-COVID-19 images, it produced accuracy 0.9859, sensitivity 0.9902, specificity 0.9853, precision 0.9868, recall 0.9047, F1-score 0.9830, Jaccard index 0.9956, and Dice score 0.9818, demonstrating robust performance across normal CXR. Overall, these results confirm that OU-Net with MGWO reliably segments CXR images, accurately preserving anatomical structures and pathological regions, and provides a highly effective tool for automated COVID-19 detection and analysis.

Finally, the methodology was extended to classification using the novel CT-CXR-Net. The BM3D-denoised images were segmented by OU-Net, with parameters optimized through MGWO. ResNet50 was employed for deep feature extraction, capturing complex patterns from both CT and CXR images. Furthermore, IBBO was used to select the most informative features, reducing dimensionality and improving classifier

efficiency. Finally, a Ridge Classifier performed COVID-19 versus Normal classification, balancing bias and variance to achieve robust performance across diverse datasets.

The proposed CT-CXR-Net achieved perfect classification on the CT dataset for both COVID-19 and non-COVID-19 cases. For COVID-19, it reached performance of 1.00, indicating all infected cases were correctly identified without any misclassification. Similarly, for non-COVID-19, the model also attained 1.00 across all metrics, reflecting flawless detection of healthy cases. The confusion matrix confirms this performance with 248 TP and 244 TN, and 0 FP/FN, showing no errors in classification. These results highlight the model's robustness in CT images, effectively capturing pathological features while maintaining complete separation between COVID-19 and normal regions, outperforming standard architectures like InceptionV3, VGG16, VGG19, and ResNet50.

On the CXR dataset, the proposed CT-CXR-Net also demonstrated superior performance compared to existing CNNs. For COVID-19, it achieved accuracy 0.990, precision 0.995, recall 1.000, and F1-score 0.997, while non-COVID-19 cases reached accuracy 0.995, precision 0.998, recall 1.000, and F1-score 0.999. The confusion matrix shows 233 TP and 173 TN, with 1839 FP and 1988 FN, reflecting a strong classification capability despite a higher number of total cases in CXR images. Overall, the proposed methodology effectively differentiates between COVID-19 and normal CXR, outperforming InceptionV3, VGG16, and VGG19 by leveraging optimized feature extraction and robust learning strategies.

6.2 Future Scope

The proposed methodology was extended by integrating multi-modal imaging data, such as combining CT, CXR, and MRI scans, to further enhance COVID-19 detection and severity assessment. Leveraging multi-modal data improve the model's ability to capture complementary information from different imaging modalities, enabling more comprehensive diagnosis and better differentiation of COVID-19 from other pulmonary diseases. Additionally, incorporating temporal imaging data allow for disease progression monitoring and prediction of patient outcomes.

Another avenue for future research is the development of lightweight and real-time models suitable for deployment on edge devices and point-of-care systems. Optimizing OU-Net, CT-CXR-Net, and feature selection algorithms for computational efficiency facilitate faster processing without compromising accuracy, making the framework practical for use in resource-constrained environments such as rural hospitals or mobile diagnostic units. Techniques such as model pruning, quantization, or knowledge distillation was explored to reduce model size and inference time.

Finally, research focus on XAI and uncertainty quantification to improve trust and interpretability in clinical decision-making. Visual explanation methods, such as Grad-CAM or attention maps, help clinicians understand which regions of the images contributed most to the classification or segmentation decision. Moreover, integrating uncertainty estimation provide confidence scores for predictions, enabling safer and more reliable use in real-world clinical scenarios. These enhancements make the system not only more accurate but also more transparent and clinically acceptable.

References

[1]. Caliman Sturdza, Olga Adriana, Florin Filip, Monica Terteliu Baitan, and Mihai Dimian. "Deep Learning Network Selection and Optimized Information Fusion for Enhanced COVID-19 Detection: A Literature Review." Diagnostics 15, no. 14 (2025): 1830.

[2]. Aboshosha, Ashraf. "AI based medical imagery diagnosis for COVID-19 disease examination and remedy." Scientific Reports 15, no. 1 (2025): 1607.

[3]. Kumar, Sunil, and Biswajit Bhowmik. "ADConv-Net: Advanced Deep Convolution Neural Network for COVID-19 Diagnostics Using Chest X-Ray and CT Images." SN Computer Science 6, no. 5 (2025): 1-22.

[4]. Hussain, Md Jabed, and Awakash Mishra. "Transforming Public Health with AI and Big Data Deep Learning for COVID-19 Detection in Medical Imaging." Journal of Intelligent Systems & Internet of Things 16, no. 2 (2025).

[5]. Kibria, Hafsa Binte, Md Ali Hossain, Shazia Rehman, Damminda Alahakoon, and Md Anisur Rahman. "An explainable lightweight parallel depth-wise separable model for lung infection detection from chest X-rays." Neural Computing and Applications 37, no. 6 (2025): 4545-4566.

[6]. Ertam, Fatih, and Ilhan Firat Kilincer. "Predicting and diagnosis of COVID-19 based on IoT and machine learning algorithm." In Advances in Computers, vol. 137, pp. 255-290. Elsevier, 2025.

[7]. Nauman, Muhammad, Sunil Ashraf, Muhammad Usman Javeed, Shafqat Maria Aslam, Usman Farooq, and Ali Raza. "Deep Transfer Learning for COVID-19 Screening: Benchmarking ResNet50, VGG16, and GoogleNet on Chest X-Ray Images." International Journal of Advanced Computing & Emerging Technologies 1, no. 2 (2025): 69-83.

[8]. Dharmik, Anjali. "COVID-19 Pneumonia Diagnosis Using Medical Images: Deep Learning–Based Transfer Learning Approach." JMIRx Med 6 (2025): e75015.

[9]. Fekri-Ershad, Shervan, and Khalegh Behrouz Dehkordi. "A Flexible Multi-Channel Deep Network Leveraging Texture and Spatial Features for Diagnosing New COVID-19 Variants in Lung CT Scans." Tomography 11, no. 9 (2025): 99.

[10]. Mitra, Sanjoy, Parijata Majumdar, Diptendu Bhattacharya, and Srijan Roy. "A Comprehensive Analysis of Artificial Intelligence Methods to Detect COVID-19." In Emerging Trends and Technologies on Intelligent Systems: Proceedings of 4th International Conference ETTIS 2024, vol. 1073, p. 57. Springer Nature, 2025.

[11]. Ilesanmi, Ademola E., Taiwo Ilesanmi, Babatunde Ajayi, Gbenga A. Gbotoso, and Samir Brahim Belhaouari. "Unlocking the Power of 3D Convolutional Neural Networks for COVID-19 Detection: A Comprehensive Review." Journal of Imaging Informatics in Medicine (2025): 1-19.

[12]. Mahdi, A. B., Al-Ibraheemi, Z. A., Atta, Z. H., Mashkoor, H. F., Hussein, H. A., Al-Bayaty, A., & AlZubaidi, A. (2025, February). Advanced Image Enhancement and Deep Learning Models for COVID-19 Features Detection in Chest X-Ray and CT Images. In International Conference On Innovative Computing and Communication (pp. 101-117).

[13]. Anakal, Sudhir, and Chandrashekhar Uppin. "Diagnosis of COVID-19 and Viral Pneumonia with Chest X-Ray Images Using ResNet-34." Iraqi Journal for Computer Science and Mathematics 6, no. 3 (2025): 6.

[14]. Gangwar, Shivam, Reeta Devi, Nor Ashidi Mat Isa, and Soontorn Oraintara. "Enhanced COVID-19 detection from chest X-rays using ERBMAHE and a channel attention-based hybrid CNN model." Soft Computing 29, no. 13 (2025): 5071-5093.

[15]. Biswas, Swarnava, Bipasa Bimalendu Patra, and Anindya Sundar Das. "Chest X-Ray Based AI-Driven Method for Detection of COVID-19 Infected Patients." In 2025 International Conference on Advances in Modern Age Technologies for Health and Engineering Science (AMATHE), pp. 1-5. IEEE, 2025.

[16]. KV, Greeshma, and J. Viji Gripsy. "RadientFusion-XR: A Hybrid LBP–HOG Model for COVID-19 Detection Using Machine Learning." Biotechnology and Applied Biochemistry (2025).

[17]. Herng, O. W., Nasir, A. S. A., & Sukor, A. S. A. (2025). Robust Segmentation of COVID-19 Chest X-Ray Images: Analysis of Variant k-Means Based Clustering Algorithms. Journal of Advanced Research in Applied Sciences and Engineering Technology, 44(1), 77-93.

[18]. Mahmood Khan, R. N., Hussain, L., Alluhaidan, A. S., Majid, A., Lone, K. J., Verdiyev, R., ... & Duong, T. Q. (2025). COVID-19 lung infection detection using deep learning with transfer learning and ResNet101 features extraction and selection. Waves in Random and Complex Media, 35(4), 7886-7909.

[19]. Ghasemi, Safiye, Somayeh Ghasemi, Amir Masoud Rahmani, and Rohollah Barzamini. "Transfer Learning-based Detection of COVID-19 Cases from Chest CT Scans." Power, Control, and Data Processing Systems 2, no. 3 (2025): e727221.

[20]. Clement David-Olawade, Aanuoluwapo, David B. Olawade, Laura Vanderbloemen, Oluwayomi B. Rotifa, Sandra Chinaza Fidelis, Eghosasere Egbon, Akwaowo Owoidighe Akpan, Sola Adeleke, Aruni Ghose, and Stergios Boussios. "AI-Driven Advances in Low-Dose Imaging and Enhancement—A Review." Diagnostics 15, no. 6 (2025): 689.

[21]. AN bin Azhar, Ahmad Nuruddin, and Nor Samsiah Sani. "Enhancing COVID-19 Detection in X-Ray Images Through Deep Learning Models with

Different Image Preprocessing Techniques." International Journal of Advanced Computer Science & Applications 16, no. 1 (2025).

[22]. AM, Arul Raj, Jayant Giri, Naim Ahmad, and Ahmed Said Badawy. "Detection of Covid-19 based on convolutional neural networks using pre-processed chest X-ray images." Aip Advances 14, no. 3 (2024).

[23]. Hassan, Esraa, Mahmoud Y. Shams, Noha A. Hikal, and Samir Elmougy. "Detecting COVID-19 in chest CT images based on several pre-trained models." Multimedia Tools and Applications 83, no. 24 (2024): 65267-65287.

[24]. Mittal, Ajay, Navdeep Kaur, Aastha Gupta, and Gurprem Singh. "Deep residual learning-based denoiser for medical X-ray images." Evolving Systems 15, no. 6 (2024): 2339-2353.

[25]. Anitha, N., T. M. Rajesh, Pritee Parwekar, and Nitheesh Ram Chatradi. "Denoising and Quality Enhancement of CT Scan/X-Ray Images of Lung Disease for Enhanced Diagnosis." In Proceedings of Eighth International Conference on Information System Design and Intelligent Applications, pp. 29-44. Singapore: Springer Nature Singapore, 2024.

[26]. Bhonsle, Devanand. "Suppression of noise signals from computed tomography and ultrasound medical images and performance evaluation." In Artificial Intelligence in Biomedical and Modern Healthcare Informatics, pp. 323-337. Academic Press, 2025.

[27]. Bhonsle, Devanand. "Suppression of noise signals from computed tomography and ultrasound medical images and performance evaluation." In Artificial Intelligence in Biomedical and Modern Healthcare Informatics, pp. 323-337. Academic Press, 2025.

[28]. Reddy, K. Lokeshwar, and G. Bharathi Mohan. "Enhancing Medical Imaging: Noise Reduction and Super Resolution with Transfer Learning." In 2024 2nd International Conference on Intelligent Data Communication Technologies and Internet of Things (IDCIoT), pp. 1430-1435. IEEE, 2024.

[29]. Haennah, JH Jensha, C. Seldev Christopher, and GR Gnana King. "Combined Unet and CNN image classification model for COVID disease detection using CXR/CT imaging." Journal of Intelligent & Fuzzy Systems 48, no. 5 (2025): 627-643.

[30]. Stephen, Valantina, P. Aruna Jeyanthy, D. Lilly Evangelin, L. Padma Suresh, and D. Ferlin Deva Shahila. "Enhancing X-Ray Imaging: CNN and DWT-Based Noise Reduction for Lower Radiation Exposure." In 2025 8th International Conference on Circuit, Power & Computing Technologies (ICCPCT), pp. 172-176. IEEE, 2025.

[31]. Kushwaha, S., Amuthachenthiru, K., Narasimharao, J., Kumar, D., & Gadde, S. S. (2024, March). Development of advanced noise filtering techniques for medical image enhancement. In 2024 5th International Conference on Intelligent Communication Technologies and Virtual Mobile Networks (ICICV) (pp. 906-912). IEEE.

[32]. Rajaraman, Sivaramakrishnan, Zhaohui Liang, Zhiyun Xue, and Sameer Antani. "Noise-induced modality-specific pretext learning for pediatric chest X-ray image classification." Frontiers in Artificial Intelligence 7 (2024): 1419638.

[33]. Chauhan, Swati, Nidhi Malik, and Rekha Vig. "UNet with ResNextify and IB modules for low-dose CT image denoising." International Journal of Information Technology 16, no. 7 (2024): 4677-4692.

[34]. Mori, K., T. Negishi, R. Sekiguchi, and M. Suzaki. "Reduction of radiation exposure in chest radiography using deep learning-based noise reduction processing: A phantom and retrospective clinical study." Radiography 31, no. 3 (2025): 102958.

[35]. Bocquet, Wesley, Roger Bouzerar, Géraldine François, Antoine Leleu, and Cédric Renard. "Detection of Pulmonary Nodules on Ultra-low Dose Chest Computed Tomography With Deep-learning Image Reconstruction Algorithm." Journal of Thoracic Imaging 40, no. 3 (2025): e0806.

[36]. Kobra, Mst Jannatul, Arman Mohammad Nakib, Peter Mweetwa, and Md Owahedur Rahman. "Effectiveness of Fourier, Wiener, Bilateral, and CLAHE Denoising Methods for CT Scan Image Noise Reduction." Scientific Journal of Engineering Research 1, no. 3 (2025): 96-108.

[37]. Agnes Pearly, A., and B. Karthik. "Advanced Lung Image Enhancement Using Dynamic Dual-Histogram Gamma Correction." In International Conference on Advancements in Smart Computing and Information Security, pp. 172-185. Cham: Springer Nature Switzerland, 2024.

[38]. Hrizi, Dorsaf, Khaoula Tbarki, and Sadok Elasmi. "Optimized Lung Nodule Classification Using CLAHE-Enhanced CT Imaging and Swin Transformer-Based Deep Feature Extraction." Journal of Imaging (2025).

[39]. Hein, Dennis. "Deep learning approaches for denoising, artifact correction, and radiology report generation in CT and chest X-ray imaging." PhD diss., Universitetsservice US-AB, Sweden 2025, 2025.

[40]. [40] Ilesanmi, Ademola E., Taiwo Ilesanmi, Babatunde Ajayi, Gbenga A. Gbotoso, and Samir Brahim Belhaouari. "Unlocking the Power of 3D Convolutional Neural Networks for COVID-19 Detection: A Comprehensive Review." Journal of Imaging Informatics in Medicine (2025): 1-19.

[41]. Riyono, Joko, Supriyadi Supriyadi, Christina Eni Pujiastuti, Sofia Debi Puspa, and Aina Latifa Riyana Putri. "Literacy Review Study on the Implementation of Convolutional Neural Network Architecture in Segmentation and Classification of Lung Medical Images." JISA (Jurnal Informatika dan Sains) 8, no. 1 (2025): 1-7.

[42]. Enshaei, Nastaran, Arash Mohammadi, Farnoosh Naderkhani, Nick Daneman, Rawan Abu Mughli, Reut Anconina, Ferco H. Berger et al. "Differentiation of COVID-19 from other types of viral pneumonia and severity scoring on baseline chest radiographs: Comparison of deep learning with multi-reader evaluation." PLoS One 20, no. 7 (2025): e0328061.

[43]. Prabhu, V. S., and K. K. Thyagharajan. "Enhancing COVID-19 detection through multimodal CT and X-ray image fusion with anisotropic diffusion and loss-attentional physics-informed neural networks." Biomedical Signal Processing and Control 110 (2025): 108200.

[44]. Zhu, Miao, and Zhichao Zhang. "An Improved Sine-Cosine Algorithm with Diversity Control Based on Nonlinearity for Medical Image Segmentation." International Journal of High-Speed Electronics and Systems (2025): 2540874.

[45]. Roberto, Guilherme F., Danilo C. Pereira, Alessandro S. Martins, Thaína AA Tosta, Carlos Soares, Alessandra Lumini, Guilherme B. Rozendo, Leandro A. Neves, and Marcelo Z. Nascimento. "Exploring percolation features with polynomial algorithms for classifying Covid-19 in chest X-ray images." Pattern Recognition Letters 189 (2025): 248-255.

[46]. Mustapha, Benzorgat, Yatong Zhou, Benzorgat Nawel, Shan Chunyan, and Xiao Zhitao. "Optimized attention U-Net for enhanced lung and area of infection segmentation in chest X-Rays and CT scans." Journal of Radiation Research and Applied Sciences 18, no. 3 (2025): 101650.

[47]. Bhongale, Madhavi, Mahesh Maindarkar, Ajit Vyas, and Renu Vyas. "Patch-based U-NET model and MSqueezeNet-PyramidNet for efficient segmentation and classification of tuberculosis, pneumonia, and COVID-19." Multimedia Tools and Applications (2025): 1-35.

[48]. Bhardwaj, Prashant, and Amanpreet Kaur. "DLSAC-Net: An automated enhanced segmentation and classification network for lung diseases detection using chest X-Ray images." Multimedia Tools and Applications (2025): 1-26.

[49]. Yadav, Vivek Kumar, and Jyoti Singhai. "Improved Multiclass Lung Disease Classification Using Segmentation and Deep Learning from Chest X-Ray Images." IETE Technical Review (2025): 1-14.

[50]. Bahroun, Sahbi. "Two-Parallel-Step CNN Framework for Detection of COVID-19 Based on Segmented CT-Scan and Chest X-Ray Images." Vietnam Journal of Computer Science (2025): 1-27.

[51]. Orenc, Sedat, Mehmet Sirac Ozerdem, Emrullah Acar, and Musa Yilmaz. "Automatic segmentation of chest X-ray images via deep-improved various U-Net techniques." Digital Health 11 (2025): 20552076251366855.

[52]. Gtifa, Wafa, Ayoub Mhaouch, Nasser Alsharif, Turke Althobaiti, and Anis Sakly. "Nature-Inspired Multi-Level Thresholding Integrated with CNN for Accurate COVID-19 and Lung Disease Classification in Chest X-Ray Images." Diagnostics 15, no. 12 (2025): 1500.

[53]. Vinothini, R., and G. Niranjana. "Advanced image segmentation and severity prediction for COVID-19 using nnU-Net and optimized FRCNN-GJS algorithm." International Journal of Machine Learning and Cybernetics (2025): 1-21.

[54]. Mehta, Vansh, Anshuman Mathur, Mannan Tyagi, and Aryan Singh Rajpoot. "A MultiResUNet-based Deep Learning Architecture for Accurate Lung Segmentation in Chest X-Rays." In 2025 2nd International Conference on Computational Intelligence, Communication Technology and Networking (CICTN), pp. 968-973. IEEE, 2025.

[55]. Herng, Ooi Wei, Aimi Salihah Abdul Nasir, and Abdul Syafiq Abdull Sukor. "Robust Segmentation of COVID-19 Chest X-Ray Images: Analysis of Variant k-Means Based Clustering Algorithms." Journal of Advanced Research in Applied Sciences and Engineering Technology 44, no. 1 (2025): 77-93.

[56]. Kang, Shilu, Dongfang Li, Jiaxin Xu, Aokun Mei, and Hua Huo. "Segmentation-Assisted Fusion-Based Classification for Automated CXR Image Analysis." Sensors 25, no. 15 (2025): 4580.

[57]. Din, Sadia, Muhammad Shoaib, and Erchin Serpedin. "CXR-Seg: A Novel Deep Learning Network for Lung Segmentation from Chest X-ray Images." Bioengineering 12, no. 2 (2025): 167.

[58]. Biju, Roshima, and Warish Patel. "Enhancing Covid-19 Detection through Deep Learning-Based Segmentation of Chest X-ray Images." Procedia Computer Science 258 (2025): 862-875.

[59]. Kumari, Ranjana, Rajesh Kumar Upadhyay, and Javed Wasim. "WHO Based K-Means Segmentation Algorithm and Hybrid VGG19-SVM Model for Identifying COVID-19 Patients in Chest X-Ray." Optical Memory and Neural Networks 34, no. 1 (2025): 95-114.

[60]. Slika, Bouthaina, Fadi Dornaika, and Karim Hammoudi. "Parallel VMamba and Attention-Based Pneumonia Severity Prediction from CXRs: A Robust Model with Segmented Lung Replacement Augmentation." Diagnostics 15, no. 11 (2025): 1301.

[61]. Qi, Yang, Jiaxin Cai, and Rongshang Chen. "AO-TransUNet: A Multi-Attention Optimization Network for COVID-19 and Medical Image Segmentation." Digital Signal Processing (2025): 105264.

[62]. Alaoui Abdalaoui Slimani, Faical, and M'hamed Bentourkia. "Improving deep learning U-Net++ by discrete wavelet and attention gate mechanisms for effective pathological lung segmentation in chest X-ray imaging." Physical and Engineering Sciences in Medicine 48, no. 1 (2025): 59-73.

[63]. Su, Vanessa, Xiaohan Yuan, Mojtaba Safari, and Xiaofeng Yang. "COVSeg-VLM: vision-language model for reliable segmenting COVID-19 infections in chest x-ray images." In Medical Imaging 2025: Computer-Aided Diagnosis, vol. 13407, p. 134072T. SPIE, 2025.

[64]. Mallick, Devanshi, Arshdeep Singh, Eddie Yin-Kwee Ng, and Vinay Arora. "Classifying chest x-rays for COVID-19 through transfer learning: a systematic review." Multimedia Tools and Applications 84, no. 2 (2025): 689-748.

[65]. Yasin, Hajar Maseeh. "Pneumonia and COVID-19 classification and detection based on convolutional neural network: A review." Asian Journal of Research in Computer Science 18, no. 1 (2025): 174-183.

[66]. Lin, Yun-Chi, and Yu-Hua Dean Fang. "Classification of the ICU Admission for COVID-19 Patients with Transfer Learning Models Using Chest X-Ray Images." Diagnostics 15, no. 7 (2025): 845.

[67]. Rajpoot, Reenu, Sweta Jain, Vijay Bhaskar Semwal, and Deepankar Singh. "Quantitative Assessment of XAI Methods for COVID-19 Detection: A Comparative Approach." SN Computer Science 6, no. 2 (2025): 122.

[68]. Hammad, Mohamed, Mohammed ElAffendi, Ahmed A. Abd El-Latif, Abdelhamied A. Ateya, Gauhar Ali, and Pawel Plawiak. "Explainable AI for lung cancer detection via a custom CNN on CT images." Scientific Reports 15, no. 1 (2025): 12707.

[69]. Rao, B. Narendra Kumar, B. Bhaskar Kumar Rao, and Nagendra Panini Challa. "Harnessing deep learning for the early detection of COVID-19 using chest X-rays." Big Data Analytics and Intelligent Applications for Smart and Secure Healthcare Services (2025): 35.

[70]. Paulretnam, Arthi Devarani, Inbamalar Tharcis Mariapushpum, and Swetha Ramamoorthi. "A real time diagnosis of lung infection using X-ray images." In AIP Conference Proceedings, vol. 3159, no. 1. AIP Publishing, 2025.

[71]. Li, Sihan, and Juhua Huang. "Resgdanet: An efficient residual group attention neural network for medical image classification." Applied Sciences 15, no. 5 (2025): 2693.

[72]. Alhafiz, Fatimah, and Abdullah Basuhail. "The Data Heterogeneity Issue Regarding COVID-19 Lung Imaging in Federated Learning: An Experimental Study." Big Data and Cognitive Computing 9, no. 1 (2025): 11.

[73]. Patnaik, Vijaya, Monalisa Mohanty, and Asit Kumar Subudhi. "CLASSIFICATION OF COVID-19 FROM CHEST X-RAY IMAGES

USING ReSqNet." Biomedical Engineering: Applications, Basis and Communications (2025): 2550009.

[74]. Olowolayemo, A., Shams, W. K., Omer, A. Y. I., Mohammed, Y., & Batha, R. S. (2025). Covid-19 mortality risk prediction using small dataset of chest X-Ray images. In Artificial Intelligence and Applications (Vol. 3, No. 1, pp. 94-109).

[75]. Thilagavathi, P., R. Geetha, S. Jothi Shri, and K. Somasundaram. "An effective COVID-19 classification in X-ray images using a new deep learning framework." Journal of X-Ray Science and Technology (2025): 08953996241290893.

[76]. Agarwal, Saurabh, and K. V. Arya. "CXRNet: CNN-attention based CXR image classifier." Expert Systems 42, no. 1 (2025): e13423.

[77]. Jacob, Basil, and Anisha M. Lal. "C19XNet: A Novel Multi-classification Model for COVID-19 Detection in Chest X-rays." In Congress on Intelligent Systems, pp. 347-364. Springer, Singapore, 2025.

[78]. S. Roy, A. Suresh, P. Sahu, A. Roy and T. R. Gupta, "Novel Pooling-Based VGG-Lite for Pneumonia and Covid-19 Detection From Imbalanced Chest X-Ray Datasets," in IEEE Transactions on Emerging Topics in Computational Intelligence, doi: 10.1109/TETCI.2025.3577509.

[79]. Alotaibi, Reem, Abir Alharbi, Abdulaziz Algethami, and Abdulkader Alkenawi. "Automated diagnosis of COVID-19 using chest X-ray image processing by a Convolutional Neural Network." International Journal of Computer Mathematics 102, no. 2 (2025): 224-244.

[80]. Singh, Kuljeet, Anubha Gaur, Sachin Kumar, Sourabh Shastri, and Vibhakar Mansotra. "Deep CP-CXR: A Deep Learning Model for Classification of Covid-19 and Pneumonia Disease Using Chest X-Ray Images." Annals of Data Science (2025): 1-24.

[81]. Fu, Xiaoyang, Rongbin Lin, Wei Du, Adriano Tavares, and Yanchun Liang. "Explainable hybrid transformer for multi-classification of lung disease using chest X-rays." Scientific Reports 15, no. 1 (2025): 6650.

[82]. Amina, Fareesa, and Krishnanaik Vankdoth. "CODE NET: COVID-19 segmentation and detection via deep learning-based networks." Bulletin of Electrical Engineering and Informatics 14, no. 5 (2025): 3863-3872.

[83]. Pal, Madhumita, Ranjan K. Mohapatra, Ashish K. Sarangi, Alok Ranjan Sahu, Snehasish Mishra, Alok Patel, Sushil Kumar Bhoi et al. "A comparative analysis of the binary and multiclass classified chest X-ray images of pneumonia and COVID-19 with ML and DL models." Open Medicine 20, no. 1 (2025): 20241110.

[84]. Wang, Xicheng, Shuai Zhang, Dejian Wei, Junzhong Zhang, and · Hui Cao. "TMscNet: a model with multiple information interaction for COVID-19 X-ray classification." International Journal of Machine Learning and Cybernetics (2025): 1-18.

[85]. Ameta, Gaurav Kumar, Ganesh Khekare, Ajay Kumar Phulre, S. Jayachitra, Vijendra Pratap Singh, and Vinodh P. Vijayan. "Automated X-Ray Image Classification for COVID-19 Detection Using DenseNet-121 and SVM." In 2025 International Conference on Automation and Computation (AUTOCOM), pp. 307-312. IEEE, 2025.

[86]. Islam, Md Jahidul. "Genetic Optimization-Based Layers Tuning and Freezing in Deep CNN for Low-Cost Disease Detection Using Chest X-Rays." SN Computer Science 6, no. 5 (2025): 1-19.

[87]. Kumar, Sunil, and Harish Kumar. "Efficient-VGG16: A Novel Ensemble Method for the Classification of COVID-19 X-ray Images in Contrast to Machine and Transfer Learning." Procedia Computer Science 235 (2024): 1289-1299.

[88]. M. R and K. S. Pranay, "Automated COVID 19 Detection using InceptionV3 Algorithm to Enhance the Accuracy and Comparing with Shufflenet

Algorithm," 2025 6th International Conference on Mobile Computing and Sustainable Informatics (ICMCSI), Goathgaun, Nepal, 2025, pp. 1472-1478, doi: 10.1109/ICMCSI64620.2025.10883638.

[89]. Balasamy, K., and V. Seethalakshmi. "HCO-RLF: Hybrid classification optimization using recurrent learning and fuzzy for COVID-19 detection on CT images." Biomedical Signal Processing and Control 100 (2025): 106951.

[90]. Kordnoori, Shirin, Maliheh Sabeti, Hamidreza Mostafaei, and Saeed Seyed Agha Banihashemi. "A Deep Learning Framework for Accurate COVID-19 Classification in CT-Scan Images." Machine Learning with Applications (2025): 100628.

[91]. Sahu, Hemlata P., and Ramgopal Kashyap. "FINE_DENSEIGANET: Automatic medical image classification in chest CT scan using Hybrid Deep Learning Framework." International Journal of Image and Graphics 25, no. 01 (2025): 2550004.

[92]. Alharbi, Meshal, and Sultan Ahmad. "Enhancing COVID-19 detection using CT-scan image analysis and disease classification: the DI-QL approach." Health and Technology (2025): 1-12.

[93]. Fathy, Abdelghany, and Hatem Abdel-Kader. "COVID-19 Detection Based on CT scan Using Meta-Heuristic Feature Selection Method." IJCI. International Journal of Computers and Information 12, no. 1 (2025): 24-42.

[94]. Pham, N.T., Ko, J., Shah, M., Rakkiyappan, R., Woo, H.G. and Manavalan, B., 2025. Leveraging deep transfer learning and explainable AI for accurate COVID-19 diagnosis: Insights from a multi-national chest CT scan study. Computers in Biology and Medicine, 185, p.109461.

[95]. Antunes, Carlos, João Rodrigues, and António Cunha. "CTCOVID19: automatic COVID-19 model for computed tomography scans using deep learning." Intelligence-Based Medicine 11 (2025): 100190.

[96]. Kordnoori, Shirin, Maliheh Sabeti, Hamidreza Mostafaei, and Saeed Seyed Agha Banihashemi. "LungXpertAI: A deep multi-task learning model for

chest CT scan analysis and COVID-19 detection." Biomedical Signal Processing and Control 99 (2025): 106866.

[97]. Rezvani, Sadjad, Mansoor Fateh, Yeganeh Jalali, and Amirreza Fateh. "FusionLungNet: Multi-scale fusion convolution with refinement network for lung CT image segmentation." Biomedical Signal Processing and Control 107 (2025): 107858.

[98]. Padmavathi, V., and Kavitha Ganesan. "Metaheuristic optimizers integrated with vision transformer model for severity detection and classification via multimodal COVID-19 images." Scientific Reports 15, no. 1 (2025): 13941.

[99]. Suseela, Suba, and Nita Parekh. "From pixels to prognosis: Attention-CNN model for COVID-19 diagnosis using chest CT images." IET Image Processing 19, no. 1 (2025): e13249.

[100]. Appati, Justice Kwame, Bless Ziamah, Herbert Ansah Akrofi, and Albert Ankomah Dodoo. "SARS detection in chest CT scan images using the bootstrapped ViT-B/16 model." Iran Journal of Computer Science (2025): 1-15.

[101]. Chowa, Sadia Sultana, Md Rahad Islam Bhuiyan, Mst Sazia Tahosin, Asif Karim, Sidratul Montaha, Md Mehedi Hassan, Mohd Asif Shah, and Sami Azam. "An automated privacy-preserving self-supervised classification of COVID-19 from lung CT scan images minimizing the requirements of large data annotation." Scientific Reports 15, no. 1 (2025): 226.

[102]. Tan, Nurlaila, and Idam Arif. "Multiclass Classification of Covid-19 CT Scan Images With VGG-16 Architecture Using Transfer Learning System." Indonesian Journal of Physics 35, no. 1 (2024): 21-26.

[103]. Singh, Retinderdeep, Neha Sharma, Kapil Rajput, and Mukesh Kumar. "High-Accuracy Detection of Cancer, COVID-19, and Tuberculosis in Chest CT Scans Using Fine-Tuned InceptionV3." In 2024 IEEE 3rd World Conference on Applied Intelligence and Computing (AIC), pp. 987-993. IEEE, 2024.

[104]. Gungor, M. A. (2021). A comparative study on wavelet denoising for high noisy CT images of COVID-19 disease. Optik, 235, 166652.

[105]. Newson, K. S., Benoit, D. M., & Beavis, A. W. (2024). Encoder-decoder convolutional neural network for simple CT segmentation of COVID-19 infected lungs. PeerJ Computer Science, 10, e2178.

[106]. Prinzi, Francesco, Carmelo Militello, Vincenzo Conti, and Salvatore Vitabile. 2023. "Impact of Wavelet Kernels on Predictive Capability of Radiomic Features: A Case Study on COVID-19 Chest X-ray Images" Journal of Imaging 9, no. 2: 32. https://doi.org/10.3390/jimaging9020032

[107]. Syafira, Putri Amanda, Novanto Yudistira, and Diva Kurnianingtyas. "Chest X-ray images clustering using convolutional autoencoder for lung disease detection." JOIV: International Journal on Informatics Visualization 9, no. 2 (2025): 838-844.

An Efficient Methodology for Preprocessing of COVID-19 Images Using BM3D Technique

Anitha Patibandla, Kirti Rawal, and Gaurav Sethi

Abstract SARS-CoV-2 virus is an infectious virus that instigated a coronavirus illness (COVID) outbreak in 2019. In the current context, datasets pertaining to study the features of the post COVID-19 symptoms require Computerized tomography (CT) scan, chest X-ray, and statistical data such as oxygen levels and pulse rate. The work focusses on identifying the dataset and cleanse the data and arrange the scattered data to a form amenable to the machine learning module. The dispensation of the images necessitates an image processing technique superseded by engaging appropriate machine learning algorithms contingent on the anticipated distinctive feature. In the same way, for the mathematical dataset, a statistical built algorithm is favored so that computational stretch can be abridged and high data estimation precision can be accomplished. DWT technique was used for noise removal of images. The work has proposed a BM3D technique for effective preprocessing of images. Performance metrics such as PSNR, SSIM, CC, MSE, RMSE, and NCC have been calculated for DWT and BM3D techniques for Covid and non-Covid classes of images and analyzed. The BM3D technique promises better performance for all the metrics.

Keywords Preprocessing · DWT · BM3D · CT images · COVID-19

A. Patibandla (✉)
LPU, Phagwara, Punjab, India
e-mail: anithakamal.ghanta@gmail.com

K. Rawal · G. Sethi
SEEE, LPU, Phagwara, Punjab, India
e-mail: kirti.20248@lpu.co.in

G. Sethi
e-mail: gaurav.11106@lpu.co.in

H. Zen et al. (eds.), *Soft Computing and Signal Processing*, Lecture Notes in Networks and Systems 840, https://doi.org/10.1007/978-981-99-8451-0_52

International Journal of Medical Toxicology & Legal Medicine Volume 27, No. 2, 2024
e-ISSN: 0974-4614
p-ISSN: 0972-0448

Block Matching and 3D Filtering (BM3D) for Preprocessing of CT scans of Covid-19 Lung Images

Anitha Patibandla[1*], Kirti Rawal[2], Gaurav Sethi[3]

[1]Dept.of ECE, Lovely Professional University, Punjab, India, Email: anithakamal.ghanta@gmail.com
[2]Signal and Image Processing Domain, Lovely Professional University, Punjab, India,
Email: kirti.20248@lpu.co.in
[3]Signal and Image Processing Domain, Lovely Professional University, Punjab, India,
Email: gaurav.11106@lpu.co.in
*Corresponding Author

Received: 13.08.2024 Revised: 18.09.2024 Accepted: 24.10.2024

ABSTRACT
SARS-CoV2 or the Corona Virus 2 is the cause of the global Corona Virus illness 2019 epidemic, also known as the COVID-19 pandemic (SARS-CoV-2). Wavelets are mostly used for denoising a two-dimensional signal for images mostly and so we have adopted a Discrete Wavelet Transform for CT image of covid and healthy lung images. Block Matching and 3D filtering can give better performance for pre-processing. Evaluation parameters such as SSIM, CC and NCC are considered for DWT and BM3D methods for Covid and Non-Covid models of imageries and evaluated. The image denoising using DWT resulted in an SSIM value of 0.564 for covid images and 0.6935 for healthy lung images, NCC of 0.997 and 0.998 for covid and healthy lung images respectively and CC of 0.9794 and 0.99234 for covid and non-covid images respectively. Image denoising using BM3D the SSIM values are computed as 0.919 and 0.926 for covid and healthy lung images respectively, NCC of 0.9996 and 0.999689 for covid and healthy lung images respectively and CC of 0.99286 and 0.9967 for covid and healthy lung images respectively. It has been observed that the BM3D method provides a good performance compared to the DWT Technique for both covid and healthy lung images considering the performance metrics.

Keywords: Discrete Wavelet Transform (DWT), BM3D, CT scan Images, Covid-19, SSIM, NCC, CC, Image denoising.

1. INTRODUCTION

Corona Virus is an extremely transmissible disease and was first noticed in Wuhan, China in 2019.The virus has spread rapidly in a very short span of time and became a global pandemic[1].But recently the interest has inclined towards the prediction of the enduring effect of covid-19 effects in the individuals affected by COVID-19[2]. It is identified that, an individual after the covid-19 through current diagnosis system found negative is to be considered to be in the safe zone [3]. However, more intense studies performed globally on a limited number of patients show that the post COVID symptoms in various individuals have evidenced the presence of covid-19 and its impact of effecting individuals in a dreadful way [4]

2. LITERATURE SURVEY

There is a substantial amount of literature cited by the researchers in the research communal on the finding of covid-19 depending on the symptoms and its community infection rate [5]. Few interesting works such as detection of covid-19 from basic questions without in-vivo and in-vitro investigations [6]. The dataset features used by the learning model in the study emphasized on basic information such as gender and age (>60) followed by symptoms such as true/false statements on headache, sore throat, cough, fever and uneasiness in breathing followed by individual contact who is infected with covid-19 [7]. Another interesting work from [8], who classified the symptoms as most common, moderate and severe [9]. The most common symptoms are tiredness, cough and fever whereas moderate symptoms include diarrhoea, conjunctivitis, sore throat, loss of smell and taste and discoloration followed by severe symptoms such as uneasiness in breathing, chest pain and loss of movement [10]. The authors have used various algorithms such as support vector machine (SVM), Random Forest classifier (RFC), k-nearest neighbour (kNN), decision tree classifier and logistic regression. However, XGB classifiers predict the highest accuracy comparative to other available classifiers [11].
Most of the early publications on the machine learning practices for the estimate of COVID-19 are grounded on simple questionnaires, and an interesting question inline to this can be inferred from [12]. The type of the data

A Review on the Detection of the Novel Coronavirus Using Machine Learning Techniques

Anitha Patibandla, Kirti Rawal, and Gaurav Sethi

Abstract The novel Coronavirus which has emerged in late 2019 has impacted the lives of the people around the world and has raised new questions in the healthcare sector. There has been extensive research in the area of COVID-19 detection considering its effect on people's lives everywhere on the planet. The disease has indicated an intensive need for study in the area of Biomedical image processing by the utilisation of Artificial Intelligence and Machine learning strategies. The utmost affected parts in the human body are the lungs. Although RTPCR test can specify whether an individual has Covid or not, it is not a reliable technique since it has low sensitivity and depends on the operator. CT scan of the lungs reveal the exact information about the intensity of the disease in most of the cases and has proved to be reliable. Large datasets are available for carrying out research by using CT scan Imagery. This paper presents an overview of the various methodologies used by various authors in the detection of COVID-19. Application of different Machine learning techniques for the dataset of CT images is proposed and performance metrics will be evaluated in the proposed work.

Keywords Novel corona virus · Biomedical image processing · Artificial intelligence · Machine learning techniques · CT scan

A. Patibandla (✉)
Department of ECE, Lovely Professional University, Punjab, India
e-mail: anithakamal.ghanta@gmail.com

K. Rawal · G. Sethi
Signal and Image Processing Domain, Lovely Professional University, Punjab, India
e-mail: kirti.20248@lpu.co.in

G. Sethi
e-mail: gaurav.11106@lpu.co.in

V. Bhateja et al. (eds.), *Information System Design: AI and ML Applications*, Lecture Notes in Networks and Systems 1107, https://doi.org/10.1007/978-981-97-6581-2_37

SSRG International Journal of Electronics and Communication Engineering
ISSN: 2348-8549/ https://doi.org/10.14445/23488549/IJECE-V12I8P128

Volume 12 Issue 8, 316-333, August 2025

Original Article

CT-CXR-Net: Optimal Deep Learning Framework for Dual-Modal COVID-19 Classification

Anitha Patibandla[1], Kirti Rawal[2]

[1,2]*Department of SEEE, Lovely Professional University, Punjab, India.*

[1]*Corresponding Author : anithakamal.ghanta@gmail.com*

Received: 15 June 2025 Revised: 16 July 2025 Accepted: 17 August 2025 Published: 30 August 2025

Abstract *- Since the onset of the COVID-19 pandemic, more than 700 million people have been impacted by the disease, and more than 7 million people have died, underlining the necessity of quickly and efficiently identifying and diagnosing the disease in controlling its spread. Despite the immense progress, conventional methods of testing usually experience the drawback of being too slow, accessible, and imprecise, especially within resource-limited settings. Existing COVID-19 classification models based on Artificial Intelligence (AI) are affected by noise interference of the medical images, sub-optimal segmentation, and inefficient feature selection, all of which contribute to a low reliability of diagnosis. To overcome these challenges, the novel CT-CXR-COVID-19 Classification Network (CT-CXR-Net) method begins with Block-Matching and 3D filtering (BM3D) denoising to effectively eliminate complex noise patterns, ensuring high-quality input for further analysis. An Optimal U-Net (OU-Net) segmentation model is employed, whose loss is minimized using Modified Grey Wolf Optimization (MGWO), leading to precise lung region extraction. Subsequently, ResNet50 is utilized for deep feature extraction, capturing complex and informative patterns from both Computer Tomography (CT) and Chest X Ray (CXR) images. To reduce feature dimensionality and enhance classification performance, Improved Brown Bear Optimization (IBBO) is adopted for optimal feature selection. Finally, a Ridge Classifier provides robust and efficient classification, maintaining a balance between bias and variance. This approach achieves exceptional results on separate datasets, with the CT dataset recording 100% accuracy, while the CXR dataset achieves 99.30% accuracy, 99.60% precision, and 99.95% recall and F1-score, demonstrating its potential for reliable and high-performance COVID-19 diagnosis.*

Keywords *- BM3D denoising, COVID-19 detection, medical image classification, Modified Grey Wolf Optimization, U-Net segmentation.*

1. Introduction

Since late 2019, COVID-19 has surpassed 700 million confirmed cases and produced over 7 million deaths globally, marking one of the most devastating pandemics in modern history [1]. Its rapid transmission, driven by asymptomatic spread and variants of concern, has placed unparalleled pressure on healthcare systems, revealing a critical need for fast, accurate, and scalable diagnostic tools to manage disease progression and prevent further casualties.

Conventional diagnostic approaches [2], such as radiologist-interpreted imaging, have faced significant challenges. RT-PCR testing delays and variable Sensitivity hinder timely detection, particularly in asymptomatic and early-stage cases [3]. Meanwhile, radiological analysis of chest CT and CXR scans depends heavily on clinician expertise, leading to inconsistent results, high workloads, and limited access, especially in under-resourced settings. To address these limitations, several companies have developed AI-integrated medical imaging solutions. Infervision's AI-powered CT tool [4], deployed in over 34 Chinese hospitals, flagged signs of COVID-19 pneumonia within seconds from thousands of scans. US-grown Aidoc's AI triage system, FDA-approved for chest CT scans, is now in use in more than 1,500 imaging centers globally, including Yale New Haven and Cedars-Sinai. Additionally, Alibaba's cloud-based CT analysis system [5] reached diagnosis speeds of around 20 seconds with 96 % accuracy across 26 hospitals. These examples demonstrate industry-scale strides in integrating AI for rapid and accurate imaging support. Hospitals worldwide have begun adopting AI-augmented imaging tools to assist clinical workflows. Zhongnan Hospital of Wuhan University deployed Infervision's CT software to triage and isolate suspected cases early in the outbreak [6]. In South Korea and Brazil, Lunit's CXR AI solution [7] supported radiologists in high-volume COVID-19 screening. Meanwhile, Minnesota hospitals conducted prospective validation of interpretable CXR AI tools across 12 institutions, demonstrating specificity and sensitivity improvements during real-time clinical use. Academic institutions and multinational hospital networks

A Review on the Detection of the Post COVID-19 Symptoms for Long Term Diseased Patients using Machine Learning Algorithms

Anitha Patibandla
Research Scholar, Dept.of ECE, Lovely Professional University, Punjab, India
anithakamal.ghanta@gmail.com, (0000-0002-1657-6966)

Abstract. Long term diseases require continuous monitoring, sometimes periodic monitoringto verify if any serious concern requires an attention. In recent years, it is noticed that the COVID-19 pandemic has triggered serious concern towards the long-term diseased individuals. As the mortality rate of the COVID-19 clearly indicates that the highest percentage of deaths reflect in the individuals suffering from long term diseases such as diabetes, pneumonia, cardiovascular and acute renal failure. Though they are tested for COVID negative through conventional apparatus, it doesn't confer that they are completely out of post consequences. Hence a periodic, if necessary continuous monitoring needs to be aided, which in current scenario is a challenging task. Hence, our current article reviews the use of machine learning algorithms to detect and diagnose pre and post COVID-19 effects onlong term diseased patients.

1. Introduction

Machine learning algorithms received significant attention in the scientific community due to their intriguing nature of predicting the physical phenomena through historical data. The learning basically adopts in two phases, supervised [33] and unsupervised learning [39]. Supervised learning requires regression and classifiers to process the data, whereas unsupervised learning requires clustering of data to predict the phenomena. In the current context, we would like to emphasize on the COVID-19prediction and diagnosis through these machine learning algorithms. However, there is an ample amount of research cited in the literature to realize the feasibility of using the machine learning algorithms. Currently, supervised learning algorithms are in application, but most of them are still in laboratories and haven't received clinical compliance yet. The complexity of the clinical compliance is due to the mutation of variants displaying different symptoms and hence, it is still observed to be a lacuna for now [3].Since machine learning algorithms have feasibility of processing large amount of data that makes the prediction model more accurate, we stick our current interest towards prediction and diagnosis of post COVID-19 effects on the long-term diseased patients. Long term diseases patients suffering from diabetes mellitus [35], cardiovascular [37], pneumonia and acute renal failure [31] display a complex behavior over a period of time which is difficult to predict that root cause is due to COVID-19. Hence a continuous monitoring of the patient and data isrequired. Works pertaining to detection of pre COVID- 19 symptoms have been well cited in the literature using demographic [4], standard symptoms [2] and physical characteristics [8] of the individuals. The post symptoms of covid-19 on a healthy individual is not reported elsewhere and for a diseased individual, it is very scarcely cited and recent inclination in this area enabled us to write the current review. The article emphasizes on the various long-term diseases and their symptoms, COVID-19 effect on these diseases, datasets available and machine learning algorithms.

2. Review on long term diseases

Long term diseases are those which may not be infectious but slowly decline the inherent body characteristics over time resulting in death. These individuals have very low immune system, though not clinically evidenced but over a long time, they are prone to get effected easily by infectious diseases such as COVID-19 in the current case. Majority of the long-term diseased patients have foreseen diabetes mellitus which is most commonly seen disease in the current era, followed by pneumonia, acute renal kidney failure and typical cardiovascular diseases. We shall now discourse each of them individually so that the nature of the disease allows us to classify the features to be used for a machine learning model.

Journal of Innovative Image Processing (ISSN: 2582-4252)
www.irojournals.com/iroiip/

Adaptive Lung Segmentation Using Optimal U-Net and Grey Wolf Optimization for COVID-19 Chest X-Rays

Anitha Patibandla[1], Manu Prakram[2]

Department of Electronics and Electrical Engineering, Lovely Professional University, Punjab, India.

E-mail: [1]anithakamal.ghanta@gmail.com, [2]manu.14704@lpu.co.in

Abstract

The chest X-ray imaging (CXR) is a key diagnostic instrument in COVID-19 diagnosis, wherein more than 600,000 tests are performed worldwide annually and the misdiagnosis rate is estimated to be 15-20 percent, largely contributed by human error. Conventional manual reading of CXR images is time-consuming, labor-intensive, and heavily reliant on the skill of the radiologist, typically resulting in a series of uneven and sluggish diagnostic outcomes. To overcome these limitations, the current research introduces an innovative state-of-the-art CXR segmentation model based on rigorous preprocessing techniques in combination with the optimisation of deep-learning algorithms to obtain precise lung parenchyma and pathological lesion outlines. Block-matching 3D filtering (BM3D) was applied to suppress noise without loss of anatomical details following curation of the COVID-19 CXR Dataset. The Optimization U-Net (OU-Net) architecture, which served as the backbone of the proposed approach, was carefully designed with adaptive encoder-decoder paths and strengthened skip connections to better subdivide real lung regions and manifestations of diseases. Additionally, the training schedule utilizes Modified Grey Wolf Optimization (MGWO) for the optimization of network parameters, and this accelerates convergence and enhances segmentation accuracy. Empirical results confirm that the OU-Net with MGWO is superior to conventional and standard deep-learning models, as the suggested approach enhances accuracy by 4.58%, sensitivity by 5.22%, specificity by 4.60%, precision by 4.85%, recall by 1.78%, F1-score by 5.07%, Jaccard index by 5.23%, and Dice score by 5.31%.

Keywords: Block-matching and 3D Filtering, COVID-19, Chest X-Ray, Grey Wolf Optimization, Optimal U-Net, Segmentation.

1. Introduction

Over 777 million confirmed COVID-19 cases and 7.1 million deaths were reported globally by mid-May 2025, translating to a global fatality rate of about 0.91% of confirmed infections [1]. Although many studies indicate much higher excess mortality, perhaps more than twice the reported amount, these figures represent the official counts [2]. Although some resurgence has been observed in parts of Asia and the Middle East, test positivity rates and reported new cases have decreased in recent months in many regions [3]. It is essential to accurately segment the lung regions in CXRs to identify abnormalities related to COVID-19, such as consolidations and ground-glass opacities [4]. Segmentation enables Artificial

DOI: https://doi.org/10.36548/jiip.
Received: DD.MM.YYYY, received in revised form: DD.MM.YYYY, accepted: DD.MM.YYYY, published: DD.MM.YYYY